



**Single Particle Tracking
Membrane Receptor Dynamics**

**Einzelpartikelverfolgung
Dynamik der Membranrezeptoren**

Doctoral thesis for a doctoral degree
at the Graduate School of Life Sciences,
Julius-Maximilians-Universität Würzburg,
Section Biomedicine

submitted by

Monika Zelman-Femiak

from

Warsaw, Poland

Würzburg 2011

Submitted on:

Members of the Promotionskomitee:

Chairperson:

Prof. Dr. Martin Müller

Primary Supervisor:

Dr. Gregory Harms

Supervisor (Second):

Prof. Dr. Petra Knaus

Supervisor (Third):

PD Dr. Heike Hermanns

Supervisor (Fourth):

Prof. Dr. Caroline Kisker

Date of Public Defence:

Date of receipt of Certificates:

Affidavit

I hereby confirm that my thesis entitled “Single Particle Tracking - Membrane Receptor Dynamics” is the result of my own work. I did not receive any help or support from commercial consultants. All sources and / or materials applied are listed and specified in the thesis.

Furthermore, I confirm that this thesis has not yet been submitted as part of another examination process neither in identical nor in similar form.

Würzburg, 04.07.2011.

Eidesstattliche Erklärung

Hiermit erkläre ich an Eides statt, die Dissertation “Einzelpartikelverfolgung - Dynamik der Membranrezeptoren“ eigenständig, d.h. insbesondere selbständig und ohne Hilfe eines kommerziellen Promotionsberaters angefertigt und keine anderen als die von mir angegebenen Quellen und Hilfsmittel verwendet zu haben.

Ich erkläre außerdem, dass die Dissertation weder in gleicher noch in ähnlicher Form bereits in einem anderen Prüfungsverfahren vorgelegen hat.

Würzburg, 04.07.2011.

Acknowledgements

I would like to thank **Dr. Gregory Harms** from the Bio-Imaging Center, Rudolf Virchow Center, University of Würzburg, Würzburg, Germany for the possibility of conducting this work, general supervision and valuable discussions.

I want to express my gratitude to **Prof. Dr. Petra Knaus** from the Institute for Chemistry and Biochemistry, Free University of Berlin, Berlin, Germany for fruitful cooperation on the BMP project, advices concerning theoretical and practical aspects of the work and care.

I am thankful to all my **colleagues** from both groups in Würzburg and Berlin for effective teamwork, friendly atmosphere and support.

I want to thank the **Promotionskomitee** for superintendence of my PhD studies at the Graduate School of Life Sciences, constructive comments and substantial help.

“Clear your mind of can’t”

Samuel Johnson

*I dedicate this work
to my Closest
who have supported me ceaselessly
and kept me believing that I can.*

Contents

Summary 6

Zusammenfassung 9

Chapter 1 12

ACP - acyl carrier protein as a covalent linkage between receptor and quantum dot for single-molecule studies

1.1. Introduction 13

1.2. Results & Discussion 15

1.3. Materials and methods 23

1.4. References 28

Chapter 2 32

BMP type I and II receptors mobility linked to non-SMAD/SMAD signaling

2.1. Introduction 33

2.2. Results & Discussion 35

2.3. Materials and methods 52

2.4. References 62

Chapter 3 65

Quantum dots for single-molecule biological imaging on native cell membranes

3.1. Introduction 66

3.2. Results & Discussion 68

3.3. Materials and methods 85

3.4. References 88

Chapter 4 92

PTHr – parathyroid hormone receptor mobility, internalization and recycling in single-molecule studies

4.1. Introduction 93

4.2. Results & Discussion 95

4.3. Materials and methods 100

4.4. References 103

Curriculum Vitae 106

Publications 107

Summary

Single-molecule microscopy is one of the decisive methodologies that allows one to clarify cellular signaling in both spatial and temporal dimensions by tracking with nanometer precision the diffusion of individual microscopic particles coupled to relevant biological molecules. Trajectory analysis not only enables determination of the mechanisms that drive and constrain the particles motion but also to reveal crucial information about the molecule interaction, mobility, stoichiometry, all existing subpopulations and unique functions of particular molecules. Efficacy of this technique depends on two problematic issues the usage of the proper fluorophore and the type of biochemical attachment of the fluorophore to a biomolecule.

The goal of this study was to evolve a highly specific labeling method suitable for single molecule tracking, internalization and trafficking studies that would attain a calculable 1:1 fluorophore-to-receptor stoichiometry. A covalent attachment of quantum dots to transmembrane receptors was successfully achieved with a technique that amalgamates acyl carrier protein (ACP) system as a comparatively small linker and coenzyme A (CoA)-functionalized quantum dots.

The necessity of optimization of the quantum dot usage for more precise calculation of the membrane protein stoichiometries in larger assemblies led to the further study in which methods maximizing the number of signals and the tracking times of diverse QD types were examined. Next, the optimized techniques were applied to analyze behavior of interleukin-5 β -common chain receptor (IL-5R β c) receptors that are endogenously expressed at low level on living differentiated eosinophil-like HL-60 cells.

Obtained data disclosed that perused receptors form stable and higher order oligomers. Additionally, the mobility analysis based on increased in number (>10%) uninterrupted 1000-step trajectories revealed two patterns of confined motion.

Thereupon methods were developed that allow both, determination of stoichiometries of cell surface protein complexes and the acquisition of long trajectories for mobility analysis.

Sequentially, the aforementioned methods were used to scrutinize on the mobility, internalization and recycling dynamics characterization of a G protein-coupled receptor (GPCRs), the parathyroid hormone receptor (PTH1R) and several bone

morphogenetic proteins (BMPs), a member of the TGF-beta superfamily of receptors. These receptors are two important representatives of two varied membrane receptor classes.

BMPs activate SMAD- and non-SMAD pathways and as members of the transforming growth factor β (TGF- β) superfamily are entailed in the regulation of proliferation, differentiation, chemotaxis, and apoptosis. For effective ligand induced and ligand independent signaling, two types of transmembrane serine/threonine kinases, BMP type I and type II receptors (BMPRI and BMPRII, respectively) are engaged. Apparently, the lateral mobility profiles of BMPRI and BMPRII receptors differ markedly, which determinate specificity of the signal. Non-SMAD signaling and subsequent osteoblastic differentiation of precursor cells particularly necessitate the confinement of the BMP type I receptor, resulting in the conclusion that receptor lateral mobility is a dominative mechanism to modulate SMAD versus non-SMAD signaling during differentiation.

Confined motion was also predominantly observed in the studies devoted to, entailed in the regulation of calcium homeostasis and in bone remodeling, the parathyroid hormone receptor (PTH1R), in which stimulation with five peptide ligands, specific fragments of PTH: hPTH(1–34), hPTHrP(107–111)NH₂; PTH(1–14); PTH(1–28) G^{1R19}, bPTH(3–34), first four belonging to PTH agonist group and the last to the antagonist one, were tested in the wide concentration range on living COS-1 and AD293 cells.

Next to the mobility, defining the internalization and recycling rates of the PTH1R receptor maintained in this investigation one of the crucial questions. Internalization, in general, allows to diminish the magnitude of the receptor-mediated G protein signals (desensitization), receptor resensitization via recycling, degradation (down-regulation), and coupling to other signaling pathways (e.g. MAP kinases). Determinants of the internalization process are one of the most addressed in recent studies as key factors for clearer understanding of the process and linking it with biological responses evoked by the signal transduction.

The internalization of the PTH-receptor complex occurs via the clathrin-coated pit pathway involving β -arrestin2 and is initiated through the agonist occupancy of the PTH1R leading to activation of adenylyl cyclase (via G_s), and phosphatidylinositol-specific phospholipase C _{β} (via G_q).

Taken together, this work embodies complex study of the interleukin-5 β -common chain receptor (IL-5R β c) receptors, bone morphogenetic proteins (BMPs) and the parathyroid hormone receptor with the application of single-molecule microscopy with the newly attained ACP-quantum dot labeling method and standard techniques.

Zusammenfassung

Die Einzelmolekül-Mikroskopie, das Verfolgen der Diffusion einzelner, mikroskopischer Partikel, welche an relevanten biologischen Molekülen gekoppelt sind, ist eine der entscheidenden Verfahren zur räumlichen und zeitlichen Quantifizierung der Zellsignalisierung und hat eine Genauigkeit im Nanometerbereich. Die so gewonnene Trajektorienanalyse ermöglicht nicht nur die Bestimmung der Mechanismen, die der Bewegung der Partikel zugrunde liegen, sondern liefert auch wichtige Informationen über die molekulare Wechselwirkungen, Bewegungsfreiheit und Stöchiometrie sowie über alle existierenden Subpopulationen und besondere Funktionen der einzelnen Moleküle. Die Wirksamkeit dieser Technik hängt von der Verwendung des geeigneten Fluorophors und der Art seiner biochemischen Anhaftung ab.

Das Ziel dieser Arbeit war die Entwicklung eines hochspezifischen Markierungsverfahrens, das zur Verwendung der Einzelmolekül-Mikroskopie für Studien im Bereich Endozytose geeignet ist und gleichzeitig eine Fluorophore-Rezeptor Stöchiometrie von 1:1 erreicht. Eine kovalente Anhaftung von Quantenpunkten an Membranrezeptoren wurde erfolgreich in einer Methode realisiert, die ACP-Systeme (Engl. Acyl-Carrier-Protein) mit Koenzym A (CoA-) funktionalisierten Quantenpunkten amalgamiert.

Die notwendige Optimierung der Verwendung von Quantenpunkten mit dem Ziel einer genaueren Berechnung der Stöchiometrie von Membranproteinen sehr großer Anzahl führte zu weiteren Studien. In diesem Zusammenhang wurden Methoden zur Maximierung der Signalanzahl und Beobachtungszeiten diverser Quantenpunktentypen untersucht. Im nächsten Schritt wurden die optimierten Verfahren angewendet, um das Verhalten von IL-5R β c (Engl. Interleukin-5 β -common chain receptor) Rezeptoren, die endogen auf niedriger Stufe auf lebende differenzierte eosinophile-ähnlichen HL-60 Zellen existieren, zu analysieren.

Die gewonnenen Daten haben gezeigt, dass die Rezeptoren sich in stabilen Oligomeren hoher Ordnung bilden, was zusätzlich mit den Ergebnissen der Analyse der Mobilität, die auf einer hohen Anzahl unterbrochener 1000-Schritt Trajektorien basiert, zwei abgegrenzte Bewegungsmuster ergab. Daraufhin wurden Methoden entwickelt, die

eine Bestimmung der Stöchiometrie von Zelloberflächen-Proteinkomplexen und die Erfassung umfangreicher Trajektorien zur Bewegungsanalyse ermöglichen.

Im Weiteren wurden die zuvor genannten Methoden zur genauen Überprüfung der Mobilität, Endozytose und der Charakterisierung der rückläufigen Dynamik der repräsentativen Rezeptoren von zwei verschiedenen Membranrezeptoren Klassen, des Parathormon-Rezeptors (Engl. the parathyroid hormone receptor), der zu der G-Proteingekoppelter Rezeptor Gruppe (GPCRs) gehört und der Rezeptoren der knochenmorphogenetischen Proteine (BMPs) verwendet.

BMPs aktivieren SMAD- und non-SMAD Signalkaskaden und als ein Bestandteil des TGF- β -Signalsystem sind sie in die Proliferation, die Differenziation, die Chemotaxis und die Apoptose involviert. Zwei BMP Rezeptor Typen, BMP Typ I und BMP Typ II (BMPRI und BMPRII) sind nötig für die effektive Signalwirkung. Offenbar sind die Bewegungsmuster für BMPRI und BMPRII sehr unterschiedlich, was hier die Genauigkeit des Signals festlegt. Non-SMAD Kaskade und die nachfolgende Differenzierung von den Osteoblastenzellen benötigt das abgegrenzte Bewegungsmuster von BMPRI. Daraus folgert, dass die laterale Mobilität ein Hauptmechanismus in der SMAD gegen non-SMAD Signalwirkung während der Differenziation ist.

Das abgegrenzte Bewegungsmuster war auch für den Parathormon Rezeptor (Engl. the parathyroid hormone receptor) (PTHr1), der in die Calcium Homeostase und den Knochenumbau involviert ist, in den Studien zu beobachten. In diesen Studien wurden fünf Peptide Ligande, spezifische Teile von dem PTH: hPTH(1–34), hPTHrP(107–111)NH₂; PTH(1–14); PTH(1–28) G¹R¹⁹, bPTH(3–34), von denen die ersten vier zu der Agonistengruppe und der Letzte zu der Antagonistengruppe gehören, in verschiedenen Konzentrationen mit lebenden COS-1 und AD293 Zellen verwendet. (oder aufgebracht)

Eine der Hauptfragen war die Festlegung der Rate der PTHr1 Internalisierung und des Recycling in dieser Forschung. Im Allgemeinen reduziert Internalisierung die Stärke der Signale, die von den G Proteinen kommen und durch die Rezeptoren übermittelt (die Desensibilisierung) werden. Durch den Rücklauf werden die Rezeptoren wieder sensibilisiert, degradiert und können somit an anderen Signalkaskaden ankoppeln (zB. MAP-Kinase).

Die Determinanten der Internalisierung sind das Hauptthema in den aktuellen Studien, da sie der Schlüssel zum besseren Verständnis der Internalisierung und zu den nachfolgenden biologischen Antworten sind.

Die Internalisierung von dem PTH Rezeptor verläuft entsprechend des Clathrin-coated Pit Weges mit der Teilnahme von β -arrestin2 und ist durch den Ligand eingeleitet, der zur Aktivierung von adenylyl cyclase (via G_s), und phosphatidylinositol-specific phospholipase C_β (via G_q) führt.

Zusammenfassend ist diese Arbeit unter Verwendung von Einzelmolekül-Mikroskopie mit der neuen ACP-Quantumpunktmethoden sowie standard Markierungsmethoden ein komplexes Studium über die IL-5R β c Rezeptoren, die BMP Rezeptoren und den PTH Rezeptor.

1

ACP - acyl carrier protein as a covalent linkage between receptor and quantum dot for single-molecule studies

Single-molecule studies reveal crucial information about mobility, stoichiometry, molecular interactions and the function of particular proteins. The most problematic issues within this technique are the proper choice of the fluorophore and the type of its biochemical attachment.

A method that attains a highly explicit linker of comparatively little size and calculable 1:1 fluorophore-to-receptor labeling stoichiometry was evolved that amalgamates usage of acyl carrier protein (ACP) and coenzyme A (CoA)-functionalized quantum dots. This strategy enables to affix quantum dots covalently to transmembrane receptors and is therefore highly useful for single molecule tracking, internalization and trafficking studies.

Biotechniques. 2010 Aug; 49(2):574-9

Zelman-Femiak M, Wang K, Gromova KV, Knaus P, Harms GS

1.1. Introduction

Signal transduction cascades are initiated by and depend ultimately on specific protein interactions in the plasma membrane. The most common trigger for the complex cellular responses is at first binding of a ligand to a receptor which next activates downstream signaling pathways. The study of the early events in the signaling cascades seems to be crucial issue to fully realize these processes. In order to gain more detailed information about dynamics and character of the membrane receptor interactions it is essential to follow the processes at a single-molecule level in real-time. Single-molecule microscopy is one of the decisive methodologies that allows to clarify cellular signaling in both spatial and temporal dimensions. Single-molecule microscopy not only enables determination of the protein interactions but also their motion, local stoichiometry, existing subpopulations and unique functions of particular molecules. Two issues that may affect efficacy of this technique are the usage of the proper fluorophore and the type of its biochemical attachment (1-4).

For the purpose of analyzing molecular mobility and determining specific localization of particular molecules high signal-to-background ratios and acquisition rates as well as inflexible, of a minimal size fluorophore are required (5,6). Fluorescent fusion proteins are frequently used for receptor labeling in single-molecule studies (7-10). Fluorophores are then covalently bound to cysteine or amino reactive groups of the receptor. Alternatively, small protein tags for the link between the dye and the membrane protein are applied (11).

Currently, next to labeling with standard organic fluorophores, labeling techniques with quantum dots (QD) are ascertained. Quantum dots have definite advantages over organic dyes as they produce much stronger fluorescence signals and have increased resistance to photobleaching. Concerning the size of QDs, they are approximately ten times smaller than latex beads and nearly the size of fluorescent proteins (12,13).

Most commonly used are quantum dots conjugated to antibodies (1,3), what adds to the radius of the QD approximately 10nm (1,3,4), influences registered motion and interferes with acquiring precise data. Maintained is then the wish of decreasing the linkage for the quantum dot labeling system and to overcome difficulties that long-tailed attachment introduces (14-17). Conjugation of the quantum dots to primary F_{ab}

fragments shows already signs of a substantial improvement. However, still infant are direct QDs binding and labeling methods of the receptors (1-4). They can be attained by amino or cysteine reactions or by exposing the biotinylated membrane protein to either quantum dots coated with streptavidin or to its truncated version, m-streptavidin that consists of 159 amino acid residues (18,19). An alternative scheme for direct labeling represents a fusion protein that includes a HaloTag, which is 296 amino acid modification of haloalkane dehydrogenase and is capable to create a covalent binding with a chloroalkanelabeled quantum dot (20,21).

Despite of existing a wide variety of labeling techniques which can be applied for biological imaging and receptor analysis (22-24), chiefly are those noncovalent or inapplicable for quantum dot labeling. However, a bunch of stabile methods with organic fluorophores found application in single-molecule microscopy, for instance, hexahistidine (13,26,27), FIAsh (25), Q-tag (29) and biotin acceptor peptide exist (28).

Effective labeling and tracking of single receptors on living cells enables the 77 amino acid acyl carrier protein (ACP) which can be reacted with coenzyme A (CoA) coupled to organic dyes or biotin (30) in the presence of phosphopantetheinyl transferase (PPTase) as a catalyst. ACP is smaller than similar SNAP and CLIC tags (22-24), and its fusion maintains the biological activity of receptors. Additionally, ACP binds CoA in a covalentlike manner what guarantee specificity and effectiveness of this reaction. Benefits of tracking and conducting internalization studies with ACP-CoA and organic fluorophores were presented on G protein-coupled receptors (GPCRs) (9,10) and AMPA receptors (31). Unknown, so far, has been a protocol for the direct QD labeling of the receptors containing the ACP tag.

In this study a QD-ACP labeling method is presented. The QDs attach covalently to the CoA molecules through activated thiol groups. A 1:1 QD:CoA ratio is provided due to the presence of amine blocking groups applied beforehand on the containig free amine groups quantum dot coating layer. The efficacy of the QD-ACP labeling technique is shown on the parathyroid hormone receptor (PTHr) and the bone morphogenetic protein type II receptor (BRII). For proper comparison each of the receptors are tracked and labeled also with antibody QD conjugates. We demonstrate that ACP-CoA-QD labeling system as the shortest specific covalent quantum dot tethering system, allows more precise tracking, elongated tracking times and determination of behaviour of particular receptors at the membrane, during internalization and postinternalization trafficking events.

1.2. Results & Discussion

Recently multiple labeling methods involving covalent attachment of fluorophores have been devised. The goal of this study was to invent a direct and uncomplicated QD labeling technique utilizing possibly short QD tether to amend tracking, internalization and visualizing trafficking events of particular receptors. We contrived a system based on the ACP, already known an extracellular fusion protein tag for receptors (30). First, to enable QD covalent binding to the ACP, QDs had to be coupled to CoA. We applied commercially available quantum dots that comprise of nanometer-scale CdSe core coated with an additional ZnS semiconductor shell and further with a polymer shell with extraneous free amine groups, which sequentially we blocked with a befitting concentration of amine blocking groups. Final, thiol-reactive chemistry resulted in obtaining QD-CoA with 1:1 ratio. (Figure 1A).

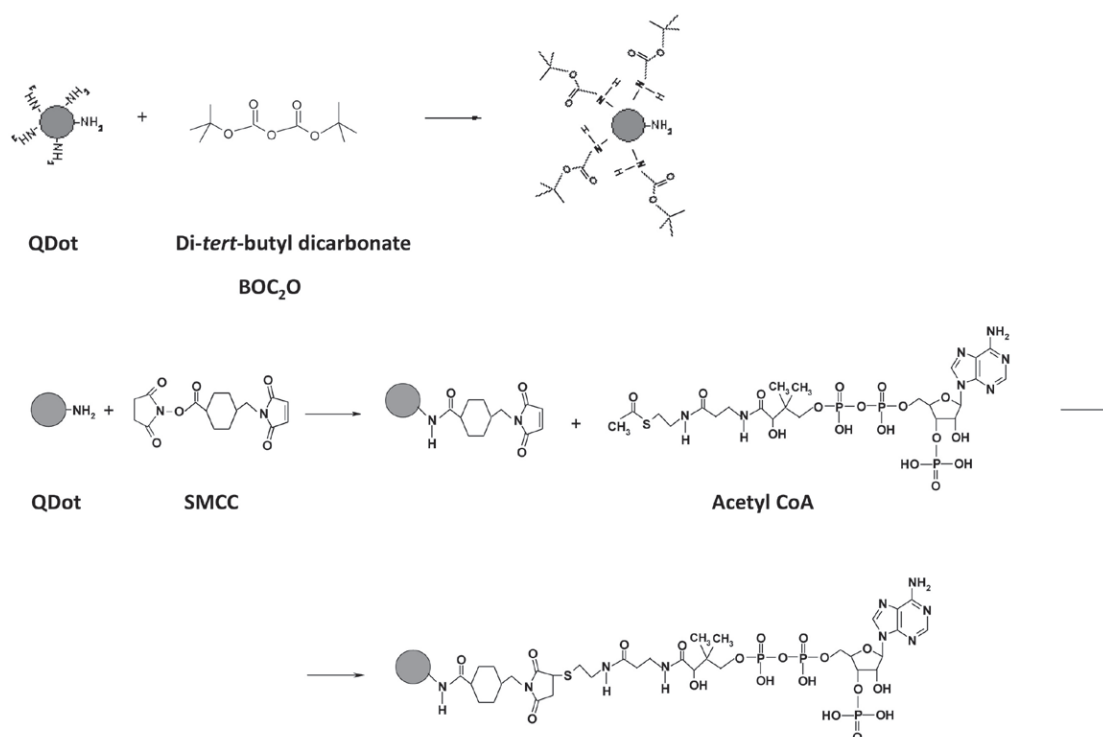
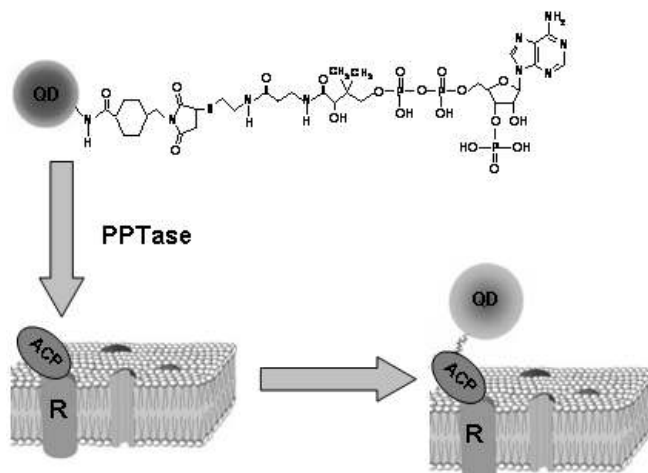


Figure 1A. The QD blocking and functionalization to the CoA. The majority of free amines on the QDs are blocked with the t-Boc. The remaining amines are functionalized with the SMCC so that at most, only one SMCC is functionalized to a QD. The CoA is then directly linked to the QD from the direct maleimide-thiol reaction.

ia.



ib.

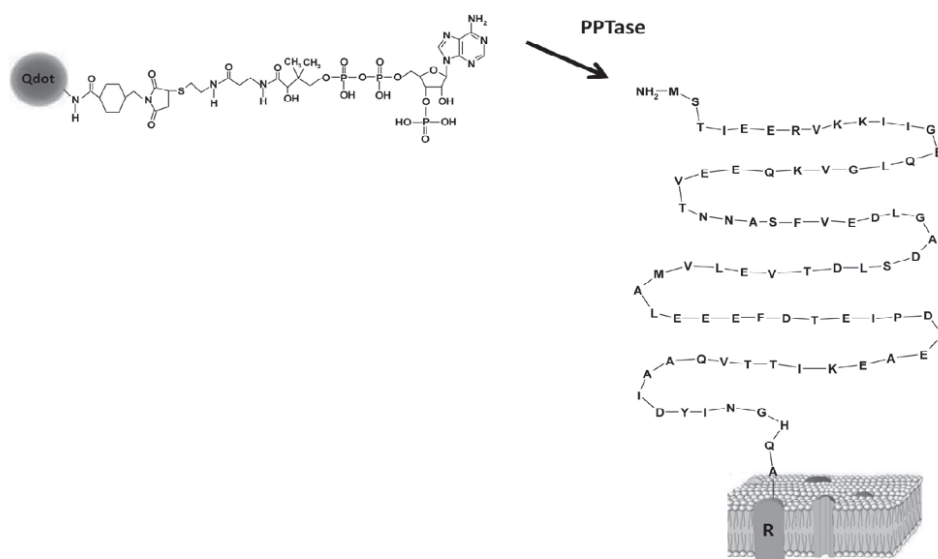


Figure 1B. Schematic diagram of labeling technique. By application of the enzyme PPTase, a single QD-CoA is transferred to the ACP protein fused to the receptor (**ia,ib**). Additionally, the small 77-amino acid sequence added to the receptor's extracellular domain is shown here (**ib**).

Next, the binding specificity of CoA-QDs to ACP-receptor under conditions of the enzymatic reaction with PPTase was examined (Figure 1B). We chose two membrane receptors to be ACP extracellularly tagged: a truncated PTHR (32) and a truncated BRII (33, 34), termed ACP-PTHr-TC and ACP-BRII-TC1, respectively. ACP-BRII-TC1 is the shortest BRII mutant which has the stop codon inserted directly before the kinase domain and lacks nearly all of the cytoplasmic tail of the receptor. The ACP tag is fused at the N terminus of the BRII-TC1. ACP-PTHr-TC corresponds to the PTH type 1

receptor lacking transmembrane domains III to VII and the 150-amino acid C terminus and has ACP crammed in the N-terminal ligand binding region.

HEK293 cells transiently transfected with appropriately low amounts of either ACP-PTHR-TC or ACP-BRII-TC1 after CoA-QD labeling exhibited the receptors efficiently and with the intensity applicable for the single molecule tracking at the plasma membrane (Figure 2, A and B). To affirm the explicitness of the ACP reaction we utilized solely CoA-QDs without the PPTase enzyme on the transfected HEK293 cells. No attachment of CoA-QDs was observed (Figure 2, A and B). A similar outcome, even upon the PPTase application, was achieved with nontransfected cells. Evidently, the signals registered on the transfected cells derived from the quantum dot labeled receptors (Figure 2C).

Besides verifying the specificity of our method, we also intended to make a comparison between the efficiency of CoA-QD system and labeling with antibody conjugated QDs on the transfected cells. For that reason the QD-CoA-ACP-labeled receptor was juxtaposed with the extracellularly HA-tagged BRII-TC1 (33,34) stained with mouse anti-HA primary and anti-mouse-F_{ab}-QD-conjugated secondary antibody. The average number of receptors per cell appeared to be similar in both cases (Figure 2, B and D).

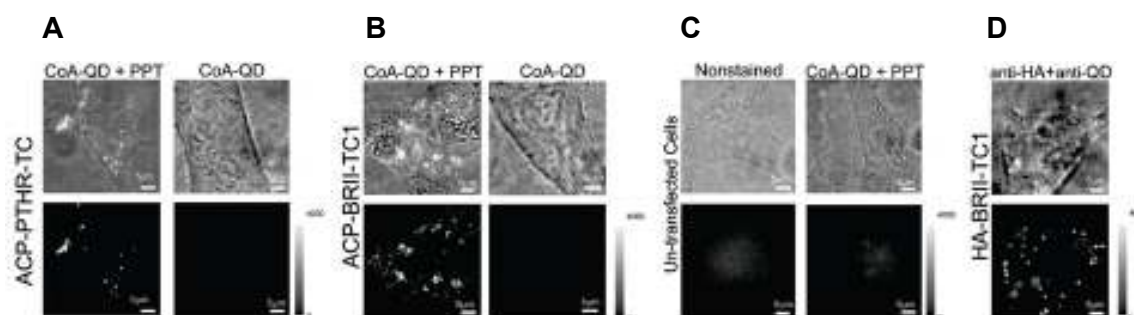


Figure 2. Characterization of the ACP-CoA-QD labeling of receptors on living cells. Fluorescent images are shown at the bottom and the corresponding transmission images are presented above. (A) CoA-QD labeling of HEK293 cells transfected with ACP-PTHR-TC followed by PPTase treatment displays many QDs (bottom left). Non-PPTase-treated cells show no QDs (bottom right). (B) CoA-QD labeling of HEK293 cells transfected with the ACP-BRII-TC1 plasmid followed by PPTase shows many QDs (bottom left), while without PPTase treatment, there are no QDs (bottom right). (C) Negative control of nontransfected HEK293 cells without (left) and with (right) CoA-QD and PPTase treatment. (D) Antibody-QD labeling of transfected HEK293 cells (transmission image, top) with the HA-BRII-TC1 plasmid with both the primary anti-HA antibody and secondary Fab antibody QD conjugate showing many QDs (bottom). All intensity scaling is in photons/5 ms.

Next, we tracked ACP-PTHR-TC marked covalently with CoA-QD on living cells. Whereas the data on the diffusion of the whole length PTHR receptor were known

(37), the type of the mobility and the role of this intensely truncated receptor were not determined. We applied TIRF microscopy to image the receptors on the basolateral surface of cells (Figure 3A). During tracking, we could pinpoint long (>50 step) traces of singular QD-receptor complexes, initially signifying free diffusion both before and after PTH addition, with subsequent fast internalization (Figure 3B, ia and ib). A small subpopulation of QD-receptor complexes exhibited limited mobility as well without as with ligand stimulation and mostly lasted long before internalizing or did not undergo internalization at all (Figure 3B, iia-iic). The movement of each individual QD-receptor complex was analyzed before and after ligand application to define the average motion (Figure 3C). Before PTH addition the QD-receptor complexes diffused in a partially confined manner on the membrane with a diffusion coefficient of $0.014 \pm 0.002 \mu\text{m}^2/\text{s}$ and a confinement coefficient $c = 0.739 \pm 0.041$. The QD-receptor complexes that endured at the membrane >10 min after PTH application displayed slow movement with the average motion of $0.00033 \pm 0.00005 \mu\text{m}^2/\text{s}$, what corresponds with the values barely above of the ascertained positional accuracy.

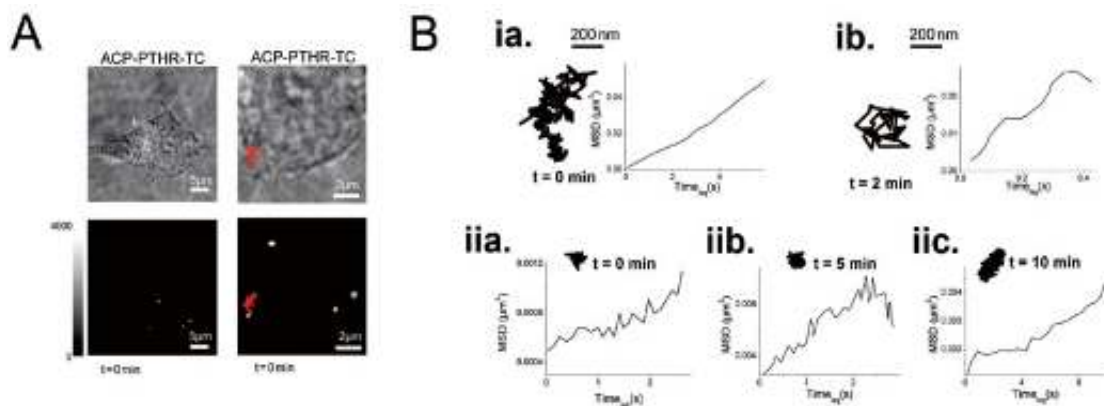


Figure 3A-B. Tracking of the surface mobility and internalization of ACP-PTHR-TC in live HEK293 cells. (A) Transmission (upper) and TIRF images (lower) of the CoA-QD-labeled ACP-PTHR-TC on HEK293 cells (left). Two traces in a magnified portion of the left image are shown in red and green (right). (B) Traces and plots of mean square displacement (MSD) versus time lag for each track of the two individual QD-receptor clusters from panel A. Before ligand addition, the receptor (i) was freely but slowly mobile ($0.003 \pm 0.001 \mu\text{m}^2/\text{s}$) and became more mobile ($0.021 \pm 0.005 \mu\text{m}^2/\text{s}$) 2 min after addition of 2.5 nM PTH. Zero, 5, and 10 min after PTH addition, the receptor (ii) displayed extremely confined motion ($0.0002 \pm 0.0001 \mu\text{m}^2/\text{s}$, $0.00083 \pm 0.00008 \mu\text{m}^2/\text{s}$, and $0.00005 \pm 0.00001 \mu\text{m}^2/\text{s}$, respectively).

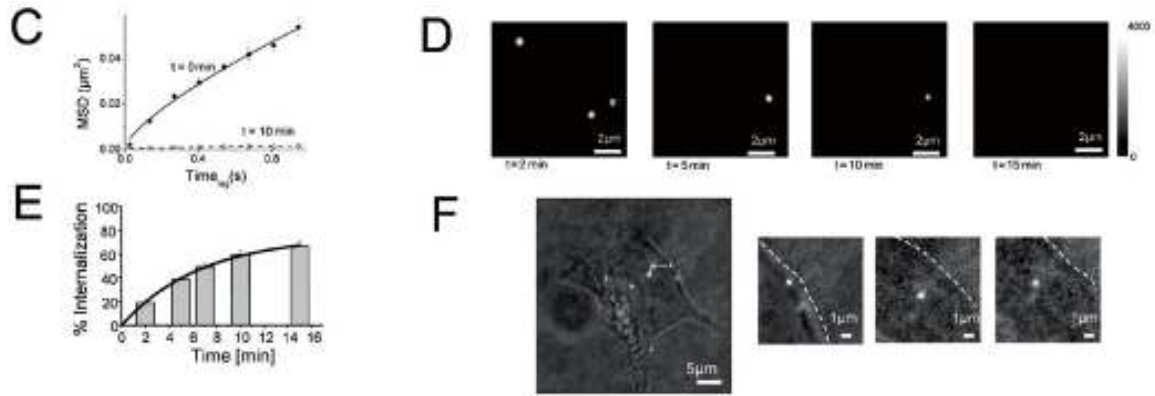


Figure 3C-F. Tracking of the surface mobility and internalization of ACP-PTHR-TC in live HEK293 cells. (C) The average motion was determined by probability analysis (see the “Materials and methods” section) and plotted as MSD versus time lag. The motion before PTH addition ($t = 0$ min) is indicated by the solid line with dark circles and after PTH addition by the dotted line with open circles. (D) Four images acquired at 2, 5, 10, and 15 min after ligand application display the internalization behavior for the zoomed image from panel A. (E) Temporal statistics from more than 10 cells for the internalization of ACP-PTHR-TC after addition of 2.5 nM PTH. (F) Trafficking of ACP-PTHR-TC receptor from the membrane into the cell. Overlay fluorescence and transmission image of four QD-receptor complexes with one trace showing two consecutive steps from the membrane (first image). Zoomed images (right three) of the QD-receptor complex at the membrane in the first image of the sequence with the same trafficked receptor complex (second image) and 2 and 3 min later (third and fourth images). Intensity scaling in panels A and D is in photons/5 ms.

Due to the ~ 1 order of magnitude difference in length between the shorter ACP-CoA-QD and the longer anti-HA/antimouse- F_{ab} -QD labeling, we decided to compare the motion of the receptors marked with each of the methods. The ACP-BRII-TC1 and HA-BRII-TC1 were tracked on cells before and after addition of BMP-2. In the absence and presence of ligand, the ACP-BRII-TC1 and HA-BRII-TC1 showed freely diffusing behavior (Figure 4, A and B) until just before the receptors internalized, whereupon the motion either significantly slowed $D_{\text{lat, ACP, 10 min after}} = 0.0004 \pm 0.0002 \mu\text{m}^2/\text{s}$ or became confined to regions of $\sim 270 \pm 20$ nm in diameter. Noticeably, the diffusion trajectories from the HA-tagged and anti-HA/antimouse- F_{ab} -QD labeled receptors invariably seemed to exhibit a larger movement, which, however, did not lead to a significant enlargement of the diffusion coefficient of the average mobility behavior (Figure 4B), where before BMP-2 application $D_{\text{lat, ACP, before}} = 0.014 \pm 0.002 \mu\text{m}^2/\text{s}$ and $D_{\text{lat, HA, before}} = 0.018 \pm 0.004 \mu\text{m}^2/\text{s}$.

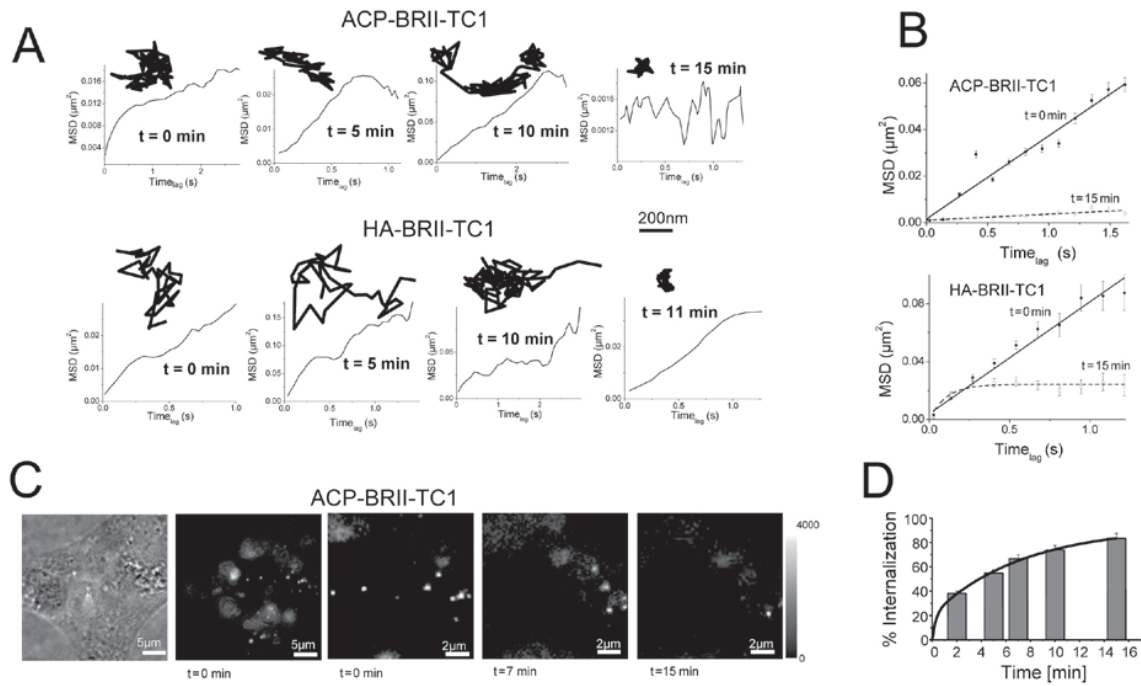


Figure 4. Tracking and internalization of the BRII-TC1 receptor on HEK293 cells. (A) Comparison of tracking from QD-receptors with ACP-CoA-QD labeling (upper) and HA/anti-HA/anti-mouse-Fab-QD labeling (lower) with MSD versus time lag plotted for each track after addition of 1 nM BMP-2. **(B)** The average motion was determined by probability analysis (see the “Materials and methods” section) and plotted as the MSD versus time lag of all ACP-BMP-II-TC1 (top graph) and HA-BMP-II-TC1 (lower graph) receptors before (dotted line with open circles) and after (solid line with dark circles) ligand addition. **(C)** Transmission (first image) and TIRF images (right four) of the CoA-QD ACP-BRII-TC1 on HEK293 cells acquired at 0, 7, and 15 min after 1 nM BMP-2 addition (right three magnified images are of the same region at t = 0, 7, and 15 min) to display the internalization behavior. Intensity scaling is in photons/5 ms. **(D)** Temporal statistics from >10 cells for the internalization of ACP-BRII-TC1 after 1 nM BMP-2 addition.

We investigated the internalization actions of both ACP-QD-labeled receptors as next. The analysis of the TIRF and wildfield images of the basolateral surface of the cells was conducted for instances when a QD-receptor complex would internalize and vanish from the membrane in longer timelapse sequences. Figure 3D and Figure 4C present examples of time-lapse internalization of the ACP-PTHR-TC and the ACP-BRII-TC1, respectively. Despite the fact that all QD-receptor complexes in the example displayed for ACP-PTHR-TC (Figure 3D) internalized, on average only 60% of receptors completely internalized with a single exponential rate of ~0.1 QD-receptor complex per minute (Figure 3E). More than 80% of the ACP-BRII-TC1 QD-receptors internalized with an aeventent bi-exponential rates of 0.1 and 1 QD-receptor complex per minute (80% and 20%, respectively; Figure 4D). Recycled QD-receptors were observed in all

cases (Figure 4C and Figure 5), however, any of the recycled receptors was included in the determination of internalization rate. Besides internalization rates, the technique is also applicable for larger scale trafficking events with broader imaging fields and increased penetration depths with slightly lower magnification and numerical aperture objectives. Numerous examples showed clearly that the receptor at the membrane could be tracked for internalization into the cells (Figure 3F).

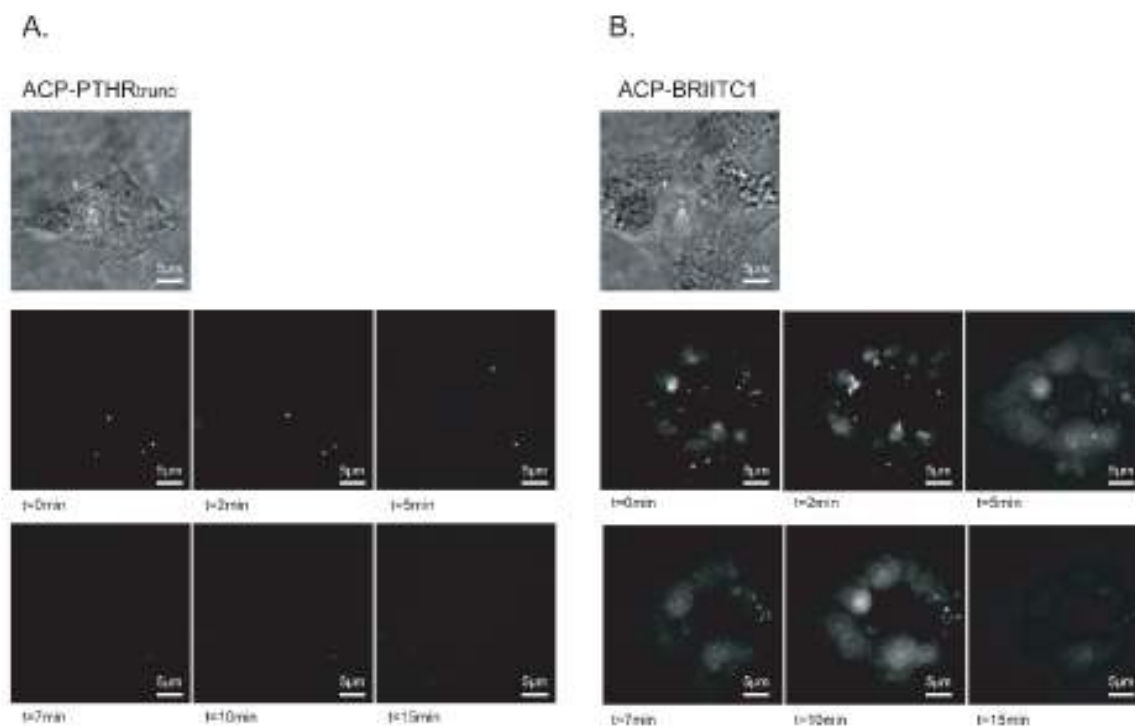


Figure 5. Internalization of the ACP-PTHr-TC and the ACP-BRII-TC1 receptors in living HEK293 cells. (A) Transmission (top left) and six TIRF images of the QD-CoA-labeled ACP-PTHr-TC acquired with lapsed time of 0–15 min after 2.5 nM PTH addition to display the internalization and recycling behavior for images from 3 A and D. (B) Transmission (top right) and fluorescence images of the CoA-QD ACP-BRII-TC1 on HEK293 cells (right) acquired before ($t = 0$ min) and after 1 nM BMP-2 with lapsed time of 2–15 min to display the internalization behavior (from Figure 4C).

In this study, we demonstrated our labeling method on decoy versions of the PTH and BRII transmembrane receptors, which both contain the ligand binding site but are deficient of the intracellular domain indispensable for signaling. The ACP technique provided efficient and highly specific labeling, what together with the excellent stability of the QDs enabled to perform internalization analysis of the receptors with minute

timescale time-lapse imaging to discern trafficking of individual receptors from the membrane into the cell and to also monitor recycling rates.

The tracking of the receptors showed that ACP-QD labeling characterized slightly lower mobility than antibody-QD labeling. We elucidate reduced mobility as the consequence of the shorter linker between the receptor and QD. Besides QD-receptor linkage, also truncation of the receptors could influence their movement. High and free diffusion mobility was expected from the truncated receptors, particularly when compared to studies carried out on the full-length PTHR and BRII (37) however, truncated receptors displayed only moderate but still free diffusion. Without BMP-2 stimulation a free diffusion of the ACP-BRII-TC1 was observed that support the observation that it does not bind to other receptors in the absence of the ligand (33,34,38). Ligand application resulted in incomplete internalization of the ACP-PTHRTC receptor what agreed with data previously gathered on truncation mutants of this receptor (39). Ligand addition caused nearly complete internalization of the ACP-BRII-TC1, which can be explained by binding to the epidermal growth factor pathway substrate 15 related protein (EPS15R), which is constitutively present in clathrin-coated pits (CCPs), the main internalization route of BRII (33).

We propose that binding to EPS15R steers the ligand-activated BRII-TC1 into CCPs, yielding in reduced mobility of the receptor, confinement to a region the size of CCPs, and the almost full internalization of this decoy receptor.

In the further projects, the ACP-QD labeling technique can be useful in the mobility analysis, internalization dynamics and trafficking studies of the wide variety of the membrane receptors as well as their specific signaling mutations. With the usage of the newly described 12-amino acid CoA binding domain (40,41) and recently delineated smaller and biologically benign QDs and nanoparticles (12,13,18) ACP-QD labeling can become the smallest, brightest, most specific, and most stable covalent labeling for tracking, internalization, and trafficking studies of individual receptors, what in combination with recently reported methods for 3-D tracking (42) would make it possible to determine the entire fate of individual receptors.

1.3. Materials and methods

1.3.1. Plasmid construction of ACP-PTHR-TC and ACP-BRII-TC1

Conflating the ACP to the N terminus of truncated human parathyroid hormone receptor PTHR-TC or to the N terminus of the truncated human type II bone morphogenetic receptor BRII-TC1 was generated analogously to priorly described N-terminally tagged GFP-PTHR (32) or BMP-HA and -myc receptors (33,34).

The PCR products of ACP and respective protein fragments were subcloned into pcDNA3 (Invitrogen, Karlsruhe, Germany) resulting in final constructs as follows: the ACP-PTHR-TC consisted of truncated (102-270 aa) and not embracing pharmacologically insignificant residues 61-101 human PTHR, besides of two residues (from restriction sites) between the ACP C and the PTHR-TC N terminal tails and six-residues between the ACP N terminal tail and the signal peptide of PTHR.; the ACP-BRII-TC1 contained six-residues between the ACP C and the BRII-TC1 N terminal tails. All constructs were verified by sequencing.

1.3.2. Cell culture

HEK293 cells were grown at 37°C/5% CO₂ in DMEM solution (Sigma-Aldrich, Taufkirchen, Germany) with addition of 10% FCS (PAA Laboratories GmbH, Linz, Austria) and 1% penicillin/streptomycin (Sigma-Aldrich). For single-molecule imaging, cells were seeded into six-well plates containing glass coverslips (No. 1, round, 24 mm; Assistent, Sondheim, Germany). Cell transient transfections were performed with FuGENE 6 (Roche Applied Science, Indianapolis, IN, USA) or Effectene (Qiagen, Hilden, Germany) and application of 0.2 µg plasmid DNA per well.

1.3.3. Labeling

For labeling cells were incubated on the coverslips for 15–20 min at 37°C/5% CO₂ in 270 µL DMEM with 1% BSA (Sigma-Aldrich), 1.5 µM 6xHis- phosphopantetheinyl transferase (PPTase), and 0.3 nM CdSe/ZnS quantum dot-coenzymeA (QD-CoA) molecules conducted with the QD655 Qdot Antibody Conjugation Kit (NrQ22021MP; Molecular Probes, Invitrogen Detection Technologies, Eugene, Oregon, USA; Invitrogen, Karlsruhe, Germany) and conjugated with CoA (Sigma- Aldrich).

Tending to establish 1:1 CoA:QD ratio, t-Boc protective groups were used to block unreacted amine groups within the coating phase of 655 quantum dots. The quantity of free amines occurred to vary, thus the concentration of t-Boc was roughly estimated to proceed blocking in a way that statistically most of the quantum dots swilled from equivalently transfected cells. That indicated smaller than 1:1 CoA:QD ratio. Amines which did not undergo the reaction with Di-tert-butyl dicarbonate (Sigma-Aldrich) were exposed for reacting with lower molar ratios of succinimidyl 4 [N-maleimidomethyl] cyclohexane-1-carboxylate (SMCC; Perbio Science, Bonn, Germany). The melamide-QD was then conjugated to CoA (Figure 1A). Mentioned reaction steps were performed not only with 655 quantum dots but also with QD585 QDot Antibody Conjugation Kit (NrQ22011MP) and with the amine-reactive 520 nm Adirondack Green and 600 nm Fort Orange EviTags QDs from Evident Technologies (Troy, NY, USA). The PPTase plasmid was acquired from Kai Johnsson (University of Lausanne, Lausanne, Switzerland). Production and purification of the PPTase protein was conducted resembling previously published protocols (1).

Three times washing step with 500 μ L DMEM followed staining samples with quantum dots. During experiments cells were kept in 300 μ L DMEM.

The hydrodynamic radius of 655 quantum dots was appraised between 15-20 nm. The coenzymeA seemed to extend the length of the radius about 1–2 nm.

1.3.4. Ligands

Human parathyroid hormone peptide ligand hPTH, amino acids 1–34 (Bachem California, Torrance, CA, USA) was applied to bind the truncated human parathyroid hormone receptor. Human bone morphogenetic protein-2 (BMP-2; Sigma-Aldrich) was used to bind the truncated BRII-TC1. Ligands were diluted in PBS and added in concentrations from 1 nM to 10 nM, depending on the experiment.

1.3.5. Single-molecule microscopy

The experimental arrangement for single molecule imaging has been described in detail previously (35,36). Essentially, the samples were mounted onto an inverted microscope (Axiovert 200; Zeiss, Göttingen, Germany) equipped with a 100x objective (PlanNeofluor 100x, N.A. = 1.3; Zeiss), and illuminated for 5 ms with the 473-nm laser line of a diode laser (MBL-473-100; CNI Laser; Changchun, China) with excitation intensity of 0.5–1 kW/cm² and synchronized with the exposure of the Peltier-cooled electron-multiplying

charge-coupled device (EMCCD) camera system (CascadeII 512B; Roper Scientific, Tucson, AZ, USA). The synchronization was realized by the use of home-built electronics to set the exposure trigger from the CCD camera and an acousto-optic time-frequency shutter (AOTF; AA Opto Electronic, Orsay, France) to control the laser light excitation. This system provided exact timing of the illumination time, intensity, and wavelength. Fluorescence signals from the QDs were monitored through a dichroic mirror (DCLP525; Chroma, Bellows Falls, VT, USA) in combination with a band pass (HQ655/40 nm; Chroma). The total detection efficiency of the experimental setup was 13% for the QDs (QD655). Typically, 500 readouts of half the region of the full array (256 x 256 pixels in the image plane) of the CCD chip was acquired to the PC with a time interval of 27 ms. During the experiment time, the cells were kept at 37°C via an objective heater (Biopetechs, Boulder, CO, USA).

1.3.6. Total internal reflection single-molecule microscopy

The total internal reflection (TIRF) single-QD imaging and tracking were performed on a Leica AM TIRF system (Leica, Wetzlar, Germany). The TIRF microscope was customequipped from the manufacturer with a 100×, N.A. = 1.46 objective (Leica), a 405-nm, 50-mW diode laser (CUBE; Coherent, Santa Clara, CA, USA), and the EMCCD camera system (CascadeII 512B). The TIRF angle was adjusted electronically via software control down to penetration depths of 70 nm. The emission of the QDs was filtered with a custom inserted band pass filter (HQ655/40 nm; Chroma).

1.3.7. Data analysis

Data processing occurred in Matlab (MathWorks, Natick, MA, USA). Trajectories were constructed from the positional shifts of the QDs in consecutive images and analyzed following a method as described (8). For the analysis of the (r_i^2, t_{lag}) plots, a positional accuracy of 7 ± 2 nm in our measurements was considered, and results in a constant offset in r_i^2 of $0.000049 \mu\text{m}^2$ for all time lags (5). In brief, the lateral diffusion of Brownian particles in a medium characterized by a diffusion constant D is described by the cumulative probability distribution function for the square displacements, r^2 (43):

$$\bar{P}(r^2, t_{lag}) = 1 - \exp\left(-\frac{r^2}{r_0^2}\right) \quad [\text{Eq.1}]$$

$P(r^2, t_{lag})$ describes the probability that the Brownian particle starting at the origin will be found within a circle of radius r at time t_{lag} . Provided that the system under study segregates into two components, characterized by mean-square displacements r_1^2 and r_2^2 , and relative fractions α and $(1 - \alpha)$, respectively, Equation 1 becomes (8,43):

$$\tilde{P}(r^2, t_{lag}) = 1 - \left[\alpha \cdot \exp\left(-\frac{r^2}{r_1^2}\right) + (1 - \alpha) \cdot \exp\left(-\frac{r^2}{r_2^2}\right) \right] \quad [\text{Eq. 2}]$$

The cumulative probability distributions $P(r_i^2, t_{lag})$ were constructed for each time lag from the single-molecule trajectories by counting the number of square displacements with values $< r^2$, and subsequent normalization by the total number of data points (43). Probability distributions with $n > 1000$ data points were least-square fit to Equation 2, resulting in a parameter set $\{r_1^2(t_{lag}), r_2^2(t_{lag}), \alpha\}$, for each time lag, t_{lag} , between 0.027 and 1.6 s. This approach of fitting leads to a robust estimation of the mean-square displacements r_i^2 even when the mobility is not purely random (8). Examples of the data acquired can be found in Figure 6.

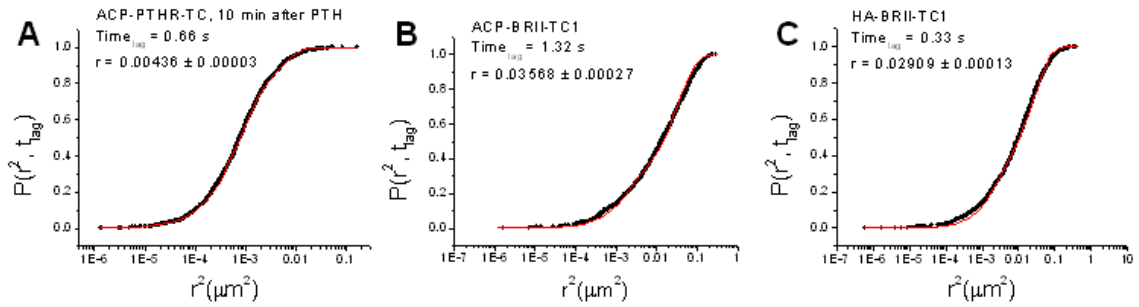


Figure 6. Examples of mobility probability distribution functions described above for the trajectory analysis. (A) Example from ACP-PTHR-TC 10 min after PTH at $t_{lag} = 0.66$ s. **(B)** Example from ACP-BRII-TC1 before BMP-2 addition at $t_{lag} = 1.32$ s. **(C)** Example from HA-BRII-TC1 before BMP-2 addition at $t_{lag} = 0.33$ s.

1.3.8. Mobility analysis

By plotting the mean square displacement (r_i^2) versus t_{lag} , the diffusional behavior of the respective populations of molecules is revealed. The (r_i^2, t_{lag}) data sets were fitted by a free diffusion model,

$$r_i^2(t_{lag}) = 4D_i t_{lag} \quad [\text{Eq. 3}]$$

where r_i^2 is proportional to time t_{lag} . When diffusion is hindered by obstruction or trapping in such a way that the mean square displacement is proportional to some power

of time <1 ($r_i^2 \sim t^\alpha$, $\alpha < 1$), it is called anomalous subdiffusion, and the diffusion constant becomes (8):

$$D = \Gamma t_{lag}^{1-\alpha}$$

[Eq. 4]

If $\alpha = 1$, then $r_i^2 \sim 1$, $D = \Gamma$ is constant, and diffusion is normal. When the mean-square displacement does increase with time but levels off to a constant value for longer time lags, this was described with a confined diffusion model. The confined diffusion model assumes that diffusion is free within a square of side length L , surrounded by an impermeable, reflecting barrier. Then the mean-square displacement depends on L and the initial diffusion coefficient D_0 , and varies with t_{lag} as (8,6):

$$r_i^2(t_{lag}) = \frac{L^2}{3} \left[1 - \exp\left(\frac{-12D_0 t_{lag}}{L^2}\right) \right]$$

[Eq. 5]

1.4. References

1. Alcor, D., G. Gouzer, and A. Triller. 2009. Single-particle tracking methods for the study of membrane receptors dynamics. *Eur. J. Neurosci.* *30*:987-997.
2. Pons, T. and H. Mattoussi. 2009. Investigating biological processes at the single molecule level using luminescent quantum dots. *Ann. Biomed. Eng.* *37*:1934-1959.
3. Chang, Y.P., F. Pinaud, J. Antelman, and S. Weiss. 2008. Tracking bio-molecules in live cells using quantum dots. *J. Biophotonics* *1*:287-298.
4. Kaji, N., M. Tokeshi, and Y. Baba. 2007. Single-molecule measurements with a single quantum dot. *Chem. Rec.* *7*:295-304.
5. Thompson, R.E., D.R. Larson, and W.W. Webb. 2002. Precise nanometer localization analysis for individual fluorescent probes. *Biophys. J.* *82*:2775-2783.
6. Kusumi, A., C. Nakada, K. Ritchie, K. Murase, K. Suzuki, H. Murakoshi, R.S. Kasai, J. Kondo, and T. Fujiwara. 2005. Paradigm shift of the plasma membrane concept from the two-dimensional continuum fluid to the partitioned fluid: high-speed single-molecule tracking of membrane molecules. *Annu. Rev. Biophys. Biomol. Struct.* *34*:351-378.
7. Harms, G.S., L. Cognet, P.H. Lommerse, G.A. Blab, H. Kahr, R. Gamsjager, H.P. Spaink, N.M. Soldatov, et al. 2001. Single-molecule imaging of l-type Ca(2+) channels in live cells. *Biophys. J.* *81*:2639-2646.
8. Lommerse, P.H., G.A. Blab, L. Cognet, G.S. Harms, B.E. Snaar-Jagalska, H.P. Spaink, and T. Schmidt. 2004. Single-molecule imaging of the H-ras membrane-anchor reveals domains in the cytoplasmic leaflet of the cell membrane. *Biophys. J.* *86*:609-616.
9. Jacquier, V., M. Prummer, J.M. Segura, H. Pick, and H. Vogel. 2006. Visualizing odorant receptor trafficking in living cells down to the single-molecule level. *Proc. Natl. Acad. Sci. USA* *103*:14325-14330.
10. Prummer, M., B.H. Meyer, R. Franzini, J.M. Segura, N. George, K. Johnsson, and H. Vogel. 2006. Post-translational covalent labeling reveals heterogeneous mobility of individual G protein-coupled receptors in living cells. *Chembiochem* *7*:908-911.
11. Sonnleitner, A., L.M. Mannuzzu, S. Terakawa, and E.Y. Isacoff. 2002. Structural rearrangements in single ion channels detected optically in living cells. *Proc. Natl. Acad. Sci. USA* *99*:12759-12764.
12. Liu, W., M. Howarth, A.B. Greytak, Y. Zheng, D.G. Nocera, A.Y. Ting, and M.G. Bawendi. 2008. Compact biocompatible quantum dots functionalized for cellular imaging. *J. Am. Chem. Soc.* *130*:1274-1284.

13. Dif, A., F. Boulmedais, M. Pinot, V. Roullier, M. Baudy-Floc'h, F.M. Coquelle, S. Clarke, P. Neveu, et al. 2009. Small and stable peptidic PEGylated quantum dots to target polyhistidinetagged proteins with controlled stoichiometry. *J. Am. Chem. Soc.* *131*:14738-14746.
14. Curry, A.C., M. Crow, and A. Wax. 2008. Molecular imaging of epidermal growth factor receptor in live cells with refractive index sensitivity using dark-field microspectroscopy and immunotargeted nanoparticles. *J. Biomed. Opt.* *13*:014022.
15. Huang, Y.F., H. Liu, X. Xiong, Y. Chen, and W. Tan. 2009. Nanoparticle-mediated IgE-receptor aggregation and signaling in RBL mast cells. *J. Am. Chem. Soc.* *131*:17328-17334.
16. Wiseman, P.W., P. Hoddellius, N.O. Petersen, and K.E. Magnusson. 1997. Aggregation of PDGF-beta receptors in human skin fibroblasts: characterization by image correlation spectroscopy (ICS). *FEBS Lett.* *401*:43-48.
17. Dorsch, S., K.N. Klotz, S. Engelhardt, M.J. Lohse, and M. Bunemann. 2009. Analysis of receptor oligomerization by FRAP microscopy. *Nat. Methods* *6*:225-230.
18. Howarth, M., W. Liu, S. Puthenveetil, Y. Zheng, L.F. Marshall, M.M. Schmidt, K.D. Wittrup, M.G. Bawendi, and A.Y. Ting. 2008. Monovalent, reduced-size quantum dots for imaging receptors on living cells. *Nat. Methods* *5*:397-399.
19. Howarth, M. and A.Y. Ting. 2008. Imaging proteins in live mammalian cells with biotin ligase and monovalent streptavidin. *Nat. Protocols* *3*:534-545.
20. Zhang, Y., M.K. So, A.M. Loening, H. Yao, S.S. Gambhir, and J. Rao. 2006. HaloTag protein-mediated site-specific conjugation of bioluminescent proteins to quantum dots. *Angew. Chem. Int. Ed. Engl.* *45*:4936-4940.
21. Zhang, Y., M.K. So, and J. Rao. 2006. Protease-modulated cellular uptake of quantum dots. *Nano Lett.* *6*:1988-1992.
22. Griffin, B.A., S.R. Adams, and R.Y. Tsien. 1998. Specific covalent labeling of recombinant protein molecules inside live cells. *Science* *281*:269-272.
23. O'Hare, H.M., K. Johnsson, and A. Gautier. 2007. Chemical probes shed light on protein function. *Curr. Opin. Struct. Biol.* *17*:488-494.
24. Yano, Y. and K. Matsuzaki. 2009. Tag-probe labeling methods for live-cell imaging of membrane proteins. *Biochim. Biophys. Acta* *1788*:2124-2131.
25. Liu, R., D. Hu, X. Tan, and H.P. Lu. 2006. Revealing two-state protein-protein interactions of calmodulin by single-molecule spectroscopy. *J. Am. Chem. Soc.* *128*:10034-10042.
26. Roullier, V., S. Clarke, C. You, F. Pinaud, G.G. Gouzer, D. Schaible, V. Marchi-Artzner, J. Pichler, and M. Dahan. 2009. High-affinity labeling and tracking of individual

histidinetagged proteins in live cells using Ni²⁺ trisnitrilotriacetic acid quantum dot conjugates. *Nano Lett.* 9:1228-1234.

27. Guignet, E.G., J.M. Segura, R. Hovius, and H. Vogel. 2007. Repetitive reversible labeling of proteins at polyhistidine sequences for single-molecule imaging in live cells. *Chemphyschem* 8:1221-1227.

28. Chen, I., M. Howarth, W. Lin, and A.Y. Ting. 2005. Site-specific labeling of cell surface proteins with biophysical probes using biotin ligase. *Nat. Methods* 2:99-104.

29. Lin, C.W. and A.Y. Ting. 2006. Transglutaminase- catalyzed site-specific conjugation of small-molecule probes to proteins in vitro and on the surface of living cells. *J. Am. Chem. Soc.* 128:4542-4543.

30. George, N., H. Pick, H. Vogel, N. Johnsson, and K. Johnsson. 2004. Specific labeling of cell surface proteins with chemically diverse compounds. *J. Am. Chem. Soc.* 126:8896-8897.

31. Kropf, M., G. Rey, L. Glauser, K. Kulangara, K. Johnsson, and H. Hirling. 2008. Subunitspecific surface mobility of differentially labeled AMPA receptor subunits. *Eur. J. Cell Biol.* 87:763-778.

32. Castro, M., V.O. Nikolaev, D. Palm, M.J. Lohse, and J.P. Vilardaga. 2005. Turn-on switch in parathyroid hormone receptor by a two-step parathyroid hormone binding mechanism. *Proc. Natl. Acad. Sci. USA* 102:16084-16089.

33. Hartung, A., K. Bitton-Worms, M.M. Rechtman, V. Wenzel, J.H. Boergermann, S. Hassel, Y.I. Henis, and P. Knaus. 2006. Different routes of bone morphogenic protein (BMP) receptor endocytosis influence BMP signaling. *Mol. Cell. Biol.* 26:7791-7805.

34. Nohe, A., S. Hassel, M. Ehrlich, F. Neubauer, W. Sebald, Y.I. Henis, and P. Knaus. 2002. The mode of bone morphogenetic protein (BMP) receptor oligomerization determines different BMP-2 signaling pathways. *J. Biol. Chem.* 277:5330-5338.

35. Steinmeyer, R., A. Noskov, C. Krasel, I. Weber, C. Dees, and G.S. Harms. 2005. Improved fluorescent proteins for singlemolecule research in molecular tracking and colocalization. *J. Fluoresc.* 15:707-721.

36. Michel, R., R. Steinmeyer, M. Falk, and G.S. Harms. 2007. A new detection algorithm for image analysis of single, fluorescence-labeled proteins in living cells. *Microsc. Res. Tech.* 70:763-770.

37. Wheeler, D., W.B. Sneddon, B. Wang, P.A. Friedman, and G. Romero. 2007. NHERF-1 and the cytoskeleton regulate the traffic and membrane dynamics of G protein-coupled receptors. *J. Biol. Chem.* 282:25076-25087.

38. Sieber, C., J. Kopf, C. Hiepen, and P. Knaus. 2009. Recent advances in BMP receptor signaling. *Cytokine Growth Factor Rev.* 20:343- 355.

39. Vilaradaga, J.P., C. Krasel, S. Chauvin, T. Bambino, M.J. Lohse, and R.A. Nissenson. 2002. Internalization determinants of the parathyroid hormone receptor differentially regulate beta-arrestin/receptor association. *J. Biol. Chem.* 277:8121-8129.
40. Yin, J., P.D. Straight, S.M. McLoughlin, Z. Zhou, A.J. Lin, D.E. Golan, N.L. Kelleher, R. Kolter, and C.T. Walsh. 2005. Genetically encoded short peptide tag for versatile protein labeling by Sfp phosphopantetheinyl transferase. *Proc. Natl. Acad. Sci. USA* 102:15815- 15820.
41. Zhou, Z., P. Cironi, A.J. Lin, Y. Xu, S. Hrvatin, D.E. Golan, P.A. Silver, C.T. Walsh, and J. Yin. 2007. Genetically encoded short peptide tags for orthogonal protein labeling by Sfp and AcpS phosphopantetheinyl transferases. *ACS Chem. Biol.* 2:337-346.
42. Katayama, Y., O. Burkacky, M. Meyer, C. Brauchle, E. Gratton, and D.C. Lamb. 2009. Real-time nanomicroscopy via three-dimensional single-particle tracking. *Chemphyschem* 10:2458-2464.
43. Schutz, G.J., H. Schindler, and T. Schmidt. 1997. Single-molecule microscopy on model membranes reveals anomalous diffusion. *Biophys. J.* 73:1073-1080.

BMP type I and II receptors mobility linked to non-SMAD/SMAD signaling

Bone morphogenetic proteins (BMPs) are members of the transforming growth factor β (TGF- β) superfamily and are entailed in the regulation of proliferation, differentiation, chemotaxis, and apoptosis (1). BMP signaling engages two types of transmembrane serine/threonine kinases, BMP type I and type II receptors (BMPRI and BMPRII, respectively). BMPs activate SMAD- and non-SMAD pathways and can elude a wide variety of biological responses. In this investigation the question about involvement of BMP receptors in the specificity of ligand-induced responses was tackled.

Single-molecule microscopy revealed an apparent divergence in the mobility of BMP receptors type I and type II. In further experiments the difference in motion of the receptors was juxtaposed according to the BMP signaling routes. The necessity of the confinement of BMP type I receptor was recognized for non-SMAD signaling and ensuing osteoblastic differentiation of precursor cells.

The conclusive postulate has been made that receptor lateral mobility navigates through SMAD versus non-SMAD signaling during differentiation.

Submission to Nature Cell Biology

Zelman-Femiak M*, Guzman A*, Knaus P, Harms GS

(* authors contributed equally to the work)

2.1. Introduction

Bone morphogenetic proteins (BMPs) embrace the vastest assemblage of the transforming growth factor β (TGF β) superfamily and actively participate in embryonic patterning and organogenesis (2,3), adult tissue homeostasis and regeneration (4,5,6). There have been four of type I and three of type II BMP receptors identified so far (7). It is also known that for effective signaling both type of receptors, that together create heterotetrameric complexes, are essential. After ligand is chained, sequentially BMP receptor type II (BMPRII) transphosphorylates BMP receptor type I (BMPRI) which in response phosphorylates the intracellular signaling proteins that belong to either SMADs or are members of mitogen-activated protein kinase (MAPK) pathways. This enables the initiation of respective SMAD and non-SMAD signaling cascades (8).

Multiplicity of biological processes that can be triggered through BMPs is still one of the most mysterious and fascinating riddle in the field. Some of factors that influence flow of the signal have already been found. One of the examples is the BMP ligand-receptor oligomerization which occurs in two different ways (9). The ligand can either target a preformed type I/type II heteromeric receptor complex (PFC) which show next a preference for SMAD-signaling. Alternatively, it can affix to its high affinity type I receptor guiding to recruitment of the type II receptor and formation of a BMP-induced signaling complex (BISC) that activates non-SMAD pathways such as MAPK cascades (10).

The course of signaling and internalization of BMP receptors can be also affected through the receptor localization within particular plasma membrane domains (11,12). Moreover, the discrepancy in the binding affinity of BMPs to receptors type I and II has been shown indicating analogously strong affinity of BMP-2 for BMPRIa and BMPRIb (K_D BMPRIa > BMPRIb \gg BMPRII) but perceptibly higher affinity of growth differentiation factor 5 (GDF-5), another member of the BMP family, for BMPRIb than for BMPRIa (K_D BMPRIb \gg BMPRIa > BMPRII) (13).

However, still many questions regarding BMP signaling machinery stay open. Single-molecule tracking could help to clarify and understand the governance of the BMP signals by observation of the individual BMP type I and II receptors in the context of their natural environment. Behavior of the receptors can be observed gradually, commencing with the absence of activatory ligand, during activation and finally

internalization. Single-molecule microscopy has already furnished insights into assembly and activation of signaling molecules such as EGFR (14). Varied mobility pattern before and after activation was presented for particular signaling molecules, e.g. the Ras molecule, and attributed to gathering of signaling complexes (15). Observed dwindling motion of TGF β receptor type I after TGF β stimulation seemed to match its heteromeric congregating with type II receptors (16).

In this study, the single-molecule microscopy has allowed to examine influence of receptor motion on the signaling pathways and to evince that lateral mobility of BMP receptors depends on the transmembrane domain and is essential for governing the SMAD- versus non-SMAD signaling under BMP stimulation.

2.2. Results & Discussion

2.2.1. BMP receptors type I and II have different lateral mobilities

Fluorescence recovery after photobleaching (FRAP) was applied to C2C12 cells expressing BMPRIa-YFP and BMPRII-CFP fusion constructs to examine diffusion of BMP receptors in living cells. FRAP analysis showed the recovery rate to differ and be double higher for BMPRII than for BMPRIa, what immediately indicated that receptor type I consists of bigger immobile subpopulation that decreases its total lateral diffusion (Figure 1a). Gathered data are in agreement with the previously presented fact that BMPRIa receptors strongly associate with DRM (11). Additionally, acceptor photobleaching exhibited a noticeable CFP increase for a FRET efficiency of 36% what clearly implies that BMPRIa receptors affiliate with BMPRII before ligand addition. This provides another convincing evidence for ligand independent so-called preformed complexes (PFCs).

Next, single-molecule microscopy was utilized to study mobility of BMP receptors labeled with two separate methods: 1) enzyme-mediated quantum dot (QD) labeling of acyl carrier protein (ACP)-tagged receptors (17) and 2) antibody-mediated QD labeling of HA- or Myc-tagged receptors.

Traces of individual QD labeled receptors and analysis of their mean square displacement (MSD) showed that BMPRIa and BMPRIb display mainly confined motion with a confinement size of < 100 nm (Figure 1b,c), what closely correlates with the low recovery rate and domination of immobile BMPRIa component in FRAP experiments. Importantly, both labeling techniques, ACP- and antibody-mediated led to the same result and no apparent discrepancy has been noticed between them (17). That puts the BMPRI membrane localization to be the main restrictive factor in receptor mobility.

BMPRII displayed two subpopulations with divergent mobility pattern, of which one showed a confined motion within regions of 200 nm or smaller (Figure 1e,f) mirroring the movement of BMPRIa and BMPRIb with diffusion coefficients of $0.004 \mu\text{m}^2/\text{s}$. Whereas the other subpopulation of much longer traces fits a free diffusion model in the mean square displacement (MSD) analysis (18) (Figure 1e,f) and reflects the high recovery rate in FRAP experiments (Figure 1a).

Again, results for ACP- and antibody-mediated labeling methods did not show any marked differences.

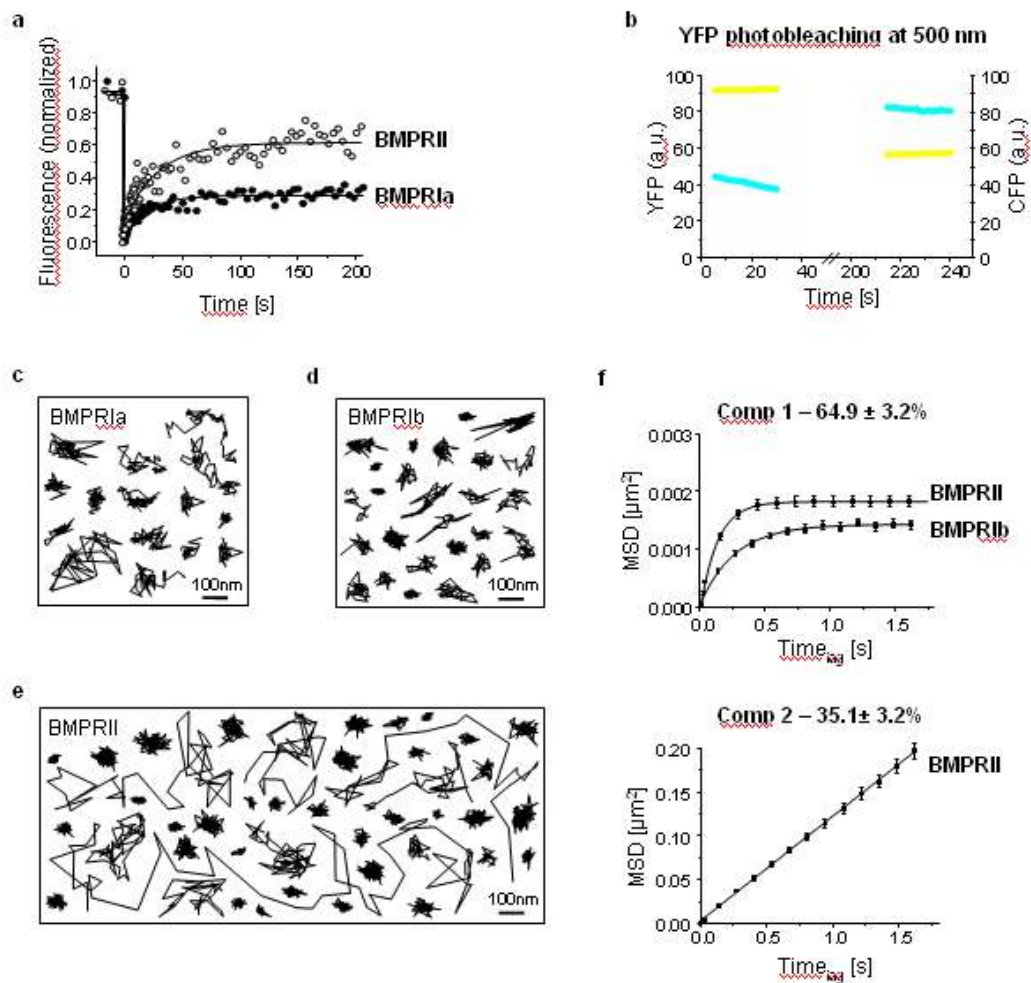


Figure 1. BMP receptors type I and II have different lateral mobilities. (a,b) Analysis and images of fluorescence recovery after photobleaching (FRAP) and fluorescence resonance energy transfer (FRET). Acceptor photobleaching of transiently expressed BMPRIa-YFP and BMPRII-CFP. Normalized fluorescence intensity before and after photobleaching is plotted vs. time. (c,d) Single-molecule tracking traces and analysis of BMPRIa and BMPRIb receptor mobility on cell surface. C2C12 cells expressing respective HA-tagged receptors were QD-labeled via tag-specific antibodies and subjected to the microscopy followed by mobility analysis. Representative movement trajectories of individual receptor molecules demonstrate the confinement of receptor mobility to a certain area. The scale bar represents 100 nm. (e) SPT-based mobility analysis of BMPRII. Cells expressing HA-tagged receptors were labeled, imaged and analysed analogous to Fig. 1c,d. Representative movement trajectories of BMPRII are shown. The scale bar represents 100 nm. (f) Average motion of receptors was determined by mean square displacement (MSD) analysis. MSD for each receptor type was plotted vs. time lag (t_{lag}) and the resulting functions fitted to mathematical models of confined and free diffusion. Data points from 5 independent experiments for each receptor type were pooled.

2.2.2. Effect of ligand application on the lateral mobility of BMP receptors

Impact of ligand application on BMP receptor lateral mobility was measured as the BMP stimulation was previously shown to augment heteromeric BMPRI/BMPRII

complex formation (9). After BMP-2 addition FRAP analysis indicated decreased BMPRII mobile fraction to the level of BMPRIa what signifies that receptors get immobilized within minutes after ligand stimulation (Figure 2a). FRET studies were conducted to verify whether assembling with BMPRIa could be responsible for the immobilization of BMPRII. After BMP-2 application FRET increase of 10% to 20% was observed implying the existence of ligand dependent BMPRIa/BMPRII complexes (Figure 2b).

Moreover, individual BMP receptors were monitored on living cells up to 30 min after BMP-2 (Figure 2c-e) or GDF-5 addition with the single-molecule microscopy technique. The mobility of BMPRIa and BMPRIb endured confined (Figure 2c,d,f) of a slightly smaller confinement size upon ligand stimulation than the one previously observed in ligand absence (compare MSD analysis in Figure 1f and 2f). Interestingly, BMPRII mobility altered drastically approximately 5 min after BMP-2 stimulation and displayed one population of solely confined motion with the similar to BMPRI diffusion coefficient of $0.004 \mu\text{m}^2/\text{s}$ and confinement size of 100 to 200 nm (Figure 2e,f). This mobility abating can be correlated with the formation of BMP-induced signaling complexes (BISCs) (10).

To examine ligand impact on the differences in distribution of endogenous BMPRII cell surface biotinylation was combined with isolation of detergent-resistant membranes (DRMs) by sucrose gradient fractionation. Co-fractionation of the respective molecule with DRM-markers (e.g. Caveolin1) is the sign of its association with membrane microdomains. Prior to ligand addition endogenous BMPRII was present in both DRM- and non-DRM fractions at the cell surface and shifted to DRM fractions already 5 min after BMP-2 stimulation (Figure 2g,h). This suits the mobility data of BMPRII showing decrease of its motion upon ligand stimulation (Figure 1a,e,f and 2). To further examine motionless of BMPRII in the context of the heteromeric complex formation FRET and single-molecule studies with a BMPRII intracellular truncation mutant (BMPRII-TC1) lacking the ability to build preformed complexes with BMPRI (10) were performed. No FRET before ligand addition and only a 10% FRET increase upon BMP-2 ligand stimulation were noticed. In single-molecule analyses, the BMPRII-TC1 had solely a freely diffusing population ($D = 0.02$ to $0.05 \mu\text{m}^2/\text{s}$).

Furthermore, ligand application only slightly induced the confinement and immobilization of this receptor on the membrane giving values similar to already reported on HEK293 cells (17) indicating immobility correlation to oligomerization.

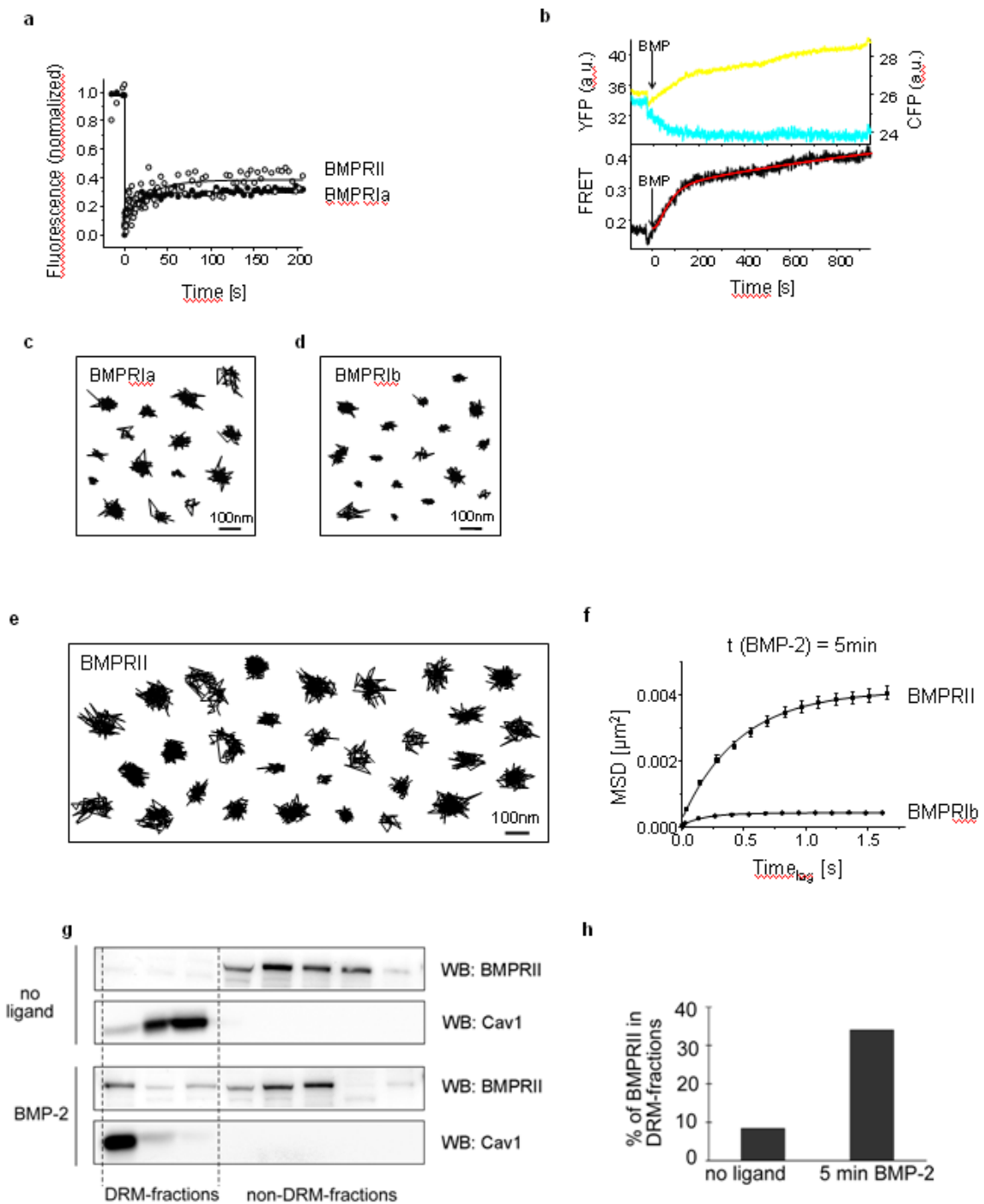


Figure 2. Lateral mobility of BMPRII is reduced upon ligand stimulation.

(a) FRAP analysis of BMPRIa and BMPRII lateral diffusion upon BMP-2 stimulation. BMPRIa-YFP and BMPRII-CFP constructs were transiently expressed and imaged as in Figure 1a. Normalized fluorescence intensity before and after photo-bleaching upon stimulation with BMP-2 is plotted vs. time. Percentage of recovery for both receptors is shown in the histogram. The reduced recovery rate of BMPRII reflects the increased amount of immobilized BMPRII on cell surface.

(b) Time resolved FRET on individual cells expressing BMPRIa-YFP and BMPRII-CFP constructs indicated an increase of FRET after ligand.

(c-e) SPT traces of BMPRIa, BMPRIb and BMPRIILF after 5 min BMP-2 stimulation. C2C12 cells expressing the respective HA-tagged receptor were starved, QD-labeled and imaged upon BMP-2 stimulation as described for the same cells in Figure 1c. Representative trajectories of BMPRIa, BMPRIb and BMPRII LF show a comparable confined mobility for all receptors after ligand stimulation. Scale bar represents 100 nm.

(f) Analysis of BMPRI and BMPRII MSD vs. time shows a comparable average mobility for both receptor types after BMP-2 stimulation. Data points from five independent experiments were pooled.

(g,h) Enhanced DRM-association of endogenous BMPRII upon ligand stimulation as assessed by co-fractionation with the DRM-marker Caveolin1. C2C12 cells were starved and stimulated with BMP-2 for 5 min. After cell surface biotinylation cells were used for sucrose gradient fractionation and subsequent streptavidin precipitation of biotinylated proteins. Precipitates were subjected to Western blot analysis. Quantification of Western blot analysis demonstrates the increased proportion of BMPRII in DRM-fractions after BMP-2 addition.

2.2.3. Modulating lateral mobility of BMPRI

BMPRIb was shown to have a strong biochemical association with cholesterol-rich membrane microdomains (11). Therefore, in this study experiments of cholesterol depletion by short treatments with methyl- β -cyclodextrin (M β CD) were performed to better understand the effect of cholesterol-rich microdomains on the confinement of BMPRIb motion. Already 5 min after application M β CD caused a gradual increase up to 180 nm in the confinement size of individual BMPRIb receptors (Figure 3a,b). After 60 min BMPRIb showed fully free diffusion (Figure 3c,d). As control for plasma membrane integrity under cholesterol depleting conditions the mobility of an independent transmembrane receptor was analysed under M β CD treatment. For this the transferrin receptor (TfR), a known non-DRM protein, was subjected to single-molecule analysis. Mobility pattern of TfR did not change under these conditions implying that the membrane integrity was not affected under M β CD treatment.

Furthermore, the role of caveolae - a subpopulation of DRMs containing Caveolin1 - was studied for BMPRIb mobility. Caveolae were previously shown to influence BMP signaling (11,19). Single-molecule analysis of siRNA-mediated knockdown of Caveolin1, which was performed in C2C12 cells stably expressing HA-tagged BMPRIb (C2C12-BMPRIb *wt*) and verified by Western Blotting prior to the imaging, displayed free diffusion-like motion of BMPRIb (Figure 3e,f). These data provide compelling evidence that localization of BMPRIb in cholesterol-rich membrane microdomains and specifically in caveolae is necessary to maintain the confinement of BMPRIb mobility.

Not only the chemical composition of membrane microdomains, but also interactions between membrane microdomains and cytoskeleton have been described previously (20,21,22). Obviously, any attachment to the cytoskeleton could be the factor hindering mobility of the BMPRIb receptors (23). That gave the reason to scrutinize the involvement of the microtubule network in the motionless of BMPRIb. Microtubule

disruption was performed by short term nocodazole treatment (up to 90 min) before imaging C2C12-BMPRIb *wt* cells with single-molecule microscopy. BMPRIb receptor mobility has been greatly boosted after disruption of microtubules (Figure 3g-i) indicating that the confinement of BMPRIb is based not only on receptor localization in membrane microdomains but also on cytoskeletal interactions.

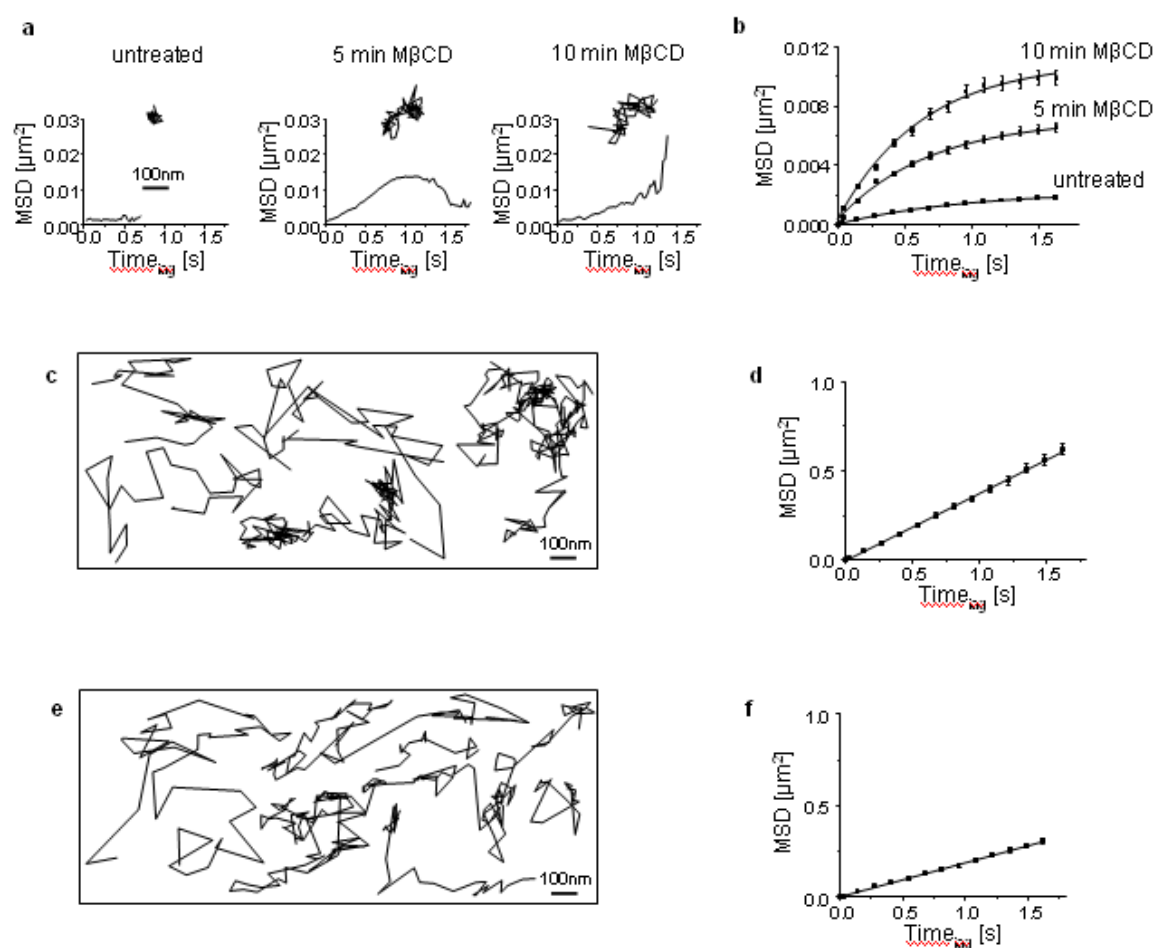


Figure 3a-f. BMPRIb confinement requires both specialized membrane domains and cytoskeletal components.

(a) Short term effects of cholesterol depletion by MβCD on BMPRIb mobility as assessed by single-molecule microscopy. C2C12 cells expressing HA-tagged BMPRIb *wt* (C2C12-BMPRIb *wt*) were starved, QD-labeled and imaged in a time series 0-30 min after application of MβCD. Trajectories and respective MSD graphs of a single representative receptor before, 5 min and 10 min after MβCD application demonstrate gradual mobility increase over time. Scale bar represents 100 nm.

(b) MSD analysis demonstrates an MβCD-induced increase of average BMPRIb mobility of 5 independent experiments starting at 5 min treatment duration.

(c,d) Representative trajectories (c) and MSD analysis (d) of BMPRIb mobility after 60 min MβCD pretreatment show long traces and free diffusion-like motion. Scale bar represents 100 nm.

(e,f) Role of Caveolin1 scaffolds for BMPRIb mobility as assessed by single-molecule microscopy. C2C12-BMPRIb *wt* cells were subjected to transient shRNA-mediated Caveolin1 knockdown. Single-molecule microscopy and analysis of BMPRIb mobility were performed as

described earlier. Representative trajectories (e) and MSD analysis (f) demonstrate increased BMPRIb lateral mobility under Caveolin1 knockdown. Scale bar represents 100 nm.

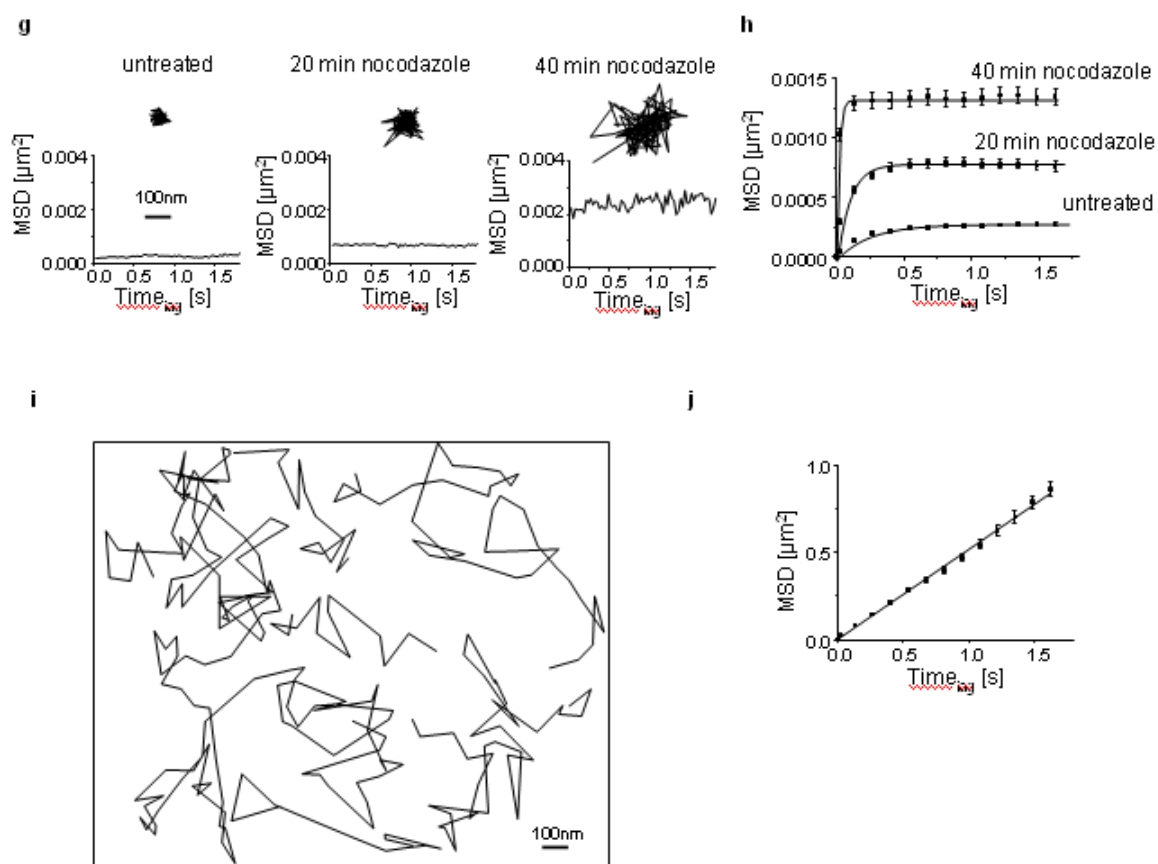


Figure 3g-j BMPRIb confinement requires both specialized membrane domains and cytoskeletal components.

(g-j) Role of cytoskeleton for BMPRIb mobility as assessed by single-molecule microscopy. C2C12-BMPRIb wt cells were treated with nocodazole 0, 10, 20, 40 min (g and h) and for 90 min (i and j) to induce microtubule disruption before QD-labeling and imaging (as described). Representative trajectories (g and i) and MSD analysis (h and j) of BMPRIb mobility under these conditions show increased BMPRIb mobility upon cytoskeletal perturbation. Scale bar represents 100 nm.

2.2.4. Structural elements mediating the confined mobility of BMPRIb

To determine which of domains causes BMPRIb immobility mutagenesis of the extracellular membrane-proximal region (L3 loop) (24), the transmembrane (TM) and intracellular domains were performed (Figure 4a). Thereby some of BMPRIb mutations in the transmembrane region (TM2, TM5 and PKT) were recognized to cause lower co-fractionation of the receptor with the DRM marker Caveolin1 (Figure 4b,c). This indicates that the transmembrane region is essential for the placement of BMPRIb within cholesterol-rich membrane microdomains.

Single-molecule microscopy was utilized to characterize HA-tagged BMPRIb mutants (C2C12-TM2, C2C12-TM5 and C2C12-PKT) respectively expressed in stable C2C12 cell lines. A substitution of three amino acids to alanine in the second turn of the transmembrane α -helix (PKT mutation) resulted in a fivefold increase of the BMPRIb confinement (Figure 4h,i). Lateral mobility of receptors get even greater when four successive point mutations in the same transmembrane region (TM2 mutation) were present (Figure 4d,e). However, the pattern of BMPRIb-TM2 motion remained confined but with the increased to tenfold than of BMPRIb *wt* confinement. Contrasting mobility of great and free diffusion-like motion displayed point mutations in the helix turn closest to the intracellular compartment (TM5 mutation) (Figure 4f,g).

Behavior of receptor mutations was studied as well upon BMP-2 and GDF-5 stimulation. Ligand application did not cause any significant changes to receptor mobility pattern. 5 min after ligand stimulation the confinement size of BMPRIb-TM2 got decreased by 38% but threefold increased in case of BMPRIb-PKT.

Taken together, gathered data clearly show that the transmembrane domain is one of the crucial factors in confining lateral mobility of BMPRIb.

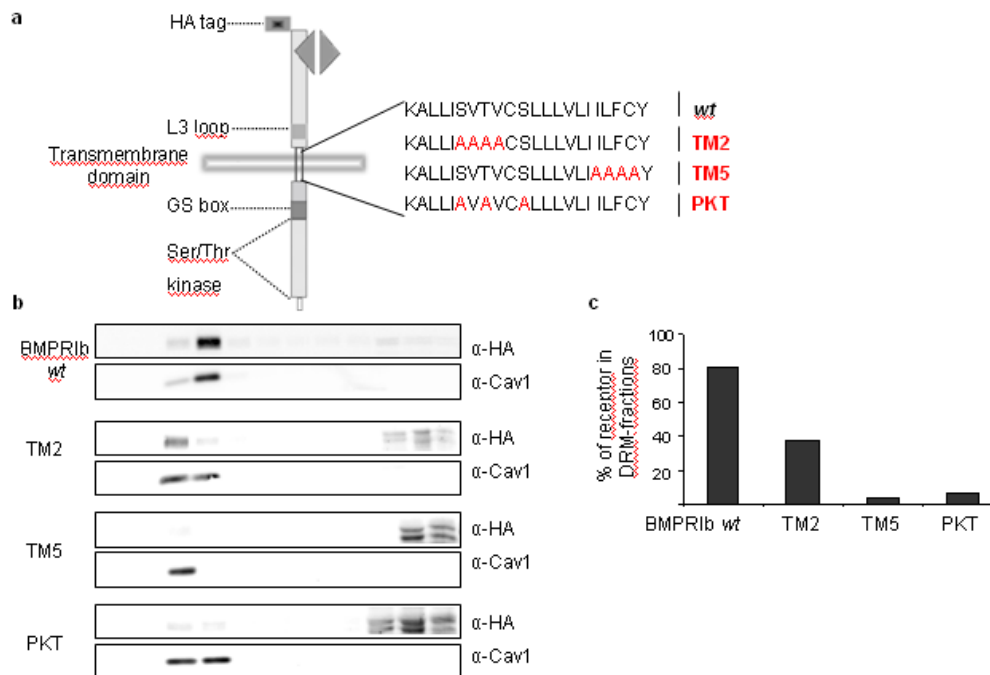


Figure 4a-c. Structural components mediating the confined mobility of BMPRIb.

(a) Mutagenesis approach for identification of structural elements responsible for the immobility of BMPRIb. Point mutations, a poly-alanine scan of the transmembrane domain and intracellular truncations of BMPRIb were generated by targeted mutagenesis. The wild type sequence of transmembrane domain is depicted in black, the mutated amino acids in red.

(b,c) Reduced DRM-association of BMPRIb transmembrane domain (TM) mutants as assessed by co-fractionation of receptor with Caveolin1. C2C12-TM2, -TM5 and -PKT cells were used for sucrose gradient fractionation and fractions were subjected to Western blot

analysis (b). The histogram (c) depicts the percentage of receptor present in DRM-fractions obtained by quantification of the Western blot analysis.

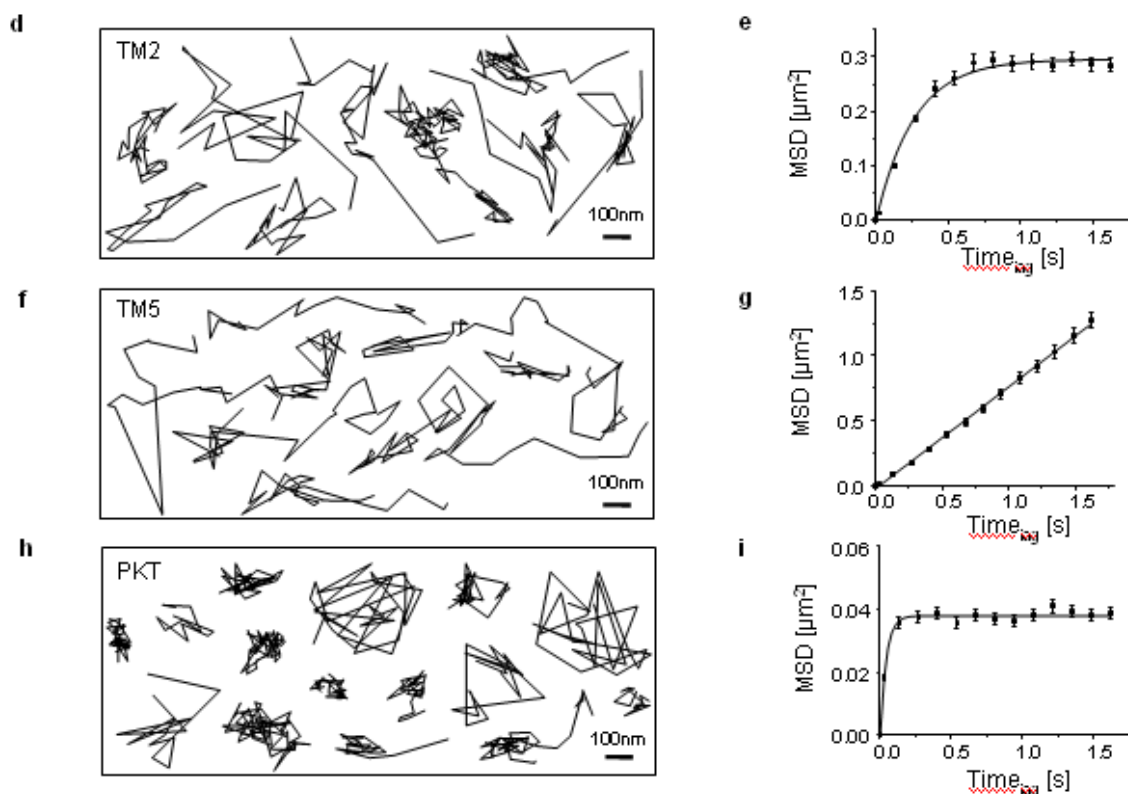


Figure 4d-i. Structural components mediating the confined mobility of BMPRIb. (d-i) Mutations of transmembrane domain increase lateral mobility of BMPRIb. C2C12-TM2, -TM5 and -PKT cells were used for antibody-mediated QD-labeling of receptor and subjected to single-molecule microscopy. Representative trajectories and MSD analysis show a strong increase either in confinement size for the PKT (h) or in lateral mobility for TM2 (d) and TM5 (f) in comparison to BMPRIb *wt*. For MSD analysis data points from five independent experiments were pooled. Scale bar represents 100 nm.

2.2.5. Effects of BMPRIb mobility on SMAD-signaling

BMP receptors transduce signals by triggering SMAD- and non-SMAD-signaling cascades upon ligand stimulation (1). In this study, the influence of BMPRIb increased mobility on signal transduction was investigated.

SMAD-signaling that is activated through BMPRI was examined by Western blot analysis of C-terminal SMAD1/5/8 phosphorylation. Additionally to BMP-2 cells were stimulated with GDF-5 to elicit a clear response of BMPRIb and avoid confusing with endogenous BMPRIa. Ligand-induced activation of SMAD-signaling did not differ in C2C12-TM2, -TM5 and -PKT cells when compared to C2C12-BMPRIb *wt* cells (Figure 5a,b upper panels). Moreover, a BMP-responsive luciferase reporter gene assay displayed no interference with SMAD-dependent transcriptional activation (Figure 5c).

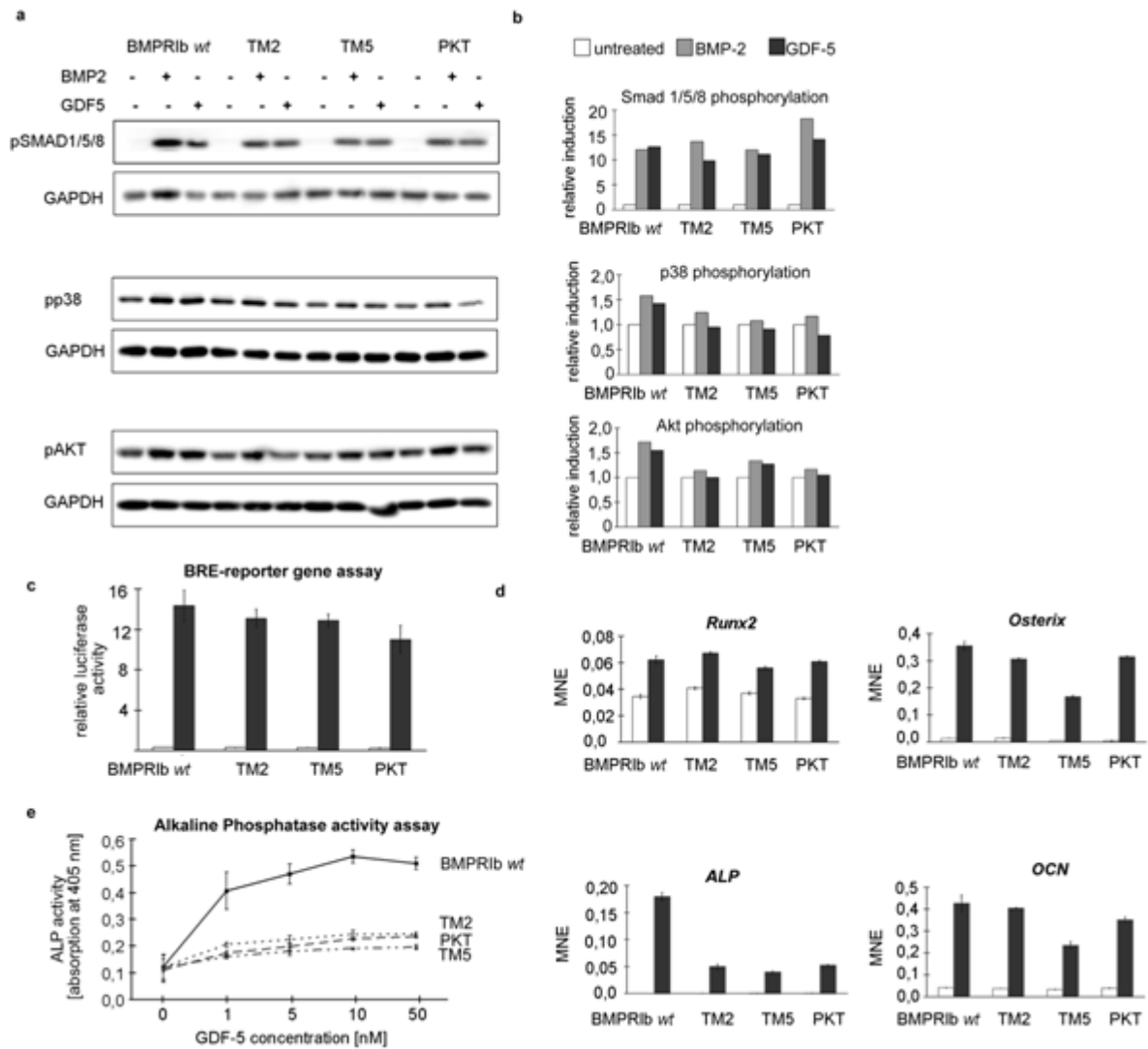


Figure 5. Effects of enhanced BMPRIb mobility on signaling.

(a,b) Western blot analysis of Smad1/5/8, p38 and Akt activation in C2C12-BMPRIb *wt*, -TM2, -TM5 and -PKT cells. Cells were stimulated with BMP-2, GDF-5 or pure PBS for 30-60 min. Cell lysates were subjected to Western blot analysis of respective phosphorylated proteins. GAPDH was used as loading control. Quantification of Western blot (b) depicts relative intensity of phospho-specific signals normalized to respective GAPDH.

(c) Expression analysis of osteoblastic differentiation markers in C2C12-BMPRIb *wt* or mutant cells. C2C12-BMPRIb *wt*, -TM2, -TM5 and -PKT cells were starved, stimulated with GDF-5 for 12 h or 48 h and used for RNA isolation. Quantitative RT-PCR was performed to analyze gene expression of *Runx2*, *ALP*, *Osterix* and *OCN*. Gene expression was normalized to *HPRT* expression and plotted as mean normalized values (MNE).

(d) Analysis of Smad-mediated transcriptional activation by BMP-responsive reporter gene assay. Cells were transfected with BMP-responsive and constitutive active luciferase constructs, starved and stimulated with GDF-5 for 6 h. Luciferase activity was measured in cell lysates. Quantification shows GDF-5-induced luciferase activity normalized to constitutive luciferase activity.

(e) Alkaline phosphatase (ALP) activity assay. C2C12 cells-BMPRIb *wt*, -TM2, -TM5 and -PKT cells were starved and stimulated with various concentrations of GDF-5 for 72 h. ALP production indicative for osteoblastic differentiation was assessed by a colorimetric assay of enzymatic activity of ALP.

2.2.6. Effects of BMPRIb mobility on non-SMAD-signaling

Western blot analysis was used to study the capacity of BMPRIb-TM mutants to activate p38 MAPK and PI3K/Akt pathways. C2C12-TM2, -TM5 and -PKT cells showed no GDF-5 induced activation of p38 and Akt (Figure 5a,b middle and lower panels), and only slight activation upon stimulation with BMP-2 that is elicited through both BMPRIb and endogenous BMPRIa.

The transcriptional effects of non-SMAD-signaling were estimated by expression analysis of BMP target genes *Runx2*, *Osterix (Osx)*, *Osteocalcin (OCN)* and *Alkaline Phosphatase (ALP)*. Expression of the early and mainly Smad-dependent osteoblastic marker *Runx2* was unimpaired upon GDF-5 induction (Figure 5d, upper panel), however *ALP* expression, which necessitates both SMAD- and non-SMAD-signaling and is a later marker of osteogenesis, showed sharp decrease in C2C12-TM2, -TM5 and -PKT cells (Figure 5d, lower panel). Moreover, upon ligand stimulation expression of *Osx* and *OCN* was compromised solely in the C2C12-TM5 cell line (Figure 5d) with TM5 being the mutation of the highest impact on BMPRIb lateral mobility.

The enzymatic activity of ALP was examined in cells expressing particular transmembrane mutants to estimate osteoblastic differentiation. The ALP activity assay revealed GDF-5 induced ALP-production in C2C12-TM2, -TM5 and -PKT cells to be significantly reduced in comparison to C2C12-BMPRIb *wt* (Figure 5e). However, BMP-2 induced ALP-production did not differ in these cells implying no signaling interference between the mutated BMPRIb and endogenous BMPRIa.

Taken together, obtained data have clearly shown that restricted lateral mobility of BMPRIb is essential for efficient non-SMAD-signaling and osteoblastic differentiation of C2C12 cells but not necessary for canonical SMAD-signaling.

2.2.7. Effect of BMPRIb lateral mobility on receptor internalization

The internalization of BMPRIb-TM mutants was measured in the ligand absence and upon ligand stimulation. FACS-based internalization studies (25) were conducted in HEK293T cells transiently expressing equal amounts of HA-tagged BMPRIb *wt* or respective mutants to examine basal endocytosis. The time-dependent decrease of fluorescently stained receptors from the surface was measured by FACS. The internalization of all BMPRIb-TM mutants was observed at similar to BMPRIb *wt* rates (Figure 6a).

Estimation of the internalization was proceeded with the usage of single-molecule microscopy. Individual QD-labeled receptors were tracked before and after ligand stimulation in C2C12 cells stably expressing the respective receptors (Figure 6d-g). Initially, BMP-2 application caused BMPRIb-TM mutants to internalize with varied tempo ($t = 2-15$ min) than BMPRIb *wt*, however after 30 minutes of ligand presence nearly all receptors vanished (Figure 6d-g), hence endocytosis is not impaired under increased lateral mobility of BMPRIb.

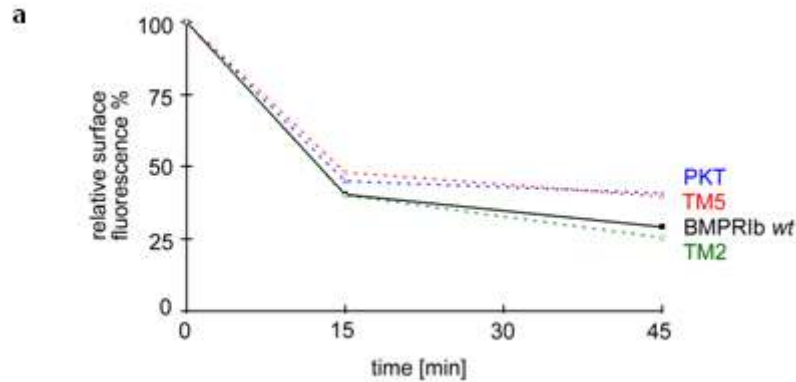


Figure 6a. Increased lateral mobility of receptor does not impair receptor endocytosis. (a) FACS-based analysis of BMPRIb internalization. HA-tagged BMPRIb *wt* or mutant receptors transiently expressed in HEK293T were fluorescently labeled and the decrease of surface fluorescence assessed by FACS-measurements. The line plot depicts the time-dependent decrease of mean fluorescence indicative of receptor internalization.

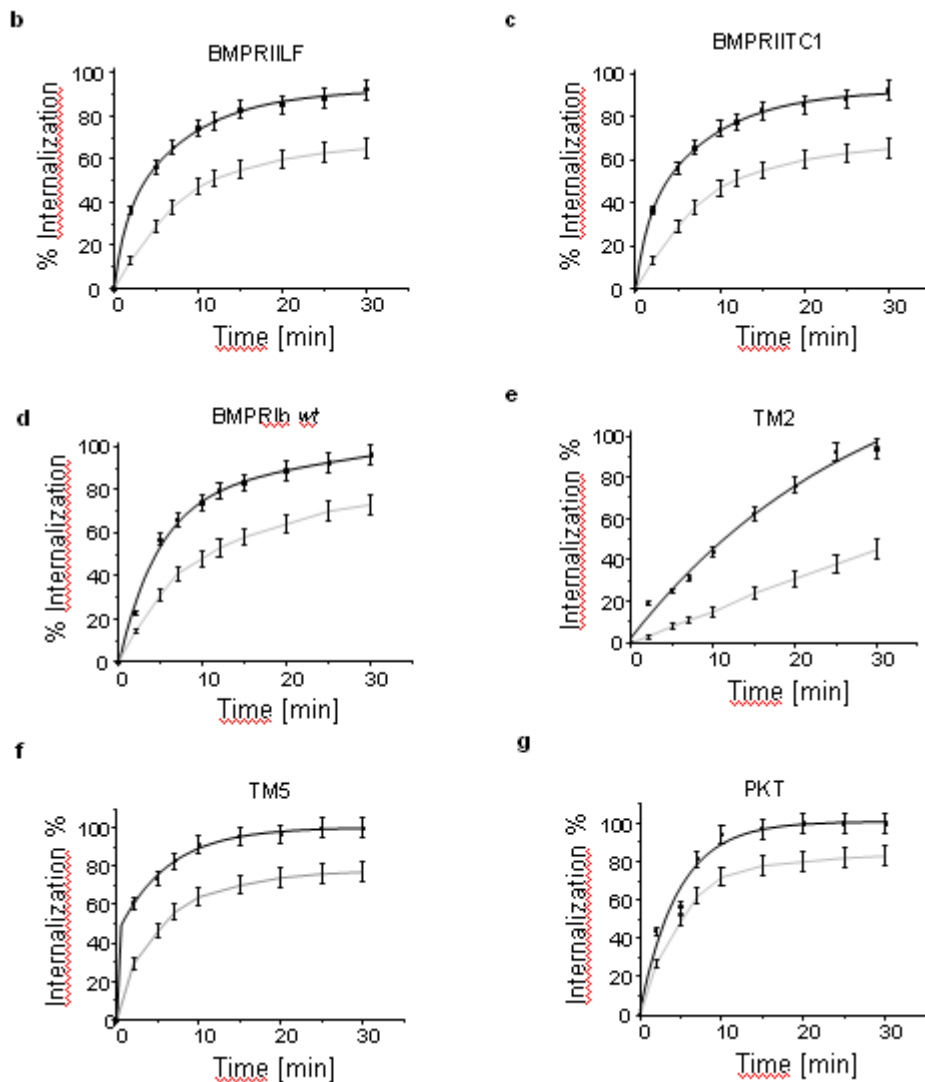


Figure 6b-g. Increased lateral mobility of receptor does not impair receptor endocytosis.

(b-g) Single-molecule analysis of receptor internalization. HA-tagged receptors and receptor mutants stably expressed in C2C12 cells were QD-labeled, ligand stimulated and observed up to 30 min until nearly all receptors internalized. The internalization of following receptor was analysed: BMPRIb *wt* (d); BMPRIb-TM mutants -TM2 (e), -TM5 (f), – PKT (g), BMPRII (b), BMPRII-TC1 (c). Receptor internalization is plotted as % of internalized receptors vs. time without ligand application (grey lines) and after stimulation (black lines). Each internalization profile includes data from five independent experiments.

2.2.8. Effect of BMPRIb lateral mobility on BMPRI/BMPRII hetero-oligomerization

Dual-colour single-molecule microscopy was utilized for analysis of BMPRIb/BMPRII hetero-oligomerization in living cells. C2C12-BMPRIb *wt* or mutant cells were transiently transfected with Myc-tagged BMPRII. Receptors were antibody labeled with quantum dots of two different colors for BMPRI and BMPRII, respectively. Single-molecule microscopy was applied to visualize and analyze co-localization over time. BMPRIb and BMPRII were observed to oscillate between longer and shorter

distances, several times getting close together and again separate, which indicated very dynamic and transient binding between the BMP receptors rather than a stable union (Figure 7a,b). Such behavior of receptors has been recently reported (26).

Analysis of ligand-independent BMPRIb/BMPRII co-localization enabled to define a mean time of receptor unification (“complex lifetime”) to be < 0.4 s for both BMPRIb *wt* and TM-mutants. BMPRIb *wt* and BMPRII complex members were oscillating 3 to 4 times between separating from each other and re-gathering for almost one second. However, ligand application increased the duration of co-localization between BMPRIb *wt* and BMPRII by more than twofold and would recombine on average more than 10 times for a total combination time of at least five seconds, suggesting a stabilization of BMPRI/BMPRII complex upon ligand binding (Figure 7c). In contrast, BMPRIb-TM mutants neither displayed prolonged co-localization with BMPRII upon ligand stimulation nor did they on-average recombine more than twice. Therefore, increased lateral mobility of BMPRIb evidently impairs the stabilization of BMPRI/BMPRII complexes upon ligand binding but does not hinder ligand-independent interaction with BMPRII.

Taken together, single-molecule study revealed a confined lateral mobility of BMPRIa and BMPRIb and two populations, mobile and immobile, of BMPRII. It was presented that BMPRII mobility is reduced upon ligand stimulation, what most probably mirrors a complex formation with BMPRI. Furthermore, the confinement of BMPRIb depends on transmembrane region, necessitates cholesterol-rich membrane regions and cytoskeletal components. Finally, we demonstrate that the confined mobility of BMPRIb is essential for i) ligand-induced stabilization of BMPRIb/BMPRII complex, ii) navigation of non-SMAD responses and iii) subsequent osteoblastic differentiation.

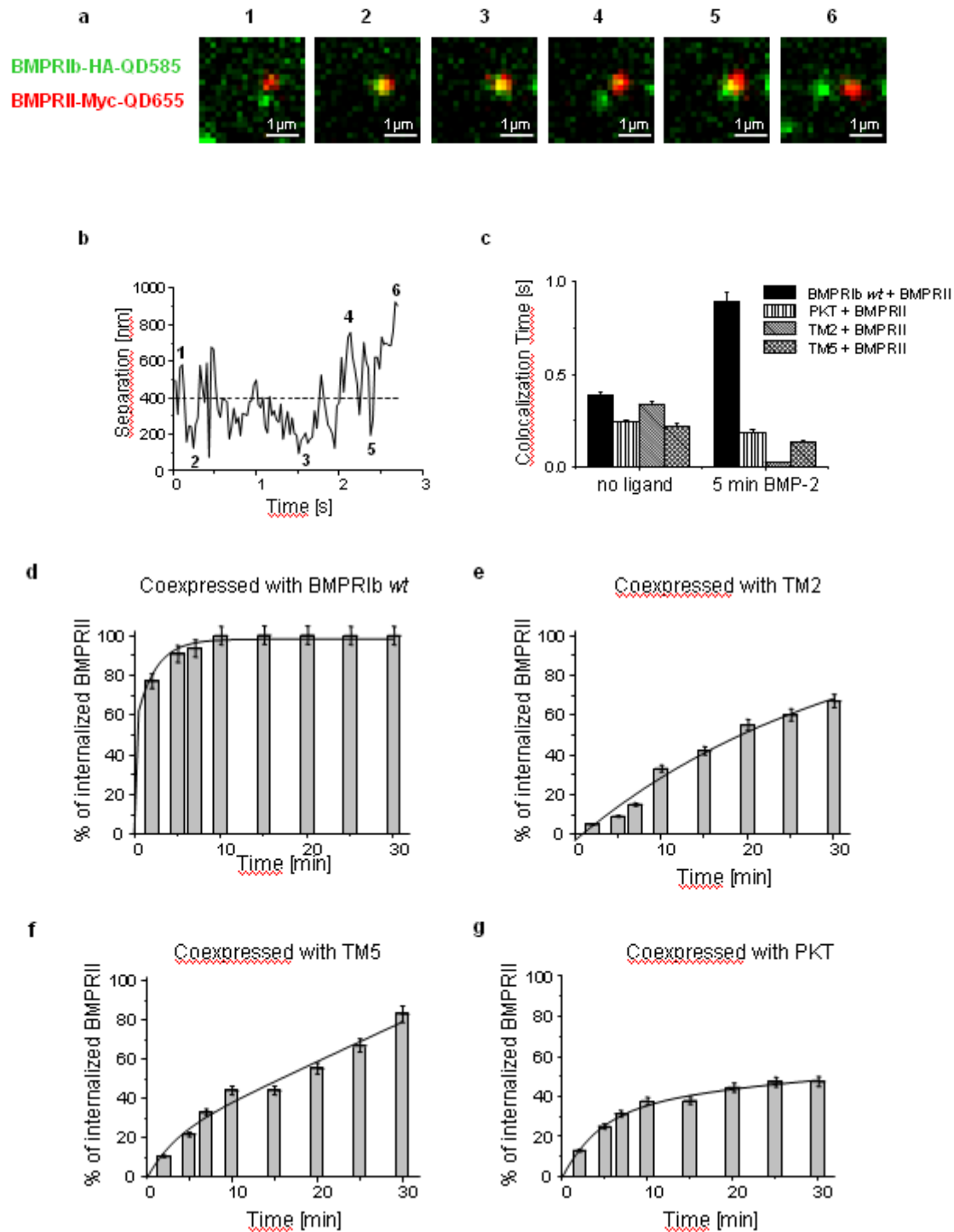


Figure 7. Mobility of BMPRI important for stability of BMPRI/BMPRII hetero-oligomers. (a) Colocalization dynamics of an individual QD585-labeled HA-BMPRIb receptor (green) and an individual QD655-labeled Myc-BMPRIILF receptor (red) before BMP-2 addition on the surface of a C2C12 cell over time. Colocalization is presented by a merged yellow colour. The receptors are shown to come together and dissociate twice. (b) Time-resolved separation distance analysis of the same receptors from a). A threshold distance of 400 nm (dotted line) was applied to determine the minimal colocalization length to reveal the typical behavior that the receptors separate, recombine and to determine the colocalization and separation times.

(c) Time of colocalization between BMPRII and BMPRIb *wt* or particular TM mutants presented before and 5 min after BMP-2 addition. Diagram includes data from five independent experiments and equal number of potential complex pairs. BMP-2 stimulation amplifies the time of colocalization between BMPRII and BMPRIb *wt* by twofold, whereas between BMPRII and BMPRIb-TM mutants no extension in colocalization time was observed . (d-g) Single-molecule quantification of the internalization of BMPRII transiently co-expressed in C2C12 cells with stable expression of HA-BMPRIb *wt* or HA-BMPRIb-TM mutants C2C12 cells. ACP-tagged BMPRII was transiently transfected in stable C2C12 cell lines, labeled with QD655 and studied up to 30 min after BMP-2 addition on single-molecule microscope. Each internalization profile includes data from five independent experiments.

2.2.9. Discussion

BMPs activate non-SMAD pathways including MAPKs (p38, ERK, JNK) (8,10) PI3K/Akt and small GTPases (Rho, Rac, Cdc42) (27) which are crucial for osteoblastic differentiation (28,29) and other cellular responses to BMP (30). However, the factors determining balance between SMAD- and non-SMAD-signaling remain unclear.

In this study the conclusive postulate has been made that receptor lateral mobility navigates through SMAD versus non-SMAD signaling during differentiation. The confinement of BMPRI has been shown as essential factor for activation of p38 and Akt but not of canonical SMAD-signaling.

It was previously reported that disruption of membrane microdomains by cholesterol depletion interferes with p38 activation and osteoblastic differentiation of C2C12 cells (11). Here, we demonstrate that mutations in the transmembrane domain of BMPRIb mimic this chemical treatment in respect to the lateral mobility of receptor and the selective reduction of non-SMAD responses.

We also studied the role of a membrane-proximal, negatively charged extracellular loop (L3 loop) which could target the receptor to microdomains that are enriched in positively charged glycosphingolipids. Only minor effects of the L3 loop mutations on the lateral mobility and no effects on the signaling properties of BMPRIb were noticed. This implies that the transmembrane region is the key mediator of the microdomain association and hence mobility of BMPRIb.

Furthermore, the increased lateral mobility of receptor was shown not to impair constitutive or ligand-induced receptor internalization. It also does not affect formation of heteromeric BMPRI/BMPRII complexes. Thus the BMPRI/BMPRII complex is formed and enough stable to allow the transphosphorylation of BMPRI. This is the reason why enhanced motion does not impair SMAD-signaling. On the other hand, efficient induction of p38 and JNK pathways requires the formation and activation of XIAP-TAB-TAK complex, which was shown to have interactions with both receptors

(8). Possibly, this process necessitates a greater stability of the heteromeric receptor complex which can be observed for BMPRIb *wt* upon ligand binding (as shown by dual colour single-molecule microscopy experiments) but can not be established if lateral mobility of BMPRI is increased e.g. by mutation.

To examine association of the BMPRII immobility with heteromeric complex formation, single-molecule experiments with a BMPRII intracellular truncation mutant (BMPRII-TC1) were conducted. BMPRII-TC1 was previously described as a receptor mutant lacking the ability to build preformed complexes with BMPRI (10). In single-molecule microscopy and mobility analysis this mutant had a homogeneous freely diffusing population with very short immobilization after BMP-2 stimulation. This might imply that the immobility of BMPRII mirrors its hetero-oligomerization with BMPRI.

BMP type I receptors have been shown here to associate with DRMs, whereas BMP type II receptor is found in both DRM- and non-DRM fractions and is shifted to DRM-fractions upon ligand application. This differs from previous results in which neither BMPRIa nor BMPRII were associated with DRMs unless stimulated with a ligand (12). However, that studies were conducted in cells that already underwent chondrocytic differentiation. Possibly, differentiation abolishes the DRM association of receptors to minimize specific signaling pathways that require DRM association. Our data imply that the localization of BMP type I receptor is required for BMP-induced MAPK activation and osteogenic differentiation, thus the DRM-association of receptors might be a general mechanism to modulate the ratio between different responses during differentiation.

Moreover, live cell imaging including single-molecule microscopy and FRAP clearly showed greater mobility for BMPRII that 5-10 min upon ligand stimulation is decreased to the level of BMPRI and gets a confined profile for the whole existing population of receptors. The application of high temporal resolution and surface labeling in biochemical experiments enabled to exclude endocytotic events and to focus on immediate-early processes on the plasma membrane.

2.3. Materials and methods

2.3.1. Constructs, antibodies and reagents

The DNA fragments encoding fluorescent proteins (pEYFP and pECFP (Clontech)) and Acetyl Carrier Proteins (ACP) were PCR amplified and inserted in-frame to the N-terminus of the DNA sequences encoding for the BMP receptors type Ia, Ib, II and II-TC1, including linker regions (17). All fusion constructs were ligated into the pcDNA3 expression vector (Invitrogen) for transient expression in mammalian cells. The expression of BMPRII-TC1 was tested in transfected HEK, Cos-1 cells and C2C12 cells. Antibodies were obtained from following companies (dilution is stated in the brackets): α -HA tag (clone HA-7) (1:1000 for Western blot, 1: 400 for immunofluorescence studies) from Sigma-Aldrich; α -BMPRII (1:500) and α -Caveolin1 (1:1000) from Santa Cruz Biotechnology; α -transferrin receptor (1:1000), α -phosphorylated SMAD1/5/8 (1:1000), α -phosphorylated SAPK/JNK Thr 183/Tyr185, α -phosphorylated Akt Thr308 (1:1000), anti-Myc tag (1:1000 for Western blot, 1: 400 for immunofluorescence studies) and α -GAPDH (1:1000) from Cell Signaling Technology, α -phosphorylated p38 motif PTGPY (1:2000) from Promega.

Methyl- β -cyclodextrin, nocodazole and polyethylenimine (PEI) were purchased from Sigma-Aldrich. Anti-Caveolin1 siRNA and control siRNA were purchased from Santa Cruz Biotechnology and transfected with the siRNA transfection reagent from Santa Cruz Biotechnology.

2.3.2. Cell culture and transfection

C2C12 and HEK293T cells (both purchased from American Type Culture Collection) were cultivated in Dulbecco's modified Eagle's culture medium (Biochrom, Germany) supplemented with 10% v/v fetal bovine serum (Biochrom), 2 mM L-Glutamin (PAA), 100 U/ml Penicillin (PAA) and 100 mg/ml Streptomycin (PAA) at 37°C/10% CO₂. For transient transfection LipofectamineTM 2000 (Invitrogen) was used according to manufacturer's instructions. Cells were seeded out on plates (Sarstedt) or glass coverslips (24mm, class 1, Hartenstein GmbH) and used for assays or imaging 20 h to 48 h post transfection. For transient transfection of HEK293T cells polyethylenimine (PEI) (Sigma-Aldrich)) or Effectene (Qiagen, Hilden, Germany) was used as described earlier. Stable C2C12 cell lines were established by retroviral transduction of Gateway^R-based

(Invitrogen) HA-tagged BMPRIb *wt* or respective mutant constructs followed by 500 µg/ml Hygromycin B selection and FACS sorting.

2.3.3. Separation of detergent-resistant membrane microdomains (DRMs)

Isolation of DRMs was performed as described (11). In short, C2C12 cells were lysed with buffer containing 20 mM (3-[(3-cholamidopropyl)-dimethylammonio]-1-propanesulfonate) (CHAPS), 25 mM Tris-HCl pH 7.4, 150 mM NaCl, 3 mM EDTA, protease and phosphatase inhibitors in according concentrations for 30 min at 4° C, homogenized with a Potter apparatus and cleared of cell debris by centrifugation. The lysate was adjusted to a concentration of 40% OptiPrepTM (Axis-Shield, Scotland) and layered with a discontinuous OptiPrep gradient (30%, 5%). Following ultracentrifugation (20 h, 39000 rpm, 4°C, SW40Ti Beckman rotor) the gradient was fractionated by pipetting 10 - 11 fractions of equal volume from the top, which were denaturated and analysed by SDS-PAGE and Western blot.

2.3.4. Cell surface biotinylation

Cell surface biotinylation was performed by incubating adherent cells with 0,5 mg/ml EZ-LinkTM Sulfo-NHS-LC-Biotin in PBS (Pierce) for 1h at 4°C. Subsequently cells were washed for 10 min with 50 mM Tris pH 8,0 to quench Biotin and processed for DRM separation as described above. For precipitation of biotinylated proteins after sucrose gradient ultracentrifugation fractions were treated as described (34). In short, fractions were adjusted to equal sucrose concentration and 1% TritonX. Next they were incubated at 37° C for 15 min and cleared of insoluble particles by centrifugation. Then biotinylated proteins were isolated by incubation and precipitation with Streptavidin-SepharoseTM beads (GE Healthcare), denaturated and subjected to Western blot analysis.

2.3.5. Dual luciferase reporter gene assay

C2C12 cells (5×10^3 per well of 96-well plate) were transfected with 40 ng BMP response element (BRE)-fused *firefly* luciferase construct (p(BRE)₄-luc) (32) and 30 ng *Renilla* luciferase construct (pRLTK). 20 h post transfection cells were serum starved and subsequently stimulated with 1-10 nM BMP-2 or GDF-5. Cell lysis and luciferase measurements were carried out according to manufacturer's instructions (Dual-Luciferase Reporter Assay System; Promega). Luciferase activity was measured by

Mithras plate luminometer (Berthold Technologies, Germany). All measurements were conducted in triplicates.

2.3.6. *Alkaline phosphatase activity assay*

C2C12 cells ($1,5 \times 10^4$ per well of 96-well plate) were grown for 20 h in normal growth medium, starved for 2 h in serum-reduced medium (2% FCS) and treated for 72 h with various concentrations of BMP-2 or GDF-5 (1-20 nM) in serum-reduced medium. Cells were lysed and alkaline phosphatase activity was determined as absorption at 405 nm as described (33Katagiri, Yamaguchi et al. 1994).

2.3.7. *Western Blot analysis of SMAD- and non-SMAD signaling*

C2C12 cells ($1,5 \times 10^5$ per well of 6-well plate) were grown for 24 h in normal growth medium, starved in serum-reduced medium and stimulated with 1-10 nM BMP-2 or GDF-5 for 15 min – 60 min. Stimulation was stopped by cell lysis. As a control for each time point stimulation with pure PBS occurred for the same duration as ligand stimulated samples. After denaturation samples were analysed by SDS-PAGE and Western blotting. Western blots were probed with phospho-specific antibodies to detect activation of various players of SMAD- and non-SMAD pathways.

2.3.8. *Quantitative Reverse Transcription – PCR*

C2C12 cells (3×10^5 per well of 6-well plate) were grown for 24 h in normal growth medium, starved for 2-5 h in serum-reduced medium and stimulated for 12 h, 24 h or 48 h with 10 nM BMP-2 or GDF-5. Total RNA was extracted using NucleoSpin^R RNA II Kit (Macherey-Nagel, Dueren, Germany) according to manufacturer's instructions. cDNA was synthesized from 1 µg RNA and used in SYBR Green quantitative real-time PCR in 1:8 dilutions. The amount of following transcripts: *Runx2*, *Osterix*, *Alkaline Phosphatae* (*ALP*) and *Osteocalcin* (*OCN*), was determined relative to the housekeeping gene hypoxanthine-phosphoribosyltransferase (*HPRT*). For each gene real-time PCR reactions from BMPRIb *wt* versus mutant receptor expressing samples under the respective stimulated and unstimulated conditions were performed. All measurements were done in triplicates (StepOnePlus instrument from Applied Biosystems) and C(T) values were determined using StepOne Software v2.2. Mean normalized expression (MNE) and the corresponding standard error (SE_MNE) were calculated according to (Simon, 2003 #30).

2.3.9. Fluorescence Tagging - Quantum Dot Labeling of ACP

Labeling was performed by incubating the cells on the cover slips for 15-20 min at 37°C in DMEM (270 µl) with 1% Bovine Serum Albumin (BSA, Sigma-Aldrich); 1.5 µM 6xHis-PPTase and 0.3 nM CdSe/ZnS Quantum Dot – CoA molecules prepared with the 655 QDot Antibody Conjugation Kit (Molecular Probes, Invitrogen). Before measurements samples were washed three times with 300 µl DMEM. Experiments were conducted on cells in 250 µl DMEM (17).

2.3.10. Quantum Dot Antibody Labelling of HA- and Myc- tagged Receptors

The primary α -HA (clone H7, Sigma, Taufkirchen, Germany) or α -Myc (Cell Signaling) antibodies 0,6 µl and 2 µl at 0.1 mg/ml were incubated on the transfected cells with in 100 µl growing media at 37° C for 10 minutes then washed three times with 300 µl DMEM containing 10% FCS. To avoid non-specific binding, cells were incubated with full media plus 5% goat serum (Sigma-Aldrich) 5 min at 37° C, then again triple washing step occurred. Quantum Dots (QD-655 and QD-585) conjugated with specific secondary antibodies to α -mouse and α -rabbit. (Invitrogen, USA), 0.35 µl in 200 µl growing media, were added to the cells following the primary antibody addition procedure for 25-30 minutes at room temperature and was washed three to five times with Phenol Red-free DMEM.

2.3.11. Cholesterol extraction by M β CD treatment

Cholesterol depletion was done by incubation the cells in DMEM supplemented for a total concentration of 5 mM methyl- β -cyclodextrin (M β CD, Fluka) (or methyl- β -cyclodextrin, M β CD, Sigma-Aldrich Chemie, Steinheim, Germany) either in an incubator for 1 h at 37°C with 10 % CO₂ (95% humidity) with subsequent washing with full media or with application directly on the microscope. Data after these procedures were recorded over a period of one to two hours.

2.3.12. Microtubules Destabilization

Polimerization of microtubules was interfered by: incubating the cells for 1 h at 37°C with 10 % CO₂ (95% humidity) in DMEM supplemented with 5 µM nocodazole that was kept another 30 min on the cells during staining and imaging (i.e. 1,5h in total.); or by

direct addition of 5 μ M nocodazole to the imaged sample. Time points measured after the nocodazole treatment: 0, 2, 5, 10, 15, 20, 25, 30, 35, 40, 45, 50, 55 and 60 minutes.

2.3.13. BMP addition

In most cases, BMP-2 (Sigma-Aldrich, USA) was used as a cytokine ligand for BMPRI and BMPRII receptors, with final concentration of 0.5 nM, 1 nM, 2 nM, 20 nM, and 40 nM. The ligand addition occurred either through an injection system (InjectMan, Eppendorf, Germany) or perfusion system (either home-built or Manufacturer, Country). In some cases for comparison, after recording the data on unstimulated cells 2 μ l of 20 μ M BMP-2 (provided as a kind gift from Prof. Walter Sebald, Physiological Chemistry, Würzburg, Germany) solution were added directly to the media or buffer solution of the sample to get the final reported concentration of the ligand. After allowing the samples to diffuse throughout the sample, recording was continued.

2.3.14. Confocal microscopy

HEK293T, COS-1 or C2C12 cells were grown to 50% confluence on 24 mm glass cover slips, transiently transfected, and incubated in complete DMEM medium for 24 h. After this, cells were perfused with PBS. Cells were analyzed before or after treatment with 20 nM BMP-2. All live cell imaging was performed at room temperature. The fluorescence images were recorded on a Leica SP5 confocal microscope with a 63 \times NA 1.4 objective. The fluorescence emission resulted from excitation with 458 (for CFP) and 514 (for YFP) nm laser lines from an argon ion laser (Coherent Inova, I-308) from the modified Zeiss LSM-410 or Lasos (DMI 600B, Germany) with the Leica SP5 LSM confocal with internal spectral parameter settings of 458 for CFP and 514 nm for YFP. The fluorescence was detected with either optical filter sets from the microscope manufacturer using a 475–495 band pass filter for CFP and a 530–585 band pass filter for YFP or with a 490–500 nm spectral band width setting for CFP and a 520–590 nm spectral band width setting for YFP on the Leica SP5. For imaging of quantum dots on the confocal microscope either a D655/40 emission filter (Chroma, USA) in the Zeiss LSM-410 or a spectral window of 635-675 in the Leica SP5 was used.

2.3.15. FRET microscopy measurements

In this study, a fluorescence microscope was used to perform FRET measurements (resf-). We quantified the FRET signal by calculating excess acceptor

emission using FRET ratios from defined regions of interest in, for example, the cell membrane. The setup for fluorescence resonance energy transfer between the cyan and yellow fluorescent proteins comprises an inverted microscope (Axiovert 200, Carl Zeiss) equipped with a high numerical aperture objective (Plan Apochromat 100×, 1.4 NA, Carl Zeiss). Samples were excited with wide-field light from a computer-driven monochromator Xenon lamp source (Polychrome IV, Till Photonics) at 436 ± 5 nm (CFP) and 480 ± 5 nm (YFP) that was connected to the microscope with an optical light guide and optical focusing system (Till Photonics) with the excitation light reflected by a dichroic beamsplitter (for CFP and FRET measurements, DCLP 460 or for YFP measurements, DCLP 490, Chroma) into the microscope objective. The fluorescence images and recordings were made by detection from a CCD camera (Coolsnap HQ, Photometrics) with the image on the CCD camera split spectrally in half and re-imaged on the CCD with a relay system with a dichroic beam splitter at 505 nm and two filtered split images bandpass filtered again with the a 480 ± 20 nm for CFP emission and the other at 535 ± 15 nm for YFP emission (Dual View, Optical Insights). FRET (including the individual CFP and YFP) signals and images were acquired every 1 s.

FRET is calculated as the ratio of the corrected YFP and CFP emission intensities at 535 ± 15 nm (I_{YFP}) and 480 ± 20 nm ($I_{CFP}(436)$): $I_{YFP}/I_{CFP}(436)$ upon excitation of CFP at 436 ± 5 nm (beam splitter DCLP 460 nm). The YFP (acceptor) direct excitation factor was determined with YFP transfected cells only. The YFP fluorescence was recorded first with 436 ± 5 nm excitation ($F_{Y,436}$). Next the YFP emission was recorded with 480 nm excitation ($F_{Y,480}$). The direct excitation crosstalk was calculated by $F_{Y,436}/F_{Y,480}$ and was equal to 0.06 ± 0.01 . The YFP only cells did not show any emission intensity in the CFP emission channel with 436 ± 5 nm excitation. The bleed-through or spillover crosstalk of CFP (donor) into the 535-nm channel was determined first from cells expressing CFP with 436 ± 5 nm excitation (and also of pure recombinant CFP) only showed that the 535 nm channel had 56% of the intensity of the 480 nm channel. The FRET ratio calculation was performed in the following steps to ensure correct subtractions of signals for FRET(ref-): (1) we identify and subtract the spillover of the CFP in the YFP channel to determine the pure YFP component due to FRET and direct excitation: $YFP_{sum} = I_{YFP}(436 \text{ nm}) - I_{CFP}(436 \text{ nm}) \times 0.56$, (2) we identify and subtract the direct excitation component to determine the YFP signal due to FRET: YFP_{FRET} (or I_{YFP}) = $YFP_{sum} - 0.06 \times YFP(480 \text{ nm})$, and (3) the FRET ratio was then calculated by the formula: $FRET_{ratio} = I_{YFP}/I_{CFP}(436 \text{ nm})$.

FRET data were acquired for a long time periods before ligand addition to make sure that both the cyan site and yellow fluorescent protein signals were stable and were not photobleaching. Otherwise, the measurements were discontinued and not included in these results.

To study agonist-induced changes in FRET, cells were placed in FRET-buffer or in DMEM (0.5% FCS) and BMP-4 (20 nM) was applied. As a negative control on the cell the FRET-buffer or DMEM (0.5% FCS) was applied to show that the FRET change was induced by BMP-4 addition but not by buffer or media. The imaging data were analyzed with Origin (Microcal) software. ImageJ and MetaMorph 5.0 (Universal Imaging) were also used in some cases. All live cell imaging was performed at room temperature.

We proved FRET by photobleaching the acceptor and then observed the donor dequenching (donor signal increase). The calculation of relative CFP:YFP concentrations for the intermolecular FRET were corrected by dividing by the brightness of the individual, initial CFP ($I_{\text{CFP}}(436)$) and YFP ($I_{\text{YFP, corr}}$) intensities: $I_{\text{CFP}}(436)/(t_{\text{CFP}} \epsilon_{\text{CFP},436} \varphi_{\text{CFP}})$ and $I_{\text{YFP, corr}}/(t_{\text{YFP}} \epsilon_{\text{YFP},436} \varphi_{\text{YFP}})$ where t_{CFP} and t_{YFP} are the optical transmissions for CFP and YFP in the respective CFP (0.35) and YFP (0.60) detection channels, $\epsilon_{\text{CFP},436}$ and $\epsilon_{\text{YFP},436}$ are the molar extinction coefficients of CFP ($28,000 \text{ M}^{-1} \text{ cm}^{-1}$) and YFP ($7,000 \text{ M}^{-1} \text{ cm}^{-1}$) at $436 \pm 5 \text{ nm}$ excitation, respectively, and φ_{CFP} and φ_{YFP} are the fluorescence quantum yields of CFP (0.36) and YFP (0.76) (refs-).

2.3.16. Single-molecule microscopy

Our primary experimental design is a custom arrangement for wide-field single-molecule imaging. Different versions have been described previously in detail (refs.). Briefly, cells adherent to glass slides were mounted onto the microscope and kept in phenol red free DMEM (Invitrogen) at 37°C . The single-molecule images were obtained with a Zeiss Axiovert 200 microscope (Carl Zeiss, Jena, Germany) with a $100\times$ oil-immersion objective (Plan Apochromat Oil, $\text{NA}=1.4$, Zeiss, Oberkochen, Germany) and with an objective heater with temperature controller (Bioptecs, Colorado USA and Visitron, Germany) to keep the cells at 37°C . The samples were illuminated for 3 to 10 ms by an Ar^+ -laser (Coherent, Dieburg, Germany, and Santa Clara, CA USA) at a wavelength of 514 nm and by the 473 nm laser line of a diode laser (MB-473-100, CNI Laser, China). The control of pulse length was performed by focusing into either a fast mechanical shutter (nm laser, CA, USA) or into an AOTF (Acousto Optic Time

Frequency Modulator, AA Optic, France). A synchronization signal of the camera exposure was directed as a trigger to either a computer DACA board (National Instruments, Munich Germany or Austin TX, USA) or to a computer-programmable pulse generator (Hameg, Germany) to steer the pulse length. The illumination intensity was set from 0.35 to 0.9 kW/cm² ±0.2 kW/cm² (or 3 to 5 kW/cm² ±0.2 kW/cm² for fluorophores in the control experiments listed below) either via setting of the throughput voltage of the AOTF or from placement of neutral density filters in the beampath to proper attenuation. With appropriate filter combination (DCLP525, DCLP555, DCLP645, HQ605/75, D655/40 or HQ690/90 Chroma Technology, Rockingham, VT, USA; or OG550-3, Schott, Mainz, Germany) along with a peltier-cooled slow-scan CCD camera system (1300B, Princeton Instruments, Trenton, NJ, USA) or of the peltier-cooled EMCCD-camera system (CascadeII 512B, Roper Scientific, USA), single-molecules of either tetramethyl rhodamine (TRITC) (from Molecular Probes, Netherlands) with a total detection efficiency of 12 % or quantum dots with emission at 655 nm (QD655) (Invitrogen, USA) with a total detection efficiency of 14% could be detected. For the observation of the localization and mobility of the anchored fluorophores the focus was set to the apical membrane of the cell with a depth of focus of ~1 μm. The density of fluorescent proteins on the plasma membrane of transfected cells was < 1 μm⁻² to permit imaging and tracking of individual fluorophores on average except for the cases when the membrane receptor proteins aggregated through natural cell signaling processes.

2.3.17. Single molecule and total internal reflection (TIRF) microscopy

The cells were illuminated at 405 nm by a diode laser (Cube 405 nm – 50 mW, Coherent Laser, USA/Germany) for either CFP or QDots or a 488 nm laser for YFP or QDots synchronized with a CCD camera (Cascade 512B, Photometrics, USA), an acousto-optic tunable filter (AOTF), and an objective type total internal reflection microscope (AM TIRF – DMI 6000, Leica Microsystems GmbH, Wetzlar, Germany) with a 100x objective (PlanApo 100x NA 1.45, Leica, Wetzlar, Germany) controlled with LASAF software (Metamorph provided exact timing of the illumination time, intensity and wavelength. Single molecules were visualized using an objective type total internal reflection microscope (AM TIRF – DMI 6000, Leica Microsystems GmbH, Wetzlar, Germany) with a 100x objective (PlanApo 100x NA 1.45, Leica, Wetzlar, Germany). Fluorescence signals from TMR were monitored through a dichroic mirror in

combination with a band-pass (for 568nm, Chroma Technologies) by a CCD camera at 30-msec intervals (Cascade 512B, Photometrics, USA). Typically 500 readouts of a small region of the full array (typically 100x100 pixels, i.e. 16 x 16 μm^2 in the image plane, of a total 512 x 512 pixels) of the CCD chip was acquired to the PC.

2.3.18. Fluorescence Recovery After Photobleaching (FRAP)

All live cell imaging was performed at 37°C. The fluorescence images were recorded on either a modified confocal microscope (LSM-410, Carl Zeiss, Göttingen, Germany and LSM Tech, Stewardstown, PA, USA) with a 100x NA 1.3 objective (Carl Zeiss, Goettingen, Germany) or a Leica SP5 confocal microscope (Leica, Mannheim, Germany) with a 63x NA 1.4 objective (Leica, Wetzlar, Germany). The fluorescence emission resulted from excitation with a 514 nm laser LSM-410 confocal microscope (Zeiss, Jena, Germany) or with the Leica SP5 LSM (Leica, Mannheim & Wetzlar, Germany) confocal microscope. The fluorescence was detected with either optical filter sets from the microscope manufacturer using a LP530 in the modified LSM-410 confocal microscope (Zeiss, Göttingen, Germany) or with the Leica SP5 confocal microscope (Leica, Mannheim, Germany) a 530-610 nm spectral band width setting for the YFP. For FRAP on the LSM-410 confocal microscope, the 514 nm laser was synchronized with custom electronics (Lab View, National Instruments, Austin, TX, USA) and an acousto-optic modulator (AOM, Isomet, USA) for the 514 nm line to allow light intensity to be adjusted on a pixel-by-pixel basis for wither imaging or photobleaching. The green excitation light was sent through focusing optics and the AOM and then directly into the microscope.

For FRAP experiments, all scans were 128 x 128 pixels representing a 64 x 64 μm area. Prebleach images were first acquired to analyze prebleach intensity. Each image was scanned within 200 ms, and four images per second were acquired. For the bleach, the scanner mirror range was reduced by a factor of 16 in order to zoom in to a 4 x 4 μm area on the surface of a cell and a simultaneous trigger was sent from the LSM to a Labview (National Instruments, USA) program which allowed the user to define the appropriate timing (delay and duration of the bleach pulse) by precisely controlling the voltage signals to the AOM to increase laser intensity for the time of the bleach scan, and then returned back to normal scanning intensity when bleach scan was finished. Bleaching occurs in 200 ms, and the first image was taken 200ms after the bleach was finished. Then 15 images were taken every 250 ms, follwed by 20 images every 500ms,

10 images every 1 seconds, 10 images every 2 seconds and finally 70 images every 4 seconds for faster diffusing samples, or 15 images were taken every 250 ms, followed by 20 images every 500 ms, 10 images every 2 seconds, 10 images every 4 seconds and finally 70 images every 8 seconds for slower diffusing samples.

2.3.19. FRAP Analysis

The images were analyzed with the use of Image J (NIH, USA) and the data was exported to Origin (Origin Labs, USA) for analysis. Average fluorescence intensities within Regions of Interest (ROI) in the bleached regions were analyzed for each detection channel to obtain the recovery data. Corrections were made for photobleaching during scanning by monitoring neighboring cells and analyzing their signals. Mobile fractions were calculated and the recovery was fit to the equation: $I = A1 - A2 \cdot \exp(-k \cdot t)$ where I is the average intensity, k is the rate of the exponential recovery, t is the time, A1 is the full recovery value and A2 is the value of the drop in intensity after the bleach. Two component recovery analysis was also applied to data and fit to the equation: $I = A1 - A2 \cdot \exp(-k1 \cdot t) - A3 \cdot \exp(-k2 \cdot t)$. Percentage of immobile fraction is calculated by comparing pre-bleach intensity with recovered intensities.

2.3.20. Data analysis

according to the point 1.3.7.

2.3.21. Mobility analysis

according to the point 1.3.8.

2.4. References

1. Sieber, C., J. Kopf, et al. (2009). "Recent advances in BMP receptor signaling." *Cytokine Growth Factor Rev* 20(5-6): 343-55.
2. Kishigami, S. and Y. Mishina (2005). "BMP signaling and early embryonic patterning." *Cytokine Growth Factor Rev* 16(3): 265-78.
3. Zhao, G. Q. (2003). "Consequences of knocking out BMP signaling in the mouse." *Genesis* 35(1): 43-56.
4. Andriopoulos, B., Jr., E. Corradini, et al. (2009). "BMP6 is a key endogenous regulator of hepcidin expression and iron metabolism." *Nat Genet* 41(4): 482-7.
5. David, L., C. Mallet, et al. (2008). "Bone morphogenetic protein-9 is a circulating vascular quiescence factor." *Circ Res* 102(8): 914-22.
6. Vukicevic, S. and L. Grgurevic (2009). "BMP-6 and mesenchymal stem cell differentiation." *Cytokine Growth Factor Rev* 20(5-6): 441-8.
7. Miyazono, K., Y. Kamiya, et al. (2009). "Bone morphogenetic protein receptors and signal transduction." *J Biochem* 147(1): 35-51.
8. Yamaguchi, K., S. Nagai, et al. (1999). "XIAP, a cellular member of the inhibitor of apoptosis protein family, links the receptors to TAB1-TAK1 in the BMP signaling pathway." *Embo J* 18(1): 179-87.
9. Gilboa, L., A. Nohe, et al. (2000). "Bone morphogenetic protein receptor complexes on the surface of live cells: a new oligomerization mode for serine/threonine kinase receptors." *Mol Biol Cell* 11(3): 1023-35.
10. Nohe, A., S. Hassel, et al. (2002). "The mode of bone morphogenetic protein (BMP) receptor oligomerization determines different BMP-2 signaling pathways." *J Biol Chem* 277(7): 5330-8.
11. Hartung, A., K. Bitton-Worms, et al. (2006). "Different routes of bone morphogenic protein (BMP) receptor endocytosis influence BMP signaling." *Mol Cell Biol* 26(20): 7791-805.
12. Zhou, Z., J. Xie, et al. (2010). "Neogenin regulation of BMP-induced canonical Smad signaling and endochondral bone formation." *Dev Cell* 19(1): 90-102.
13. Nickel, J., A. Kotzsch, et al. (2005). "A single residue of GDF-5 defines binding specificity to BMP receptor IB." *J Mol Biol* 349(5): 933-47.
14. Sako, Y., S. Minoghchi, et al. (2000). "Single-molecule imaging of EGFR signalling on the surface of living cells." *Nat Cell Biol* 2(3): 168-72.

15. Parton, R. G. and J. F. Hancock (2004). "Lipid rafts and plasma membrane microorganization: insights from Ras." *Trends Cell Biol* 14(3): 141-7.
16. Ma, X., Q. Wang, et al. (2007). "Lateral diffusion of TGF-beta type I receptor studied by single-molecule imaging." *Biochem Biophys Res Commun*.
17. Zelman-Femiak, M., K. Wang, et al. (2010). "Covalent quantum dot receptor linkage via the acyl carrier protein for single-molecule tracking, internalization, and trafficking studies." *Biotechniques* 49(2): 574-9.
18. Lommerse, P. H., G. A. Blab, et al. (2004). "Single-molecule imaging of the H-ras membrane-anchor reveals domains in the cytoplasmic leaflet of the cell membrane." *Biophys J* 86(1 Pt 1): 609-16.
19. Bragdon, B., O. Moseychuk, et al. (2010). "Bone Morphogenetic Proteins: A critical review." *Cell Signal*.
20. Villalba, M., K. Bi, et al. (2001). "Vav1/Rac-dependent actin cytoskeleton reorganization is required for lipid raft clustering in T cells." *J Cell Biol* 155(3): 331-8.
21. Brdickova, N., T. Brdicka, et al. (2001). "Interaction between two adapter proteins, PAG and EBP50: a possible link between membrane rafts and actin cytoskeleton." *FEBS Lett* 507(2): 133-6.
22. Head, B. P., H. H. Patel, et al. (2006). "Microtubules and actin microfilaments regulate lipid raft/caveolae localization of adenylyl cyclase signaling components." *J Biol Chem* 281(36): 26391-9.
23. de Keijzer, S., J. Galloway, et al. "Disrupting microtubule network immobilizes amoeboid chemotactic receptor in the plasma membrane." *Biochim Biophys Acta* 1808(6): 1701-8.
24. Allendorph, G. P., W. W. Vale, et al. (2006). "Structure of the ternary signaling complex of a TGF-beta superfamily member." *Proc Natl Acad Sci U S A* 103(20): 7643-8.
25. Horbelt, D., G. Guo, et al. (2010). "Quantitative analysis of TGFBR2 mutations in Marfan-syndrome-related disorders suggests a correlation between phenotypic severity and Smad signaling activity." *J Cell Sci* 123(Pt 24): 4340-50.
26. Marom, B., E. Heining, et al. "Formation of Stable Homomeric and Transient Heteromeric Bone Morphogenetic Protein (BMP) Receptor Complexes Regulates Smad Protein Signaling." *J Biol Chem* 286(22): 19287-96.
27. Gamell, C., N. Osses, et al. (2008). "BMP2 induction of actin cytoskeleton reorganization and cell migration requires PI3-kinase and Cdc42 activity." *J Cell Sci* 121(Pt 23): 3960-70.
28. Gallea, S., F. Lallemand, et al. (2001). "Activation of mitogen-activated protein kinase cascades is involved in regulation of bone morphogenetic protein-2-induced osteoblast differentiation in pluripotent C2C12 cells." *Bone* 28(5): 491-8.

29. Guicheux, J., J. Lemonnier, et al. (2003). "Activation of p38 mitogen-activated protein kinase and c-Jun-NH2-terminal kinase by BMP-2 and their implication in the stimulation of osteoblastic cell differentiation." *J Bone Miner Res* 18(11): 2060-8.
30. Gamell, C., A. G. Susperregui, et al. (2011). "The p38/MK2/Hsp25 pathway is required for BMP-2-induced cell migration." *PLoS One* 6(1): e16477.
31. Zuo, W. and Y. G. Chen (2009). "Specific activation of mitogen-activated protein kinase by transforming growth factor-beta receptors in lipid rafts is required for epithelial cell plasticity." *Mol Biol Cell* 20(3): 1020-9.
32. Korchynskiy, O. and P. ten Dijke (2002). "Identification and functional characterization of distinct critically important bone morphogenetic protein-specific response elements in the Id1 promoter." *J Biol Chem* 277(7): 4883-91.
33. Katagiri, T., A. Yamaguchi, et al. (1994). "Bone morphogenetic protein-2 converts the differentiation pathway of C2C12 myoblasts into the osteoblast lineage." *J Cell Biol* 127(6 Pt 1): 1755-66.
34. Rossier-Pansier, L., F. Baruthio, et al. (2008). "Compartmentalization in membrane rafts defines a pool of N-cadherin associated with catenins and not engaged in cell-cell junctions in melanoma cells." *J Cell Biochem* 103(3): 957-71.
35. Guicheux, J., J. Lemonnier, et al. (2003). "Activation of p38 mitogen-activated protein kinase and c-Jun-NH2-terminal kinase by BMP-2 and their implication in the stimulation of osteoblastic cell differentiation." *J Bone Miner Res* 18(11): 2060-8.
36. Kusumi, A., C. Nakada, et al. (2005). "Paradigm shift of the plasma membrane concept from the two-dimensional continuum fluid to the partitioned fluid: high-speed single-molecule tracking of membrane molecules." *Annu Rev Biophys Biomol Struct* 34: 351-78.
37. Wheeler, D., W. B. Sneddon, et al. (2007). "NHERF-1 and the cytoskeleton regulate the traffic and membrane dynamics of G protein-coupled receptors." *J Biol Chem* 282(34): 25076-87.

3

Quantum dots for single-molecule biological imaging on native cell membranes

Quantum dots have lately been presented as an useful and effective tool for the visualization and tracking of individual proteins on the cell surface. Usage of these nanoparticles and QD-labeling methods, however, still require optimization, especially to allow more exact calculation of the membrane protein stoichiometries in larger assemblies. In this study described are methods that augment the number of signals and the tracking times of diverse QD types. These techniques were applied to peruse interleukin-5 β -common chain receptor (IL-5R β c) receptors that are endogenously expressed at low level on living differentiated eosinophil-like HL-60 cells.

Gathered data reveal that examined receptors form stable and higher order oligomers. Higher than 10% maximization of uninterrupted trajectories of totally uninterrupted 1000-step trajectories displays two patterns of confined motion. Thereupon procedures were evolved that enable determination of stoichiometries of cell surface protein complexes, even at native non-transfected levels, as well as the observation of long trajectories to analyze their mobility.

Submitted to Nature Methods

Zelman-Femiak M, Noskov A, Lambright G, Bhushan S,

Lohse MJ, Harms GS

3.1. Introduction

Receptors play a decisive role in cellular signaling events, hence they are often a main object of studies and undergo investigation with the application of multiple techniques, from biochemical, pharmacological to microscopic ones. Most of the methods, unfortunately, provide averaged data that are based on a vast number of particular events. Additionally, frequently little information can be gained at all as the amount of studied molecules is below the detection level of the technique (<1000 molecules/cell). In such cases, any data from the biochemical assays vast volumes of cells are required and this either do not guarantee success. Microscopy could be a much more powerful tool regarding the resolution and sensitivity level to localize particular membrane proteins, however, there occur restrictions as well, concerning for example the necessity of *in situ* labeling like for the electron microscope measurements. A craving for *in vivo* approach with improved temporal resolution by microscopy has lacked so far the sensitivity and resolution to achieve the final goal: to follow a single receptor in living primary cells.

Recently, the advent of new labeling methods with small, fluorescent semiconductor nanocrystals, quantum dots, makes it possible to monitor single receptors in the membrane of living cells (1). QDs are 100-fold brighter than standard fluorophores, have a photostability of many hours, a relatively small size that is not much bigger from the common fluorescent proteins and an availability in many colors with ultraviolet or blue light excitation. Furthermore, QDs are commercially available with different biological functionalities (2,3).

The main benefit from the brightness and stability of the QDs is that single protein *in vivo* imaging becomes to be possible because the relatively low excitation power induces little cellular background allowing for high signal-to-noise ratios (exceeding 100:1) and thus sub-resolution limit “pointing accuracy” (4). What is more, QDs are rich in the high electron density enabling the primary cell or tissues samples to be subsequently fixed and re-imaged with high resolution electron microscopy (5). All mentioned reasons introduce quantum dots as a powerful tool that is able to bring a fresh insight into membrane receptor biology (6-11) and resolve fundamental doubts about cell data of such low receptor density.

However, reports of quantum dots for single-molecule tracking have not been consistent with a CCD camera system so far and the parameters required for the QD visualization on the cells have not been optimized. This is in contrast to other fluorescent techniques such as Fluorescence Correlation Spectroscopy, FCS (12). Defining and optimizing parameters for quantum dots in single-molecule microscopy seems to be requisite to acquire the best for the tracking detection level. For various natural and artificial fluorophores these parameters have already been reported (13,14,15).

QDs have one main feature, which occurs at times more pronounced than from standard fluorophores and which can be described as the emission rhythm based on the constant change between the 'on' state and intervals with no emission at all. This on-off situation is called 'blinking' and apart from it, QDs undergo photobleaching under continuous but albeit long periods of excitation (16), attributed to Auger ionization (16,17), but this process is not well understood (18-22). Continuous blinking could also be a serious incommodity in the analysis based on signals from individual quantum dots or their conjugates in flow cytometry or single-molecule biochips (23). The 'off' state of some QDs during measurement could decrease an overall signal to significantly alter stoichiometry measurements. In single tracking experiments blinking process has a special meaning as it can disturb acquiring the trajectories of maximal length.

In this investigation the photophysical behavior is characterized and the most optimal conditions for the quantum dot usage in single-molecule microscopy are determined. For the first time, we present the stoichiometry and mobility of individual interleukin receptors, the IL-5R β_c on living eosinophil-like cells.

3.2. Results & Discussion

3.2.1. Quantum dot properties

The first inevitable step in the examination of quantum dot photophysical characteristics was to determine the concentration in which the single QDs could be detected. Concentration dependent 2D samples of QDs were created (Figure 1). At the lowest concentrations (1 pM, Figure. 1) single QDs and single-step photobleaching, 'blinking' were observed (13,24).

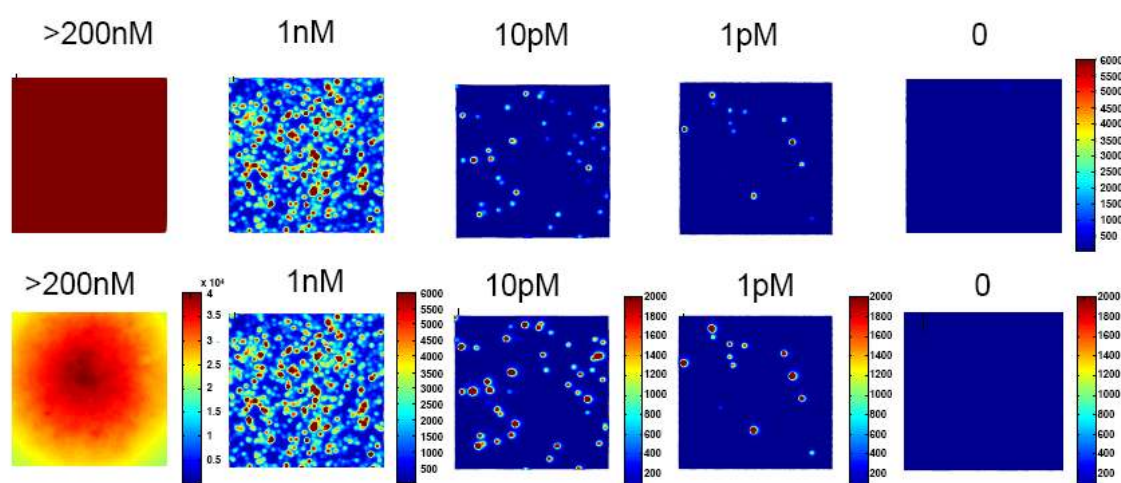


Figure 1. Fluorescent images of QD655. Solutions of the indicated concentrations of QDs in borate buffer with bovine serum albumin were spincoated with 10 μ l each on a glass coverslip. Upper row presents scaling to the level where single molecule are observed; bottom row is scaled to show the full intensity range of each image. All images were recorded at 1 kw/cm^2 for 5 ms.

In order to catch the moment when a molecule achieves a dark state and stops emitting individual QDs were tracked in sequential images for longer time periods to imitate *in vivo* recording times. Photobleaching was observed when the fluorescence does not come back after a while; and the blinking, when the fluorescence does re-appear.

The periodic character and intensity fluctuation of the QDs were outlined. From the data it was concluded that the blinking off time follows power law statistics:

$$P(t) \propto t^{-\alpha}$$

where $P(t)$ is the off time probability, t is the time of any 'OFF' event and α is descriptive exponent. Blinking statistics can solely be well-defined if a lower time cutoff

is verified for them. A lower cutoff time could shape the means to determine the distribution. In our experiments, this time was reached by the readout time (our minimum is found between 10 and 30ms) and signal-to-noise ratio of our CCD camera imaging system under single-molecule tracking conditions. The statistics of blinking events, however, should be separated from the fact that dark, non-fluorescing QDs exist (12,26) and also that some can be photoinduced (25).

To distinguish the various effects of blinking and intensity dependent photoinduction of quantum dots, an excitation dependent investigation was conducted in which QDs were mapped out spatially concerning the excitation intensity, I_{ex} , to ascertain if more QDs in diverse positions are excited with higher intensity and whether they are excited more often. (Figure 2 and 3).

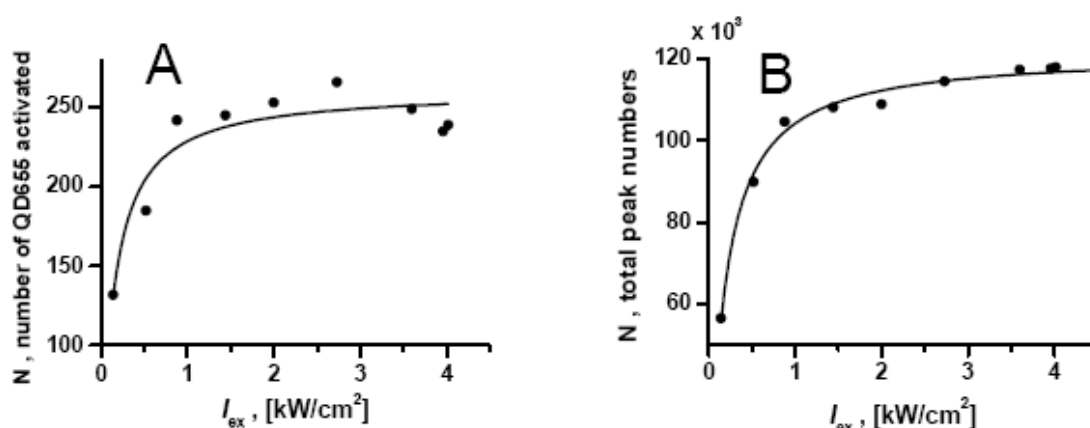


Figure 2. Fluorescent properties of quantum dots QD655. (A) Total number of QD655 photoinduced and recorded within a $32 \times 32 \mu\text{m}$ area as a function of I_{ex} . Application of excitation intensities above $1 \text{ kW}/\text{cm}^2$ does not cause a significant further increase in number of QDs. (B) Activation of fluorescence by increasing I_{ex} . Plotted is the total number of signal positions obtained in 1000-frames (5 s with 5 ms per frame) datasets. Data were fitted to the saturation equation given in the text to reveal $N^\infty=121773$, the maximum number of observations, and $I_s=0.1675 \text{ kW}/\text{cm}^2$ the intensity where 50% of the total positions were observed. Signal positions (± 0.5 pixel) at multiple frames were only counted once.

The results in Figure 2 and 3 demonstrate that increasing the excitation intensity leads to increasing numbers of individual spatially separated QDs achieving saturation above $\sim 1 \text{ kW}/\text{cm}^2$. Before data acquisition the sample regions in the experiment were illuminated for 30 seconds with excitation $> 5 \text{ kW}/\text{cm}^2$. We discovered this procedure to be necessary and sufficient to photoactivate the portion of QDs which became dim due to long periods of photoinactivity (25). The saturation intensities (I_s) that describe the excitation

intensity where 50% of the total fluorescent QD population begin to emit are 0.14 ± 0.03 and 0.17 ± 0.05 kW/cm² for Figure 2 A & B, respectively.

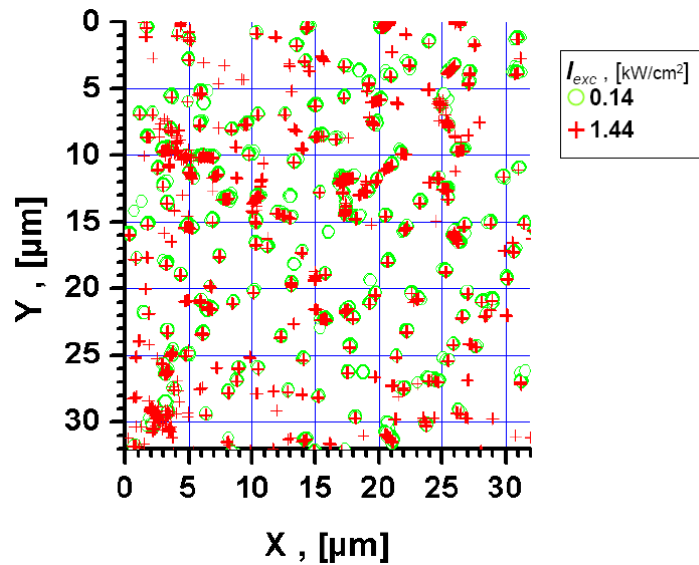


Figure 3. Example of the overlay of the signal positions. Detected signal positions in one focused sample region of spin coated QD655 on a glass coverslip at increasing excitation intensity. The data were fitted in 1000 frames datasets to count the total number of the photoactivated QDs. Data shown here were recorded over the same area at two I_{ex} – 0.14 (green circle) and 1.44 (red plus) kW/cm². The higher excitatoin intensity revealed twice as many positions.

It was shown also that blinking varied with excitation intensity and exposure time. Intensity traces (Figure 4A) were created from the total fluorescence values of integrated fluorescence from particular QDs. Application of power law statistics to ‘ON’ and ‘OFF’ data at individual excitation intensities proved that the power law exponent is large enough that a finite mean could exist for ‘ON’ and ‘OFF’ distributions.

At $I_{ex} > 1$ kW/cm² shorter mean ‘ON’-time periods were noticed in agreement with Figure 5A. The dependence of ‘ON/OFF’ time on excitation intensity follows the saturation model:

$$\tau_{on/off}(I) = \tau_{on/off}(\infty) \left(1 + \frac{I_s}{I} \right)^a$$

where I_s is the half-maximal saturation intensity, $a = 1$ for τ_{on} and -1 for τ_{off} and $\tau_{on/off}(\infty)$ is the ‘ON/OFF’ time at infinite excitation intensity (13,14). Increasing the excitation intensity enhanced QD blinking. The ‘ON’ periods became shorter, $I_s^{on} = 0.80$ [kW/cm²], until the ‘ON’ periods reached a plateau of $\tau_{on}(\infty) = 0.19$ seconds. However, the average ‘OFF’ periods increased solely moderately, $I_s^{off} = 0.66$ [kW/cm²], with $\tau_{off}(\infty) = 0.24$ seconds. We also observed that the trend for very long traces or even completely

non-blinking individual QDs was much greater at lower excitation intensity (Figure 5B). This indicate that a few particular QDs will never or less frequently blink during recording periods and will only begin to blink at higher ($> 1 \text{ kW/cm}^2$) excitation intensities. Quantum dots, their fluorescence and blinking are fully dependent from the excitation intensity.

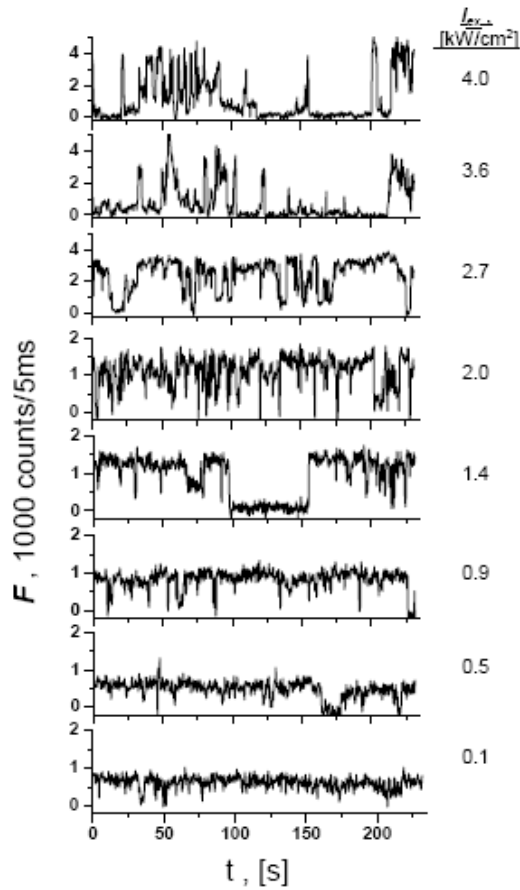


Figure 4. Examples of fluorescence intensity time trajectories. Increasing excitation intensity increased quantum dot emission but also start to blink more intensively - the 'ON' periods shorten and occur less frequently. This tendency is also clearly seen when the mean blinking 'ON/OFF'-times are plotted as a function of the excitation intensity

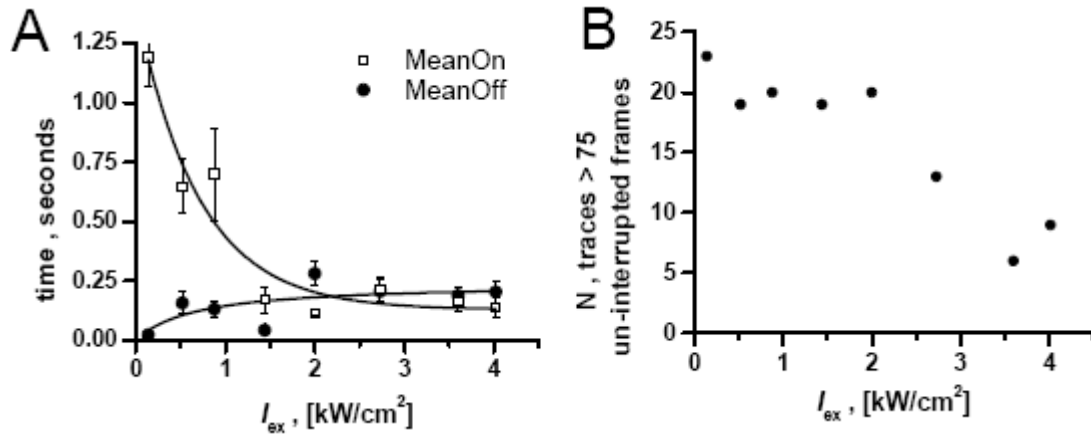


Figure 5. (A) „ON“-times (open squares) - $\tau_{on}^{\infty} = 0.19$ seconds, $I_s = 0.80$ kW/cm^2 . „OFF“-times (filled circles) - $\tau_{off}^{\infty} = 0.24$ seconds, $I_s = 0.66$ kW/cm^2 . (B) Number of traces longer than 75 uninterrupted frames observed within the average 1000 frame dataset. The trend shows the increase of blinking and reduction of the trace length with increasing excitation.

QDs present multiple levels of emission particularly at higher excitation intensities (Figure 6A , 6B) (17). It is clear to notice that at excitation intensities > 1 kW/cm^2 , the emission distributions contains multiple maxima. An Auger process is proposed to be responsible for that – i.e. that QDs lose electrons under high excitation and have lower emission or even photobleach (17,18). To study various fluorescence states and saturation, the fluorescence of the single QDs from 2D Gaussian fits was averaged from all individual observations in a dataset (Figure 6C). The excitation intensity-dependent fluorescence $\langle F(I) \rangle$ obeys the saturation model:

$$F(I) = F_0 \left(1 + \frac{I_s}{I} \right)^{-1}$$

where I_s is the half-maximal saturation intensity and F_0 is the maximum fluorescence. Emission increases in the excitation range with $I_s = 10.8$; 2.9 and 0.8 kW/cm^2 for QD655, EviDot603 and QD525, respectively. The saturation intensities are lower than the values reported by Doose et al. (12) by a factor of ~ 5 due to the difference in the time-scale. QD525 and EviDot603 had fluorescence of 10x and 20x less than QD655, what is attributed to the absorption coefficients which are reduced approximately by the same amount as that of QD655 at the corresponding excitation wavelengths. Hence, the fluorescence emission rate of the different QD types varies vastly and the excitation saturation intensities of the different types roughly follow the order of absorption coefficients.

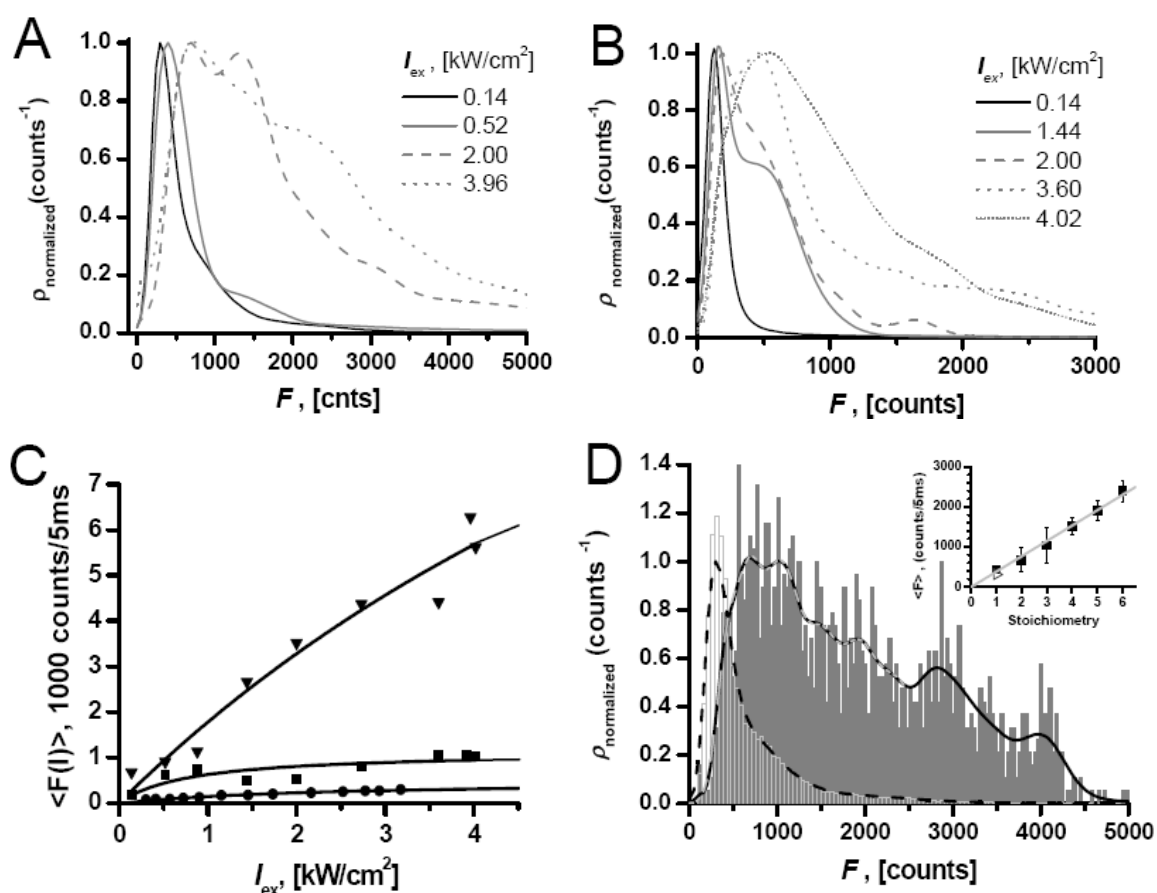


Figure 6. Fluorescence intensity probability distribution of QD655. Each probability density function, ρ , represents the distribution of the fluorescence signal intensity of at least 2000 individual observations of spincoated QDs. With increasing excitation intensity the probability to excite other fluorescence states greatly increases. (A) QD655 (B) EviDots603 (C) Saturation curves for the single QD fluorescence emission rate (photon counts/5ms) as function of the excitation intensity (I_{ex}). QD655(triangles): F_0 21045 photon counts/5ms, $I_s \sim 10$ kW/cm²; EviDot603(squares): $F_0=1126.90$ counts/5ms, $I_s =0.80$ kW/cm²; QD525(circles): $F_0 = 580$ counts/5ms, $I_s =2.9$ kW/cm². (D) Distribution of the fluorescence signal intensity constructed from 2133 individual observations of spin-coated QD655-biotin:avidin 1:1 molar ratio mix (grey filled bars) with corresponding probability density function, ρ (black curve) with $I_{ex} = 0.7$ kW/cm². The distribution was fitted for the signal intensities to 6 Gaussians (dashed light grey line). For comparison, the intensity distribution (light grey bars) obtained from QD655-Biotin solution without clustering by avidin displayed a corresponding probability density function, ρ (dashed curve). The positions of the maxima in the distribution were equidistant with a slope of 383 counts/5ms (inset).

3.2.2. Dark quantum dots and QD clustering

It has been previously described that some QDs are completely dark (26), thus we decided to investigate this fact. For that reason we placed QDs on transmission electron microscopy (TEM) grids and juxtaposed the mean fluorescence of multiple regions of QDs on the grids acquired on the fluorescence microscope to the actual QD number counted from TEM imaging (Figure 7).

The TEM images show a mean density of ~ 1100 QDs/ μm^2 . The mean fluorescence was 6500 counts/10ms/pixel with a pixel area of $0.04\mu\text{m}^2$. We observed that the average QD655 emits ~ 700 counts/10ms and that solely $\sim 50\%$ of QDs are excited (at $I_{\text{ex}} = 0.13$ kW/ cm^2), we appraise the QD density by fluorescence at 450 QDs/ μm^2 and that $\sim 60 \pm 10\%$ of QDs were totally dark. A rod like shape (Figure 7C) was observed for all of the QD655 quantum dots which was in agreement with the prior reported shape of QD655 (5). We noticed about one cluster of two quantum dots per ~ 30 QDs from the TEM images, what indicated no significant clustering of the QDs.

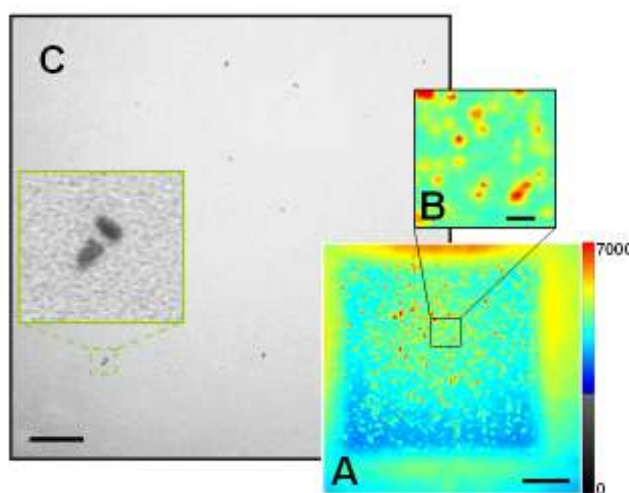


Figure 7. Comparison of the fluorescence intensity with the actual QD number. (A,B) Fluorescence image of a QD655 monomolecular layer deposited on an EM Grid and corresponding transmission electron micrograph, TEM (C). Scale bar: 10 μm (A), 1 μm (B), 0.01 μm (C).

3.2.3. Stoichiometry with quantum dots

Fluorescence distribution can predict and assay higher fluorescence levels of molecular clusters to determine local stoichiometry (24,27). That can be understood by contemplating the fluorescence distribution at $I_{\text{ex}} \leq 1$ kW/ cm^2 which comprises of one level with a minor shoulder attributed to higher emission states and to the low number of naturally occurring QD clusters. To better characterize determination of the stoichiometry with the fluorescence distribution profile, we forced clustering of biotin-coated QD655 with streptavidin.

The fluorescence image of small QD clusters does not vary from an image of single dots, apart that it shows higher intensity. However, QD blinking has a significant impact on an average intensity of a QD cluster, reducing it and this way making a direct

fluorescence intensity count more complicated. Correspondingly to the example with chemical dyes (24,27), the probability density function of the fluorescence intensity displays a discrete structure and could be fitted with a sum of multiple Gaussians to indicate the stoichiometry of many clusters (Figure 6D and 8). However, due to the effect of totally dark (~50%) and blinking (~40%) QDs, a correction to these values must be included for which a binominal model is applied (24) with the general formula:

$$P_n = r_n q^n$$

where P_n is the best approximated maximum monitored fluorescence distribution peak with n designating the stoichiometry number, q^n representing the pure fluorescence of the n^{th} level and r_n representing the relative amount at the q^n level. The next lower fluorescence level is then affected by the dark and blinking QDs from the high level stoichiometry and as well from the totally bright clusters:

$$P_{n-1} = r_n q^{n-1} (1 - q) + r_{n-1} q^{n-1}$$

This process continues until the sum of the probabilities:

$$\sum P_n \dots P_{n-1} \dots P_1$$

reproduces the experimentally determined fluorescence stoichiometry distribution and relative values

$$r_n \dots r_{n-1} \dots r_1$$

are subsequently obtained. If the constraint is set that:

$$\sum_1^n r_m = 1$$

the relative values are the corrected stoichiometries.

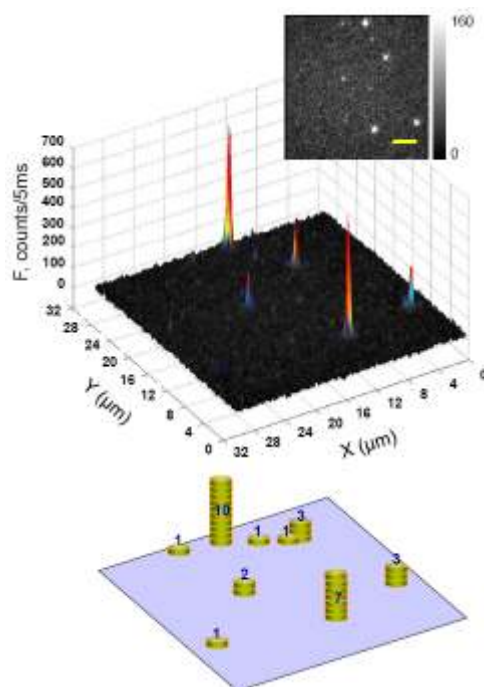


Figure 8. Local stoichiometry diagram. Intensity image in 3D showing different stoichiometry levels of a spincoated QD655-biotin:avidin 1:1 molar ratio mix that induced clustered “hot spots”. When imaged at low excitation intensity ($0.14\text{kW}/\text{cm}^2$ in this example) the probability to excite higher fluorescence states is negligible. Corresponding fluorescence intensity counting analysis image. The local stoichiometry of the biomolecule complexes could be estimated from the intensity of the signal which is divisible by the intensity of fluorescence signal from one QDot. Scale bar: $5\mu\text{m}$

To assure that presented data concerning the determination of stoichiometry were correct, we decided to prepare stoichiometric templates, a short oligonucleotide (T_{19}), in four different variants that covalently attached one, two, three or four QD655. The molecules were observed on transmission electron microscope and next their fluorescence was measured on the fluorescent microscope. This way a kind of QD dependent intensity ‘scale’ was obtained that could be utilized as the stoichiometry indicator in any experiments with 655 quantum dots under parallel conditions. (Figure 9). Concerning particular subtypes of the templates, we measured also a mean fluorescence from several different regions containing many QD-oligonucleotide. The fluorescence distribution in cases of the sample with the higher QD number affixed to the nucleotide, i.e. QD_2T_{19} , QD_3T_{19} and QD_4T_{19} revealed that the purification of those samples was not fully completed and each of them embodied also some amount of molecules of the lower complex grade respectively.

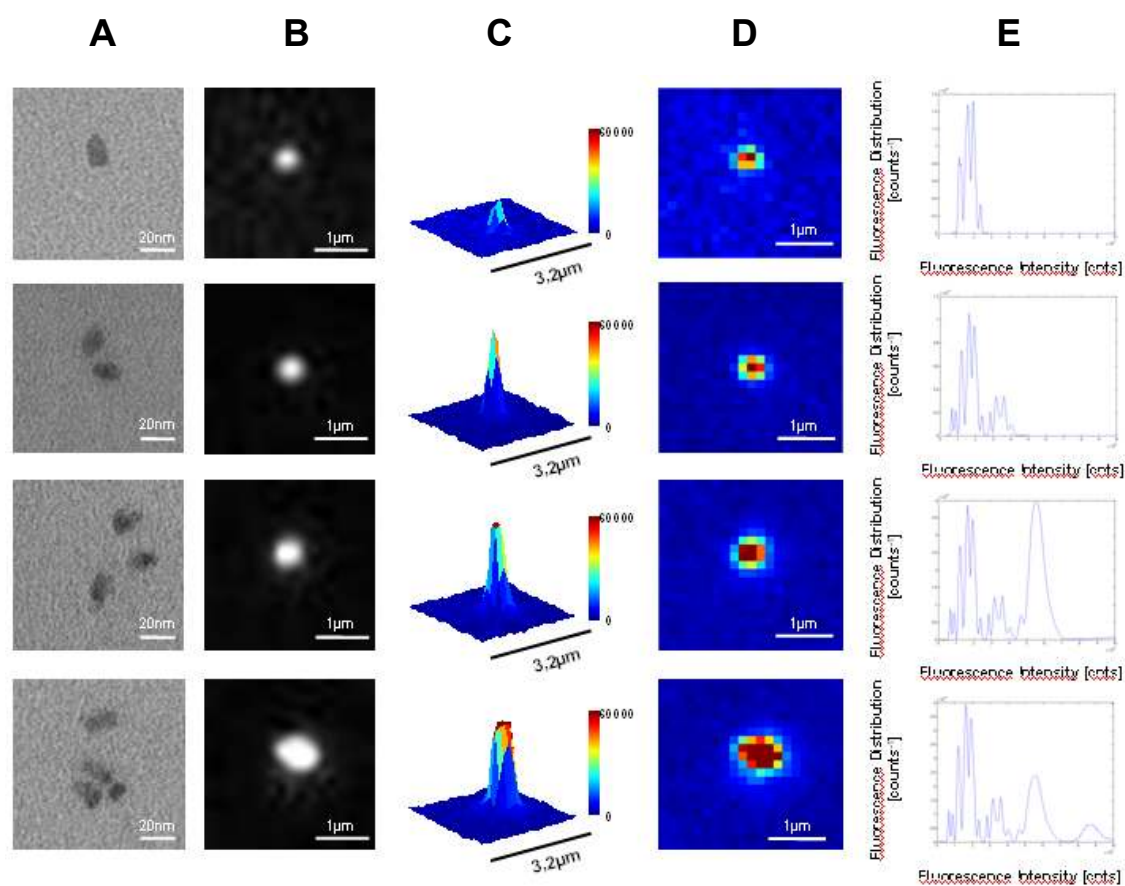


Figure 9. QD stoichiometric templates. Transmission electron microscope images of one, two, three and four QD655 that in each case are bound to the same type of oligonucleotide(A); Fluorescence images of the QDs from A (B); Fluorescence intensity scaling presenting different stoichiometry levels (C,D); Average fluorescence distribution for the each type of the template, created from the measurement of many different regions of the samples and indicating the presence of the molecules with lower number of QD attached in the samples of higher number QDs (E).

We wanted to implement this analysis to a biological example. Microscopy of IL-5R β_c interleukin receptors on living eosinophil-like cells requires single-molecule sensitivity due to the very low endogenous level of the receptors on the cell surface, 200-600 receptors per cell (28), but also requires a strong fluorophore because of the very high autofluorescence background. Observation attempts with organic dyes have not been possible (Figure 10).

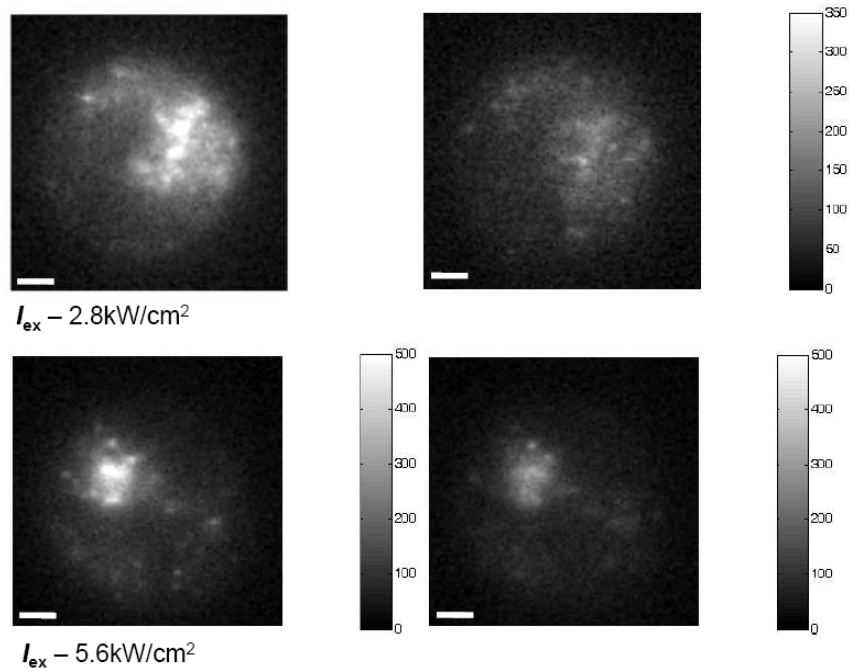


Figure 10. High autofluorescence background of eosinophil-like HL-60 cells. The detailed fluorescence microscopy of the IL-5/IL-3/GM-CSF receptor-ligand system is complicated. Two examples present the fluorescence images of eosinophil-like HL-60 cells taken before (left panels) and after (right panels) addition of the IL-5-TAMRA (tetramethyl rhodamine) conjugate. Even increased excitation intensity I_{ex} do not caused a single-molecule pattern. The background signal was essentially indistinguishable from the signal of the fluorophore. Scale bar: $1\mu\text{m}$

IL-5R β_c is the common receptor subunit in the interleukin-5 (IL-5) receptor system, of which high-affinity α -chain achieves specificity (29) (Figure 11). The receptor subunit is a single transmembrane spanning domain protein, has no intrinsic intracellular catalytic domains, and initiates signaling cascades through associated protein kinases. In humans, IL-5 plays important roles in proliferation, differentiation (30-32), migration (33), activation (34,35) and survival (36-39) of eosinophil-like cells. IL-5 is also crucial for inflammatory processes associated with general immunity and particularly with eosinophils, e.g. eosinophilia and allergic asthma (40).

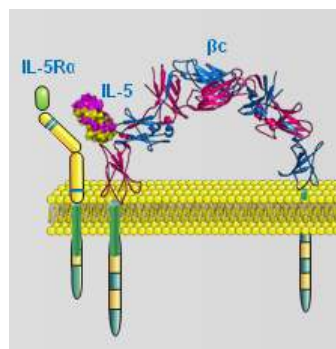


Figure 11. The Interleukin-5 receptor

Identification of IL-5R β_C on living cells with specific antibodies conjugated to QDs enabled to quantify the local stoichiometries of diffraction-limited regions with quantum dots *in vivo* and to gain information on receptor clustering (Figure 12).

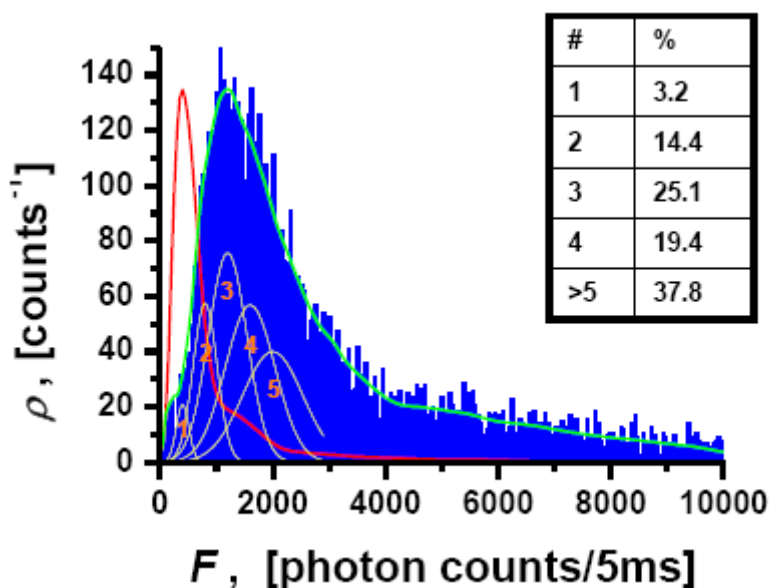


Figure 12. IL-5 receptor β_C clustering. Distribution (blue bars) and the corresponding probability density function ρ (green curve) of the fluorescence signal intensity created from 8185 independent observation on the eosinophil-like HL-60 cells. The data support that on the surface of the IL-5 receptor β_C occur with high probability ic clusters of 4 and higher as determined by the correction algorithms for blinking and dark QDs (27). For comparison the probability density function ρ_1 (red curve) for the intensity distribution of the non-clustered QD655-biotin solution obtained at the similar excitation intensity (0.52 [kW/cm 2]) is presented.

From the area of integration of the individual Gaussian peak components the predominant component appeared to be fluorescent trimers with $\sim 25\%$, followed by fluorescent tetramers with 19% and fluorescent dimers with 14%. However, upon accounting for the $\sim 40\%$ of blinking and $\sim 60\%$ of totally dark QDs in a binomial model, a maximum of clustering was found to be at a stoichiometry of 4, meaning prominent tetramer or higher order complex formation of these receptors in the eosinophil-like HL-60 cells.

3.2.4. Single Molecule Tracking of IL-5R β_C

Figure 13 depicts IL-5R β_C tracking on eosinophil-like HL-60 cells. The individual receptor clusters with QD655 were easily seen over time on the cell surface. Under low I_{ex} conditions it was possible to obtain a high number of long trajectories and low auto-fluorescence background. IL-5R β_C was measured with a signal-to-background ratio of >100 , resulting in a positional accuracy of 3.4 nm.

IL-5R β_C tracking exhibited two types of confined motion. First, there were regions from 300 up to 1400 nm in diameter where the receptors move with a fast diffusion coefficient ($D_{\text{lat}} = 0.363 \pm 0.035 \mu\text{m}^2/\text{s}$). Second, there were smaller confined regions with a diameter of 40-100 nm where the receptors moved with D_{lat} of $0.071 \pm 0.005 \mu\text{m}^2/\text{s}$.

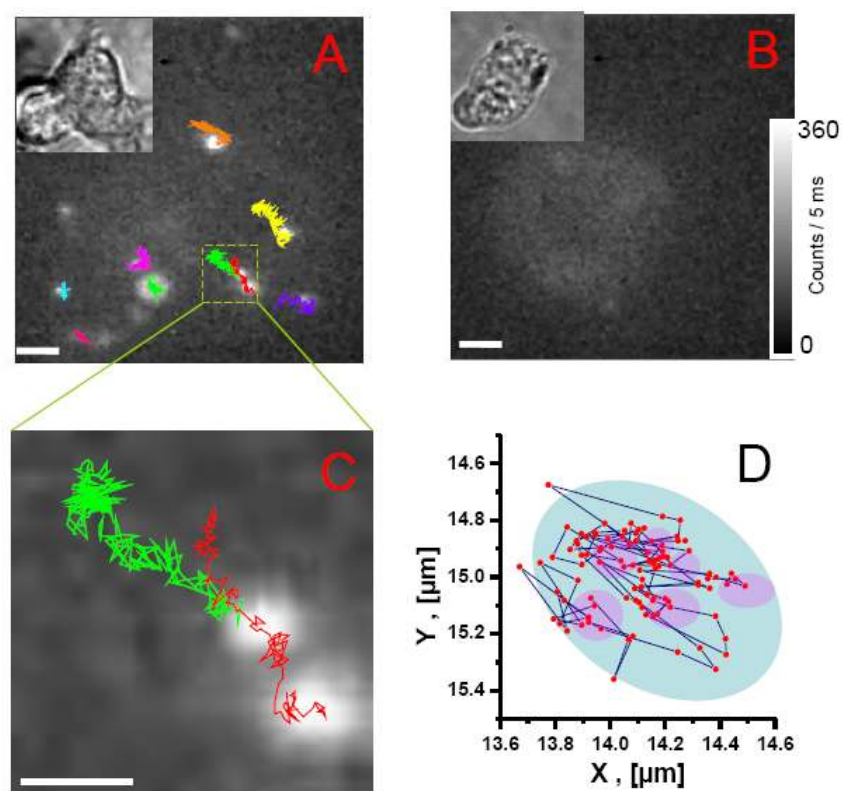
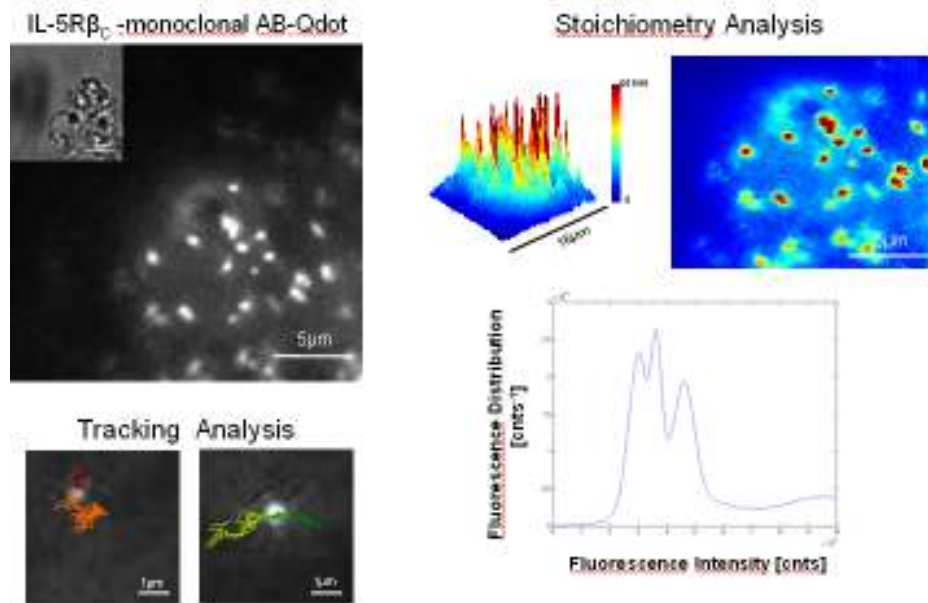


Figure 13. QD-IL-5 β_C imaging and tracking on living eosinophil-like HL-60 cells. (A,C) The bright spots (or “hot spots”) indicate the location of individual IL-5 receptor β_C subunits. Dim areas in the images represent background noise and background autofluorescence of the cell. Trajectories of clearly distinguished signals are shown as overlay. Data acquisition rate was 33.5 ms per frame. Scale bar: 2 μm (A); 1 μm (C); 1 μm (B). (B) Specific labeling control. The figure presents a cell subjected to the same labeling procedure without of anti- β_C Ab. D) Representative single-molecule trajectory showing two types of confined motion of the individual IL-5 receptor β_C subunits visualized with the help of a mouse anti- β_C antibody and goat anti-mouse QD655 conjugate.

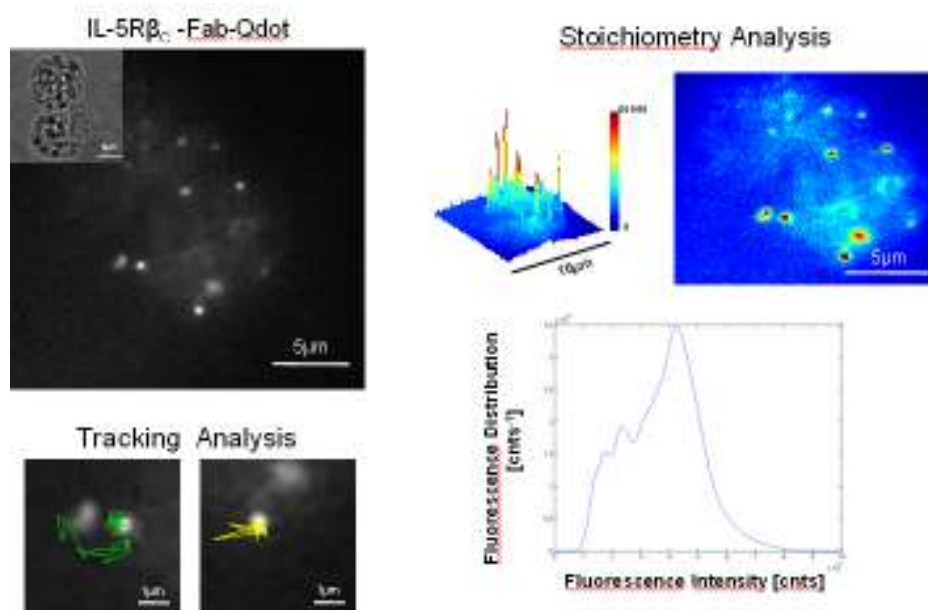
To verify that mobility and high cluster formation of IL-5R β_C receptors was not influenced or induced through QD-antibody labeling technique, we decided to produce suitable QD-Fab fragments suitable for this labeling and to compare fluorescent images (Figure 14, A and B). In both cases clusters of receptors were observed. Additionally, for

the control, we labeled and measured another receptor on HL-60 cells that we know to be non-aggregating (Figure 14C). That definitively proved that it was not a labeling method to initiate IL-5R β_c receptors clustering, but natural way in which this receptors occur at the cell membrane.

A



B



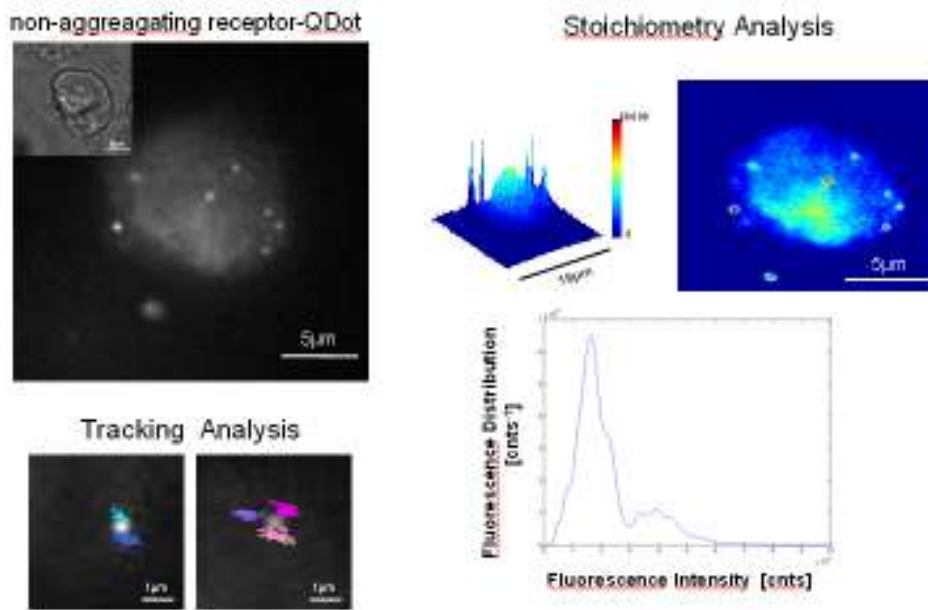
C

Figure 14. Verification of the IL-5R β_C receptor mobility and clustering type. IL-5R β_C mobility and clustering pattern after receptor labeling with QD-monoclonal antibody (A); Labeling of IL-5R β_C was performed with QD-Fab fragments. Observed clustering was very similar to A (B); Non-aggregating receptor profile on HL-60 cells proved definitively that clustering is a natural way of occurrence for IL-5R β_C receptors.(C); Scale bar: on all bigger images 5 μ m, on smaller 1 μ m.

3.2.5. Discussion

The conditions for the optimal use of QDs were the main subject of this study. We have tested commercially available QDs to best apply them for single-molecule tracking. With the optimal excitation parameters, QDs produce extremely long trajectories of over 100 uninterrupted frames (5 ms/frame, ie. 500 ms). We clearly show the utility of these parameters in microscopy and present a direct example with the tracking and local stoichiometry determination of IL-5R β_C interleukin receptors on living eosinophil-like cells.

Our work demonstrates that despite blinking and $\sim 60 \pm 10$ % of totally dark QDs, individual quantum dots under an excitation intensity of just below 1 kW/cm² have in general higher emission rates than many of the standard fluorophores. *In vivo*, single-molecule fluorescence experiments require the highest signals with the highest excitation percentage and lowest photobleaching, blinking, and autofluorescence levels. By choosing the condition of ~ 1 kW/cm² with 5 ms excitation, we were able to easily obtain average, uninterrupted trajectory lengths from 15 to over 100 steps with > 10% of

the whole population not blinking at all (at 5 ms/image) – at least five to twenty times longer before an ‘OFF’-state than the best commercially available organic fluorophores. This condition also ensures that roughly 40% of all QDs will be observed.

Although longer traces can be recorded from metallic nanoparticles with ultimately lower time resolution, multiple-color-localization and analysis of stoichiometry are only possible with QD fluorescence tracking. Under our optimized conditions, we had signal to background ratios exceeding 100:1 what allows positional accuracy of <4 nm. The minimum imaging exposure time can be reduced depending on the noise and sample background. Typical minimal values are as low as 1 ms. The emission wavelength of the QDs and the manufacturer also play a role in fluorescence brightness and photoinduced activation. The red-shifted QD655 from QDot Corp. is > 10x brighter than QD525 (QDot Corp.) and EviDot 603 (Evident Technologies), and also the QD655 and QD525 are more easily photoinduced than EviDot603.

In comparison to other fluorophores by our previously defined R-value, a benchmark of how many molecules it would take to mask the emission of a single, emitting fluorophore, the QD versus flavin fluorescence ratio is apparently $>10^5$, in comparison to eYFP with a ratio of 405 (13,14). (Flavin is the chief component of cellular autofluorescence in vertebrate cells.) This can be interpreted that for cells containing high levels of flavins, it may still not be possible to detect single QD655 or individual quantum dots because the background is too high, but that QDots are much better than other standard fluorophores (13,14). This limitation for QDs could be overcome by bleaching the cells for longer periods because the bleaching half-life of QDs is ~14 hours at ~ 1kW/cm², whereas flavins and other endogenous fluorophores bleach within a few seconds at this light intensity.

Achievements of single molecule sensitivity by fluorescence permit a detailed analysis of local stoichiometries directly on the surface of the live cells. The stoichiometry of the IL-5 receptor-ligand signaling complex determined this way is valuable as a complement to the crystallographic structure of the interleukin receptor-ligand complex. Resolution of the 3D structure for the recombinantly expressed extracellular domain of the receptor β_c reveals a stable intertwined homodimer (41,42) raising concerns over previously postulated 1:1:1 stoichiometry models of IL-5:IL-5R α : β_c (29,43,44). From biochemical separation methods with soluble Granulocyte-Macrophage Colony Stimulating Factor Receptor (hGM-CSF-Receptor- α) and the extracellular soluble part of β_c , one GM-CSF is recognized by one hGM-CSF R α with recruitment of 2 molecules of

β_c (45). Our results suggest that on native and comparatively natural, undisturbed cellular surfaces, non-active IL-5R β_c may be aggregated in clusters of four and more subunits suggesting more complex activation mechanisms than previously anticipated. This example further shows that QDs allow the detection of low levels of endogenously present biomolecules in a very difficult, physiologically native environment.

We expect that QDs will be the fluorophore of choice for standard single-membrane protein stoichiometry and tracking studies, and that they can be further improved by solving limitations that this study quantifies such as blinking and dark states. Using our optimized methods, they can already now be used to visualize single-molecules under difficult conditions.

3.3. Materials and methods

3.3.1. *Quantum dots*

QD525, QD655 Biotin or Streptavidin conjugates were acquired from QDot Corporation, Hayward, CA and EviDot603 (EviTags Fort Orange-COOH) were from Evident Technologies, Troy NY, USA. Avidin was from Sigma (Sigma-Aldrich, Germany).

3.3.2. *Complex preparation*

To model receptor clustering we induced restricted aggregation of QDs. 10 μ l of 50 pM avidin solution in 50 mM borate/HCl pH 8.3 was added portionwise to 10 μ l of 2 nM suspension of QD655-Biotin in same buffer (molar ratio 1:4). The reaction was performed at 4°C with intensive shaking.

3.3.3. *Films and Spin Coating*

For the spincoating the 2 nM (or 1 nM in a case of the complex suspensions) of QD suspensions were serially diluted 1:10 to create concentration steps from 2×10^{-9} to 2×10^{-12} in either 1% polyvinyl alcohol (PVA, Roth Chemicals, Germany) aqueous solution or in 50 mM borate/HCl pH 8.3 buffer containing 0.1% bovine serum albumin. Monomolecular layers (spincoats) were created on cleaned glass slides by adding 20 μ l of the fluorophore solution with a spin coater (SPI, KW-4a, PA, USA) in two stages: first for 10 seconds at 300 rpm and then for 2.5 minutes at 2,000 rpm.

In all cases, the glass coverslips were cleaned in 10% NaOH (AppliChem, Germany) with sonication for 10 minutes and rinsed in 18 MOhm-water (Millipore, USA) prior to use.

3.3.4. *Cell culture*

Eosinophilic cells (15HL-60E) were obtained as previously described (46). In brief, the HL-60 clone 15 cells (ATCC Cat. No.: CRL-1964) were grown in RPMI1640 medium supplemented with 10% FCS, 25mM HEPES pH7.6 and antibiotics and differentiated in the same medium with 0.5mM sodium butyrate (Sigma-Aldrich, Germany) for at least one week.

3.3.5. Single-molecule imaging

The experimental arrangement for single-molecule imaging has been described in detail previously (13,14,24). The samples were mounted onto an inverted microscope (Zeiss, Axiovert 200, Germany) equipped with a 100× objective (NA=1.4, Zeiss, Germany), and illuminated for 1-30 ms by an Ar-laser (Coherent Innova 308, USA) synchronized with the exposure of the Peltier-cooled CCD-camera system (Spec-10, 400B or 1300 B, Roper Scientific, USA). The synchronization was achieved with custom-built electronics between CCD-camera-exposure and shutter, and acousto-optic time-frequency modulator (AOTF, AA Optic, France). The following filter combinations were used: DCLP525 and HQ655/40 (Chroma, VT, USA) or OG550 (Schott, Germany) for QD655 and EviTags 603, DCLP498 and HQ 525/50 for QD525 (Chroma, VT, USA). The total detection efficiency of the experimental setup was ~13% for QD655 (and ~ 7 % for EviTags 603 and QD525). The photon counts were determined with a precision of $\sim \pm 15\%$.

Same sample regions of individually resolved QDots were recorded in sets of 1000 consecutive images illuminating and exposing for 5 ms with recording each set at one illumination intensity from 0.05 to 5 kW/cm². These are typical value ranges for the observation of single quantum dots and other fluorophores. Longer and shorter integration periods were tested but not reported here as they lead to the same conclusions.

3.3.6. Data and mobility analysis

Data processing and mobility analysis were conducted like in aforementioned protocols in points 1.3.7. and 1.3.8.

3.3.7. Immunolabeling

An aliquot of ($1 \cdot 10^6$) 15HL-60E cell suspension in culture medium was incubated at 37°C, 5%CO₂ for 20 minutes in the presence of 400 ng/ml non-blocking anti-β_c-mouse monoclonal IgG₁ (1C1, sc-21765 Santa-Cruz Biotechnology, USA). The suspension was washed with RPMI1640 (Sigma) and resuspended in RPMI1640, 0,3% Ig-free BSA plus 1 nM QDot™655 goat F(ab')₂ anti-Mouse IgG conjugate (QD Corporation, Hayward, CA). After 10 minutes incubation (37°C, 5%CO₂), cells were washed twice with prewarmed RPMI1640 for 1 min with centrifugation ($1 \cdot 10^3$ rpm, 37°C) (Eppendorf). Cells were imaged in RPMI1640 at 37°C.

3.3.8. Fab-QD655 Fragment production

Fab fragment of IL3/IL-5/GM-CSFR β antibody (Santa Cruz Biotechnology, sc-21765) was produced with Fab Preparation Kit (Thermo Scientific) and ICONTM Concentrator (Pierce) and next conjugated to QD655 with the usage of Qdot Antibody Conjugation Kit (NrQ22021MP; Molecular Probes, Invitrogen Detection Technologies, Eugene, Oregon, USA; Invitrogen, Karlsruhe, Germany) .

3.3.9. TEM Imaging

Electron micrographs were taken from dried films containing QDots at 80kV with a Zeiss EM900 transmission electron microscope.

3.4. References

1. Dahan,M., Levi,S., Luccardini,C., Rostaing,P., Riveau,B., & Triller,A. Diffusion dynamics of glycine receptors revealed by single-quantum dot tracking. *Science* 302, 442-445 (2003).
2. Alivisatos,P. The use of nanocrystals in biological detection. *Nat. Biotechnol.* 22, 47-52 (2004).
3. Giepmans,B.N., Adams,S.R., Ellisman,M.H., & Tsien,R.Y. The fluorescent toolbox for assessing protein location and function. *Science* 312, 217-224 (2006).
4. Thompson,R.E., Larson,D.R., & Webb,W.W. Precise nanometer localization analysis for individual fluorescent probes. *Biophys. J.* 82, 2775-2783 (2002).
5. Giepmans,B.N., Deerinck,T.J., Smarr,B.L., Jones,Y.Z., & Ellisman,M.H. Correlated light and electron microscopic imaging of multiple endogenous proteins using Quantum dots. *Nat. Methods* 2, 743-749 (2005).
6. Battersby,B.J. & Trau,M. Novel miniaturized systems in high-throughput screening. *Trends Biotechnol.* 20, 167-173 (2002).
7. Stroh,M., Zimmer,J.P., Duda,D.G., Levchenko,T.S., Cohen,K.S., Brown,E.B., Scadden,D.T., Torchilin,V.P., Bawendi,M.G., Fukumura,D., & Jain,R.K. Quantum dots spectrally distinguish multiple species within the tumor milieu in vivo. *Nat. Med.* 11, 678-682 (2005).
8. Bakalova,R., Zhelev,Z., Ohba,H., & Baba,Y. Quantum dot-based western blot technology for ultrasensitive detection of tracer proteins. Quantum dot-conjugated hybridization probes for preliminary screening of siRNA sequences. *J. Am. Chem. Soc.* 127, 9328-9329 (2005).
9. Larson,D.R., Zipfel,W.R., Williams,R.M., Clark,S.W., Bruchez,M.P., Wise,F.W., & Webb,W.W. Water-soluble quantum dots for multiphoton fluorescence imaging in vivo. *Science* 300, 1434-1436 (2003).
10. Gao,X., Cui,Y., Levenson,R.M., Chung,L.W., & Nie,S. In vivo cancer targeting and imaging with semiconductor quantum dots. *Nat. Biotechnol.* 22, 969-976 (2004).
11. Kim,S., Lim,Y.T., Soltész,E.G., De Grand,A.M., Lee,J., Nakayama,A., Parker,J.A., Mihaljevic,T., Laurence,R.G., Dor,D.M., Cohn,L.H., Bawendi,M.G., & Frangioni,J.V. Near-infrared fluorescent type II quantum dots for sentinel lymph node mapping. *Nat. Biotechnol.* 22, 93-97 (2004).
12. Doose,S., Tsay,J.M., Pinaud,F., & Weiss,S. Comparison of photophysical and colloidal properties of biocompatible semiconductor nanocrystals using fluorescence correlation spectroscopy. *Anal. Chem.* 77, 2235-2242 (2005).

13. Harms,G.S., Cognet,L., Lommerse,P.H., Blab,G.A., & Schmidt,T. Autofluorescent proteins in single-molecule research: applications to live cell imaging microscopy. *Biophys. J.* 80, 2396-2408 (2001).
14. Steinmeyer,R., Noskov,A., Krasel,C., Weber,I., Dees,C., & Harms,G.S. Improved fluorescent proteins for single-molecule research in molecular tracking and co-localization. *J. Fluoresc.* 15, 707-721 (2005).
15. Schmidt, T., Schuetz, G.J., Baumgartner, W., Gruber, H.J. & Schindler, H. Characterization of photophysics and mobility of single molecules in a fluid lipid membrane. *J. Phys. Chem.* 99, 17662-17668 (1995).
16. Kagan,C.R., Murray,C.B., Nirmal,M., & Bawendi,M.G. Electronic energy transfer in CdSe quantum dot solids. *Phys. Rev. Lett.* 76, 1517-1520 (1996).
17. Efros,A.L., Rosen,M., Kuno,M., Nirmal,M., Norris,D.J., & Bawendi,M. Band-edge exciton in quantum dots of semiconductors with a degenerate valence band: Dark and bright exciton states. *Phys. Rev. B. Cond. Mat.* 54, 4843-4856 (1996).
18. Hohng,S. & Ha,T. Near-complete suppression of quantum dot blinking in ambient conditions. *J. Am. Chem. Soc.* 126, 1324-1325 (2004).
19. Chung,I., Witkoskie,J.B., Cao,J., & Bawendi,M.G. Description of the fluorescence intensity time trace of collections of CdSe nanocrystal quantum dots based on single quantum dot fluorescence blinking statistics. *Phys. Rev. E. Stat. Nonlin. Soft. Matter Phys.* 73, 011106 (2006).
20. Bianco,S., Grigolini,P., & Paradisi,P. Fluorescence intermittency in blinking quantum dots: renewal or slow modulation? *J. Chem. Phys.* 123, 174704 (2005).
21. Yao,J., Larson,D.R., Vishwasrao,H.D., Zipfel,W.R., & Webb,W.W. Blinking and nonradiant dark fraction of water-soluble quantum dots in aqueous solution. *Proc. Natl. Acad. Sci. U. S. A* 102, 14284-14289 (2005).
22. Tang,J. & Marcus,R.A. Mechanisms of fluorescence blinking in semiconductor nanocrystal quantum dots. *J. Chem. Phys.* 123, 054704 (2005).
23. Stavis,S.M., Edel,J.B., Samiec,K.T., & Craighead,H.G. Single molecule studies of quantum dot conjugates in a submicrometer fluidic channel. *Lab Chip.* 5, 337-343 (2005).
24. Harms,G.S., Cognet,L., Lommerse,P.H., Blab,G.A., Kahr,H., Gamsjager,R., Spaink,H.P., Soldatov,N.M., Romanin,C., & Schmidt,T. Single-molecule imaging of L-type Ca(2+) channels in live cells. *Biophys. J.* 81, 2639-2646 (2001).
25. Silver,J. & Ou,W. Photoactivation of quantum dot fluorescence following endocytosis. *Nano. Lett.* 5, 1445-1449 (2005).
26. Ebenstein,Y., Mokari,T., & Banin,U. Fluorescence quantum yield of CdSe/ZnS nanocrystals investigated by correlated atomic-force and single-particle fluorescence microscopy. *Applied Physics Letters* 80, 4033-4035 (2002).
27. Schmidt, T., Schuetz, G.J., Gruber, H.J. & Schindler, H. Local stoichiometries determined by counting individual molecules. *Anal. Chem.* 68, 4397-4401 (1996).

28. Plaetinck,G., Van Der,H.J., Tavernier,J., Fache,I., Tuypens,T., Fischkoff,S., Fiers,W., & Devos,R. Characterization of interleukin 5 receptors on eosinophilic sublines from human promyelocytic leukemia (HL-60) cells. *J. Exp. Med.* 172, 683-691 (1990).
29. Devos,R., Guisez,Y., Cornelis,S., Verhee,A., Van Der,H.J., Manneberg,M., Lahm,H.W., Fiers,W., Tavernier,J., & Plaetinck,G. Recombinant soluble human interleukin-5 (hIL-5) receptor molecules. Cross-linking and stoichiometry of binding to IL-5. *J. Biol. Chem.* 268, 6581-6587 (1993).
30. Clutterbuck,E.J., Hirst,E.M., & Sanderson,C.J. Human interleukin-5 (IL-5) regulates the production of eosinophils in human bone marrow cultures: comparison and interaction with IL-1, IL-3, IL-6, and GM-CSF. *Blood* 73, 1504-1512 (1989).
31. Enokihara,H., Furusawa,S., Nakakubo,H., Kajitani,H., Nagashima,S., Saito,K., Shishido,H., Hitoshi,Y., Takatsu,K., & Noma,T. T cells from eosinophilic patients produce interleukin-5 with interleukin-2 stimulation. *Blood* 73, 1809-1813 (1989).
32. Karlen,S., De Boer,M.L., Lipscombe,R.J., Lutz,W., Mordvinov,V.A., & Sanderson,C.J. Biological and molecular characteristics of interleukin-5 and its receptor. *Int. Rev. Immunol.* 16, 227-247 (1998).
33. Wang,J.M., Rambaldi,A., Biondi,A., Chen,Z.G., Sanderson,C.J., & Mantovani,A. Recombinant human interleukin 5 is a selective eosinophil chemoattractant. *Eur. J. Immunol.* 19, 701-705 (1989).
34. Coffey,P.J., Schweizer,R.C., Dubois,G.R., Maikoe,T., Lammers,J.W., & Koenderman,L. Analysis of signal transduction pathways in human eosinophils activated by chemoattractants and the T-helper 2-derived cytokines interleukin-4 and interleukin-5. *Blood* 91, 2547-2557 (1998).
35. Kita,H., Weiler,D.A., Abu-Ghazaleh,R., Sanderson,C.J., & Gleich,G.J. Release of granule proteins from eosinophils cultured with IL-5. *J. Immunol.* 149, 629-635 (1992).
36. Owen,W.F., Rothenberg,M.E., Petersen,J., Weller,P.F., Silberstein,D., Sheffer,A.L., Stevens,R.L., Soberman,R.J., & Austen,K.F. Interleukin 5 and phenotypically altered eosinophils in the blood of patients with the idiopathic hypereosinophilic syndrome. *J. Exp. Med.* 170, 343-348 (1989).
37. Yousefi,S., Hoessli,D.C., Blaser,K., Mills,G.B., & Simon,H.U. Requirement of Lyn and Syk tyrosine kinases for the prevention of apoptosis by cytokines in human eosinophils. *J. Exp. Med.* 183, 1407-1414 (1996).
38. Alam,R., Pazdrak,K., Stafford,S., & Forsythe,P. The interleukin-5/receptor interaction activates Lyn and Jak2 tyrosine kinases and propagates signals via the Ras-Raf-1-MAP kinase and the Jak-STAT pathways in eosinophils. *Int. Arch. Allergy Immunol.* 107, 226-227 (1995).
39. Pazdrak,K., Schreiber,D., Forsythe,P., Justement,L., & Alam,R. The intracellular signal transduction mechanism of interleukin 5 in eosinophils: the involvement of lyn tyrosine kinase and the Ras-Raf-1-MEK-microtubule-associated protein kinase pathway. *J. Exp. Med.* 181, 1827-1834 (1995).

40. Wills-Karp, M. Immunologic basis of antigen-induced airway hyperresponsiveness. *Annu. Rev. Immunol.* 17, 255-281 (1999).
41. Carr, P.D., Gustin, S.E., Church, A.P., Murphy, J.M., Ford, S.C., Mann, D.A., Woltring, D.M., Walker, I., Ollis, D.L., & Young, I.G. Structure of the complete extracellular domain of the common beta subunit of the human GM-CSF, IL-3, and IL-5 receptors reveals a novel dimer configuration. *Cell* 104, 291-300 (2001).
42. Gustin, S.E., Church, A.P., Ford, S.C., Mann, D.A., Carr, P.D., Ollis, D.L., & Young, I.G. Expression, crystallization and derivatization of the complete extracellular domain of the beta(c) subunit of the human IL-5, IL-3 and GM-CSF receptors. *Eur. J. Biochem.* 268, 2905-2911 (2001).
43. Yamaguchi, N., Hitoshi, Y., Takaki, S., Murata, Y., Migita, M., Kamiya, T., Minowada, J., Tominaga, A., & Takatsu, K. Murine interleukin 5 receptor isolated by immunoaffinity chromatography: comparison of determined N-terminal sequence and deduced primary sequence from cDNA and implication of a role of the intracytoplasmic domain. *Int. Immunol.* 3, 889-898 (1991).
44. Brown, P.M., Tagari, P., Rowan, K.R., Yu, V.L., O'Neill, G.P., Middaugh, C.R., Sanyal, G., Ford-Hutchinson, A.W., & Nicholson, D.W. Epitope-labeled soluble human interleukin-5 (IL-5) receptors. Affinity cross-link labeling, IL-5 binding, and biological activity. *J. Biol. Chem.* 270, 29236-29243 (1995).
45. McClure, B.J., Hercus, T.R., Cambareli, B.A., Woodcock, J.M., Bagley, C.J., Howlett, G.J., & Lopez, A.F. Molecular assembly of the ternary granulocyte-macrophage colony-stimulating factor receptor complex. *Blood* 101, 1308-1315 (2003).
46. Fischkoff, S.A. Graded increase in probability of eosinophilic differentiation of HL-60 promyelocytic leukemia cells induced by culture under alkaline conditions. *Leuk. Res.* 12, 679-686 (1988).
47. Powles, J.G., Mallett, M.J.D., Rickayzen, G., & Evans, W.A.B. Exact Analytic Solutions for Diffusion Impeded by An Infinite Array of Partially Permeable Barriers. *Proceedings of the Royal Society of London Series A-Mathematical Physical and Engineering Sciences* 436, 391-403 (1992).
48. Kusumi, A., Sako, Y., & Yamamoto, M. Confined lateral diffusion of membrane receptors as studied by single particle tracking (nanovid microscopy). Effects of calcium-induced differentiation in cultured epithelial cells. *Biophys. J* 65, 2021-2040 (1993).
49. Saxton, M.J. & Jacobson, K. Single-particle tracking: applications to membrane dynamics. *Annu. Rev. Biophys. Biomol. Struct.* 26, 373-399 (1997).

4

PTHR – parathyroid hormone receptor mobility, internalization and recycling in single-molecule studies

The receptor for parathyroid hormone (PTH) and PTH-related protein (PTHrP) is entailed in the regulation of calcium homeostasis and in bone remodeling (1). Agonist occupancy of the PTH/PTHrP receptor (PTHR) leads to activation of adenylyl cyclase (via G_s), and phosphatidylinositol-specific phospholipase C_β (via G_q). PTH-induced activation of the PTHR results in the internalization of the PTH-receptor complex via the clathrin-coated pit pathway and engages β -arrestin2 (2,3).

Internalization, in general, enables to diminish the magnitude of the receptor-mediated G protein signals (desensitization), receptor resensitization (via recycling), degradation (down-regulation), and coupling to other signaling pathways (e.g. MAP kinases).

GPCR internalization process maintains still one of the most addressed, particularly regarding the determinants that are involved.

In this study we tend to stare at the parathyroid hormone receptor type 1 mobility on living cells in order to better characterize its internalization and as well to follow its recycling dynamics.

4.1. Introduction

The parathyroid hormone receptor type 1 (PTHr1) belongs to Family B of the seven transmembrane G protein-coupled receptor (GPCR) superfamily and is activated by two ligands, parathyroid hormone (PTH) and PTH-related protein (PTHrP). The intracellular tail domain of the PTHr1 contributes to G protein subunit coupling that is important for second messenger signaling. PTHr1 signals through several second messenger pathways, including adenylyl cyclase and phospholipase C.

PTH-induced activation of the PTHR results in the internalization of the PTH-receptor complex via the clathrin-coated pit pathway and is the consequence of the formation of a complex between β -arrestin2, the clathrin adaptor protein AP2, clathrin, and the activated receptor. Internalization has at least two outcomes: directing the receptor to a compartment where the phosphates are removed, allowing resensitization via recycling, and movement of the receptor to lysosomes for degradation (4).

Intact PTH 1–84 is a key endocrine regulator of calcium homeostasis and is secreted by parathyroid cells in response to reduced ionised calcium in the blood and, with its cleavage products (providing the N-terminus is preserved), activates the PTH/PTHrP receptor found in key target organs. The receptor is expressed, among other cells, by osteoblasts, osteocytes and bone-lining cells, and activates distinct G protein signaling cascades by coupling with either adenylate cyclase, phospholipase C or cAMP/protein kinase A depending upon the cell type (5-8). The receptor is also responsive to parathyroid hormone-related peptide (PTHrP). C-terminal fragments (formed by intracellular cleavage both within the parathyroid and in target organs of PTH) form the major circulating fraction because of their low catabolism. Although, the biological actions of C-terminal fragments are unclear, they appear to have a distinct receptor (9), to enhance osteoblast activity in culture (10) and to be highly expressed in osteocyte-like cells (11).

The parathyroid cell is sensitive to changes in extracellular calcium concentrations, with small increases in extracellular calcium inhibiting secretion of PTH. Conversely, a decrease in extracellular calcium steers to a rapid increase in PTH secretion. Characterization of the surface calcium-sensing receptor of the parathyroid cell showed a large extracellular domain for binding cations (12), with activation of the receptor via G protein coupling (13). Activation leads to rapid mobilization of

intracellular calcium via inositol triphosphate, with acutely elevated cytoplasmic calcium responsible for inhibiting PTH exocytosis (14). Receptor binding and potentiation by calcimimetic drugs increase the receptor sensitivity to calcium and results in decreased PTH secretion, with results from clinical trials suggesting efficacy of such drugs in treating primary and secondary hyperparathyroidism (15,16). Conversely, calcilytic compounds developed to antagonise the calcium receptor are a potential new pharmaceutical means of creating an endogenous surge of PTH for anabolic bone effects, as seen in a recent animal study (17). Mutations of the calcium-sensing receptor (both gain-of-function (18), and loss-of-function (19)) can result in either autosomal dominant hypocalcaemia (18) or familial hypocalciuric hypercalcaemia (19).

It is now possible to synthesize either the whole PTH molecule or specific fragments by recombinant technology. Initial studies with PTH, however, used PTH 1–34 (teriparatide) as it was thought to be similar to the natural cleavage product and retained the bioactivity of PTH 1–84 in bioassay. More recent studies with PTH 1–38 (20), PTH 1–84 (21) and PTHrP 1–36 (22) have suggested potential new applications with fragments of different structure, what is particularly intriguing given the distinct actions of the C-terminal fragment present in PTH 1–84 (21). The majority of clinical studies with PTH as a treatment for osteoporosis have involved parenteral administration; however, in one study, PTH 1–34 was delivered by direct plasmid gene incorporation of PTH 1–34 and expression by fibroblasts for the *in vivo* treatment of bone defects (23).

4.2. Results & Discussion

To study the parathyroid hormone receptor (PTHr1) behavior at the plasma membrane of living cells, its mobility pattern and an internalization rate, we applied single-molecule tracking that is an appropriate technique for the spatial-temporal investigation such as signal transduction and the molecular complexes formation.

Cos-1 and AD293 cells were transiently transfected with the ACP-PTHr construct, the acetyl carrier transferase protein fusion to the N-terminus of the human parathyroid hormone receptor. That allowed for a covalent labeling of the receptor with quantum dot-CoA and entirely maintaining the receptor activity (see Captions 1.1-1.4).

We tested PTHr1 under stimulation with five peptide ligands, specific fragments of PTH: hPTH(1–34), hPTHrP(107–111)NH₂; PTH(1–14); PTH(1–28) G¹R¹⁹, bPTH(3–34), from which the first four are known to belong to PTH agonist group and the last is an antagonist. Ligands were applied in the concentration range from 250pM to 250μM, with ten-fold increment for particular experiments. Data were gathered on the fluorescent microscope up to 30 min after receptor ligand stimulation.

According to the foremost observation, within 30min after ligand application receptor internalization occurred (Figure 1). We could follow the receptor not only at the cellular membrane but also inside the cell.

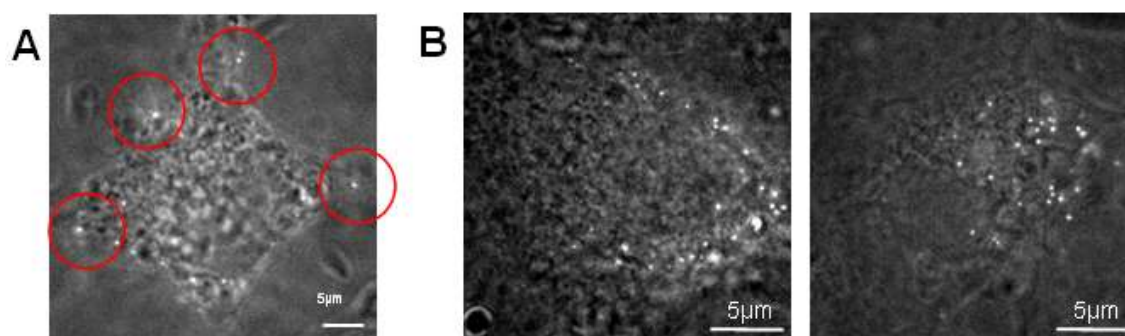


Figure 1. QD-ACP-PTHr1 receptor internalization. Fluorescence images of labeled at the cell membrane receptors (**A**); receptors are at the membrane (left panel) and 20 min after 2.5 nM PTH/1-28/ the internalization process is registered (right panel) (**B**)

The rate of internalization depended on a ligand-type and applied concentration. The mean value of internalizing molecules was calculated on the base of five independent experiments and obtained for all ligand types and concentrations. Here, an

example of the internalization profile is presented for 2.5 nM ligand concentration (Figure 2).

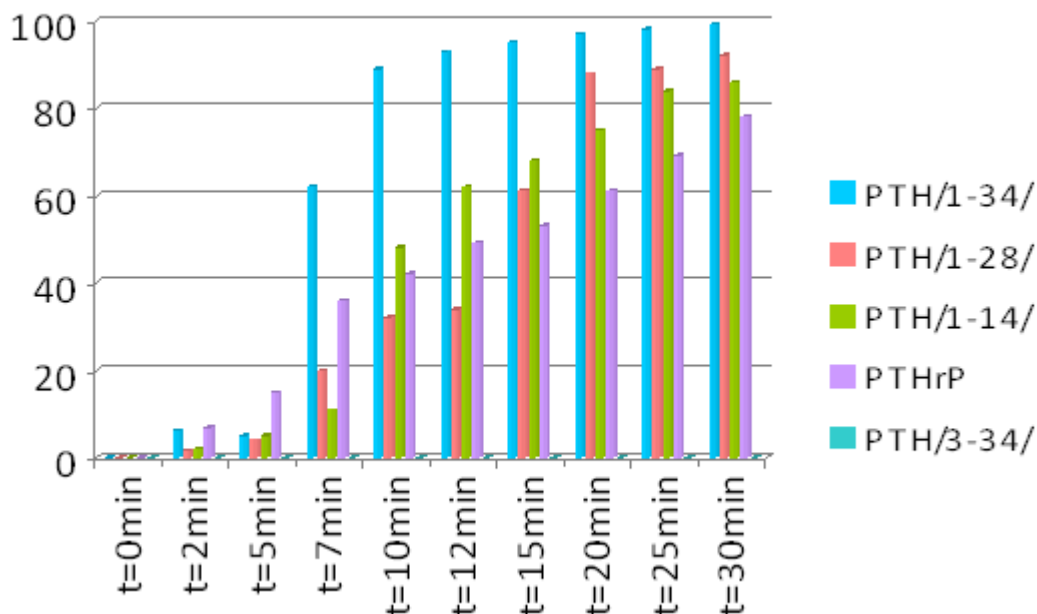


Figure 2. QD-ACP-PTHR1 receptor internalization profile for 2.5 nM ligand concentration. Data shown are from five independent experiments.

No significant changes, no internalization events, were observed after application of bPTH(3–34), the PTHR receptor antagonist. Attached QDs ‘shaked’ only, showing almost no movement.

After stimulation with hPTH(1–34) PTHR receptor mobility was restricted to the region of a small confinement and reminded trembling, however in this case internalization was observed, for example after 15min for 250pM hPTH(1–34), already in 2 min for 2.5nM and in 5 min for 25nM.

Application of 250nM hPTHrP(107–111)NH₂ resulted in a full internalization of QD-receptor complexes by the time of 7 min, whereas stimulation with the same concentration of PTH(1–28) G^{1R}¹⁹ and PTH(1–14) produced the same effect already after 2 and 5 min, respectively.

Higher concentration of PTH analogues showed also tendency to increased trajectories (Figure 3). Interestingly, higher ligand concentration also caused a sudden and short but complete immobilization of the receptors.

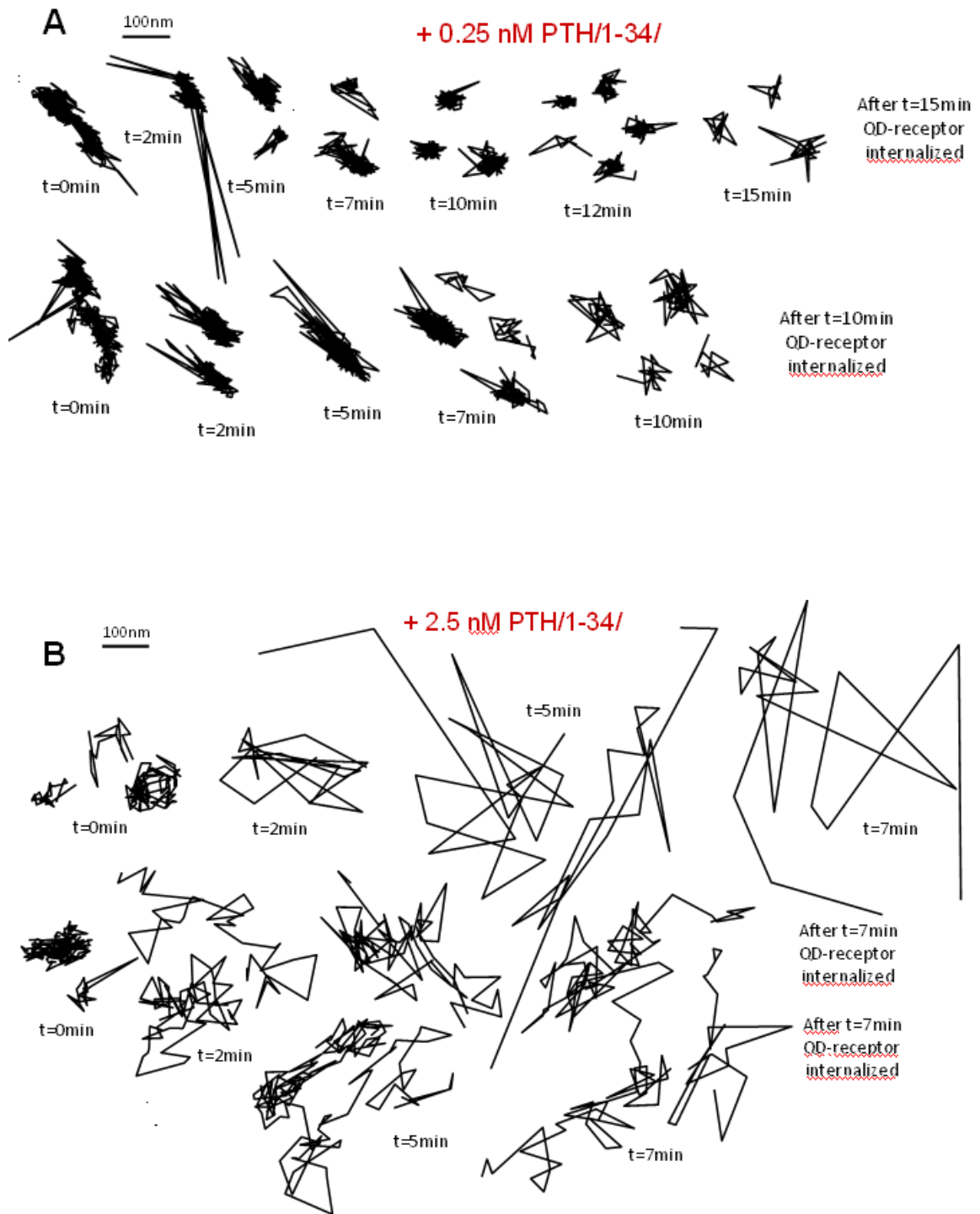


Figure 3AB. Trajectories of particular QD-ACP-PTH receptors after ligand stimulation.
Example of 0.25 nM (A) and 2.5 nM (B) concentration of PTH/1-34/ ligand application

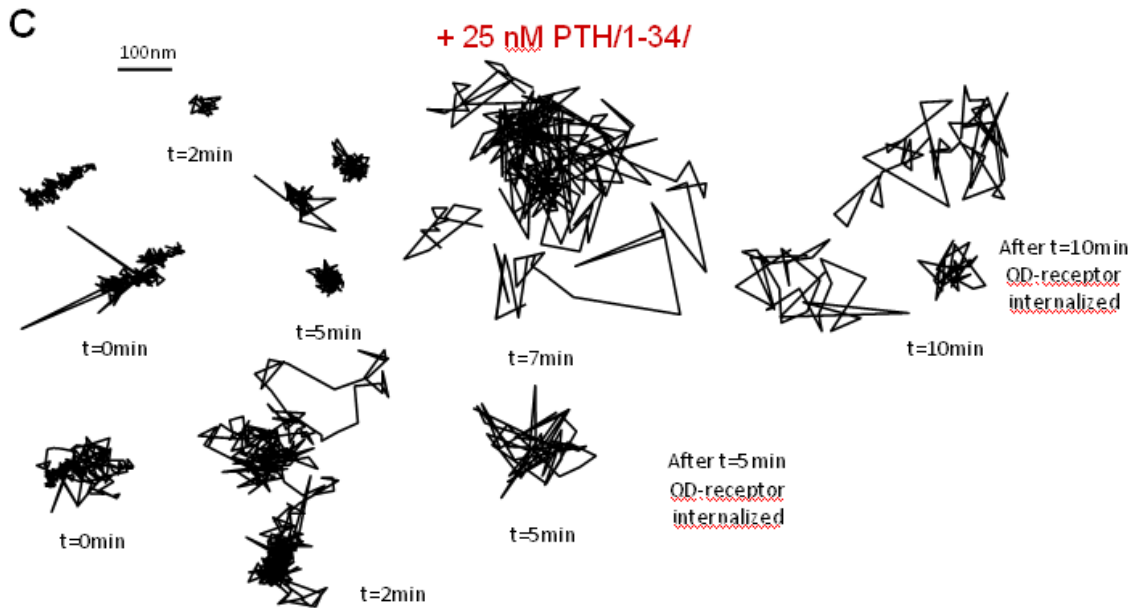


Figure 3C. Trajectories of particular QD-ACP-PTH receptors after ligand stimulation. Example of 25 nM (C) concentration of PTH/1-34/ ligand application

During microscopic measurement also recycling process appeared. The fastest time after which receptor recycling occurred, was registered 10min after ligand addition (Figure 4).

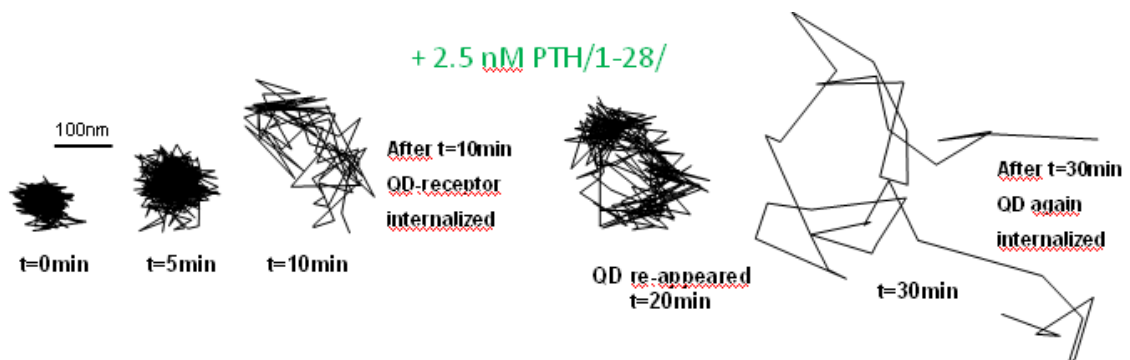


Figure 4. Example of the particular QD-ACP-PTH that recycled. After application of 2.5 nM PTH/1-28/ G^{1R} ¹⁹ observed QD-receptor internalized in 10 min and returned at the membrane in t=20 min. Ten minutes receptor was internalized. The next internalization was noticed at time t=30 min.

Regarding mobility analysis we could not state extreme differences in MSD versus time plots for PTHR when compared ligands between in each other in appropriate concentrations. Figure 5 displays the example of MSD plot for PTHR after PTH(1-14).

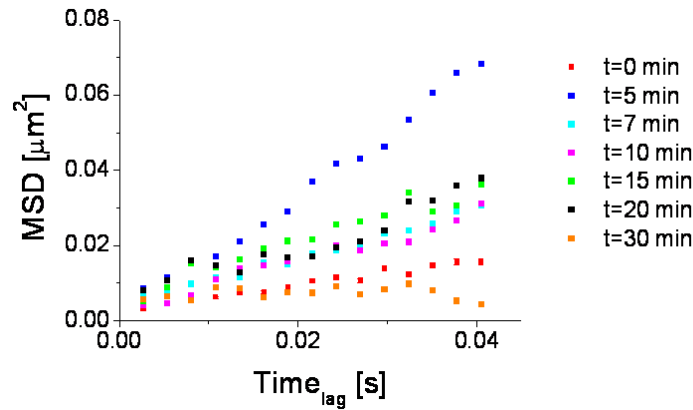


Figure 5. Example of QD-ACP-PTHR mobility characteristic when 2.5 nM PTH/1-14/ was applied. The graph presents the averaged MSD versus Time plots for all receptors from 5 independent experiments.

In all experiments it has been confirmed that not only the 34 amino acid peptide fragment of PTH activates the parathyroid hormone receptor at the cell membrane efficiently, initializing receptor internalization, but also other tested PTH fragments resulted in receptor activation. However, there was a slight tendency observed that the lowering activity occurred from hPTH(1–34), PTH(1–28)G^{1R19} to PTH(1–14), what was measured with the internalization rate and the mobility of receptors.

hPTHrP(107–111)NH₂ showed the lowest efficiency. PTH(3–34) confirmed to be an antagonist for parathyroid hormone receptor as there was no internalization observed after its addition. Interestingly, in some cases PTH(1–28)G^{1R19} caused higher internalization rate and higher mobility of the receptors than teriparatide.

Taken together, applied single-molecule tracking enabled to scrutinize the parathyroid hormone receptor (PTHR1) behavior at the plasma membrane of living cells, to recognize its mobility pattern, define the internalization and recycling rates under no ligand stimulation as well as upon stimulation of respective peptide ligands.

4.3. Materials and methods

4.3.1. Plasmid Construction of ACP-PTHr

The acetyl carrier transferase protein fusion to the N-terminus of the human parathyroid hormone receptor was produced in a similar manner as previously reported for the N-terminally labeled GFP-PTHr (ref. Johnsson – ACP fusion labeling and Castro – GFP-N-PTHr) following a PCR strategy using *pfu* DNA polymerase (Fermentas). cDNA encoding the N-terminal fragment of human PTHr (corresponding to amino acids 1-60) was amplified with primers containing restriction sites for HindIII (5') and BamHI (3'). ACP cDNA (ref. Johnsson – ACP) was amplified without stop and start codons with primers containing restriction sites for BamHI (5') and EcoRI (3'). cDNA encoding the fragment of human PTHr (corresponding to amino acids 102-593) (ref Castro) was amplified with primers containing restriction sites for EcoRI (5') and EcoRV (3') and also stop codon. All three PCR products were subcloned together by ligation after digestion with the same restriction enzyme in to pcDNA3 (Invitrogen) for transfection and expression in mammalian cells. The final construct did not include the pharmacologically un-important residues 61-101 but did include a six residue linker between the ACP C-terminus and PTHr N-terminus (Arg-Leu-Ile-Ser-Gly-Ser). The subcloned in to pcDNA3 construct was verified by sequencing.

4.3.2. Cell Culture

African green monkey kidney cells (COS-1) and Human embryonal kidney cells (AD293) were cultured in DMEM - Duplecco's Modified Eagle's Medium (Sigma) supplemented with 10% fetal calf serum (PAA Laboratories GmbH) and 1% penicillin/streptomycin (Sigma) solution at 37°C/5% CO₂. FuGENE 6 (Roche Applied Science) and Effectene Transfection Reagent (Invitrogen) were facilitated for COS-1 and AD293 cells transient transfections, respectively. For single-molecule-imaging cells were seeded into six-well plates containing glass cover slips (24mm, thickness class 1, Hartenstein GmbH).

4.3.3. Labeling

Labeling was performed by incubating the cells on the cover slips for 30 min at 37°C in DMEM (270µl) with 1% Bovine Serum Albumin (BSA, Sigma); 1.5µM 6xHis-PPTase

and 0.3nM CdSe/ZnS Quantum Dot – CoA molecules prepared with the 655 Qdot Antibody Conjugation Kit (Molecular Probes, Invitrogen). Before measurements samples were washed three times with 500 μ l DMEM. Experiments were conducted on cells in 300 μ l DMEM.

4.3.4. Peptide Ligands

The peptide ligands used were as follows: hPTH(1–34), hPTHrP(107–111)NH₂; PTH(1–14); PTH(1–28) bPTH(3–34). The human PTH(1–34) (free carboxy terminus), human PTHrP(107-111), and bovine PTH(3-34) was purchased from Bachem California (Torrance, CA). The PTH(1–14) and PTH(1–28) peptides were synthesized by the Massachusetts General Hospital Biopolymer Core facility, as described (ref. MGH). Peptide quality was verified by analytical HPLC, matrix-assisted laser desorption/ionization mass spectrometry and amino acid analysis, and peptide concentrations of stock solutions were established by amino acid analysis. Radiolabeled peptide variants were prepared by the oxidative chloramine-T procedure using Na¹²⁵I (specific activity, 2200 Ci/mmol; PerkinElmer/NEN Life Science Products, Boston, MA) and were purified by reversed-phase HPLC.

Ligands were added in concentrations from 250pM to 250 μ M, with ten-fold increment for particular experiments.

4.3.5. Pharmacology

Ligand binding and measurement of cAMP were performed as described (ref. Pharmacology Harvard) with minimal modifications. For binding studies, stably transfected cells grown in 24-well plates were incubated in DHB buffer (serum-free DMEM containing 20 mM Hepes and 1% BSA) for 1 h at 0°C, followed by a 1.5-h incubation with the same buffer containing ¹²⁵I-PTH(1-34) (100,000 cpm per well) as a radioligand with or without varying concentrations of unlabeled peptides. Cells were washed three times with iced PBS and extracted with 0.8 M NaOH, and cell-associated ¹²⁵I-PTH(1-34) was counted.

For cAMP assays, cells grown in 12-well plates were washed twice with Hepes buffer (137 mM NaCl/5 mM KCl/1 mM CaCl₂/1 mM MgCl₂/20 mM Hepes, pH 7.4) and incubated with isobutylmethylxanthine (0.5 mM) in the same buffer for 5 min at 37°C. Cells were stimulated with varying concentrations of PTH(1-34) or PTH(1-34)^{TMR} at 37°C for 15 additional min. Cellular cAMP was extracted and measured by RIA (Immunotech,

Luminy, France; Beckman Coulter). Competition binding studies and concentration-response data were analyzed with the program PRISM 4.0 (GraphPad, San Diego).

4.3.6. Single-molecule microscopy

according to the point 1.3.5.

4.3.7. Total internal reflection single-molecule microscopy

according to the point 1.3.6.

4.3.8. Data analysis

according to the point 1.3.7.

4.3.9. Mobility analysis

according to the point 1.3.8.

4.4. References

1. Gardella, T. J., and Jüppner, H. Interaction of PTH and PTHrP with their receptors. (2000) *Rev. Endocrinol. Metab.* 1, 317–329
2. Ferrari, S. L., Behar, V., Chorev, M., Rosenblatt, M., and Bisello, A. Endocytosis of ligand-human parathyroid hormone receptor 1 complexes is protein kinase C-dependent and involves beta-arrestin2. Real-time monitoring by fluorescence microscopy. (1999) *J. Biol. Chem.* 274, 29968–29975
3. Ferrari, S. L., and Bisello, A. Cellular distribution of constitutively active mutant parathyroid hormone (PTH)/PTH-related protein receptors and regulation of cyclic adenosine 3',5'-monophosphate signaling by beta-arrestin2. (2001) *Mol. Endocrinol.* 15, 149–163
4. Vilardaga JP, Krasel C, Chauvin S, Bambino T, Lohse MJ, Nissenson RA., Internalization determinants of the parathyroid hormone receptor differentially regulate beta-arrestin /receptor association. *J Biol Chem.* 2002 Mar 8;277(10):8121-9.
5. Schwindinger WF, Fredericks J, Watkins L, Robinson H, Bathon JM, Pines M, Suva LJ, Levine MA: Coupling of the PTH/PTHrP receptor to multiple G-proteins. Direct demonstration of receptor activation of Gs, Gq/11, and Gi(1) by [alpha-32P]GTP-gamma-azidoanilide photoaffinity labeling. *Endocrine* 1998, 8:201-209.
6. Cheung R, Erclik MS, Mitchell J: Increased expression of G(11)alpha in osteoblastic cells enhances parathyroid hormone activation of phospholipase C and AP-1 regulation of matrix metalloproteinase-13 mRNA. *J Cell Physiol* 2005, 204:336-343.
7. Kondo H, Guo J, Bringhurst FR: Cyclic adenosine monophosphate/protein kinase A mediates parathyroid hormone/parathyroid hormone-related protein receptor regulation of osteoclastogenesis and expression of RANKL and osteoprotegerin mRNAs by marrow stromal cells. *J Bone Miner Res* 2002, 17:1667-1679.
8. Bringhurst FR: PTH receptors and apoptosis in osteocytes. *J Musculoskelet Neuronal Interact* 2002, 2:245-251.
9. Nguyen-Yamamoto L, Rousseau L, Brossard JH, Lepage R, D'Amour P: Synthetic carboxyl-terminal fragments of parathyroid hormone (PTH) decrease ionized calcium concentration in rats by acting on a receptor different from the PTH/PTH-related peptide receptor. *Endocrinology* 2001, 142:1386-1392.
10. Sutherland MK, Rao LG, Wylie JN, Gupta A, Ly H, Sodek J, Murray TM: Carboxyl-terminal parathyroid hormone peptide (53-84) elevates alkaline phosphatase and osteocalcin mRNA levels in SaOS-2 cells. *J Bone Miner Res* 1994, 9:453-458.

11. Divieti P, Inomata N, Chapin K, Singh R, Juppner H, Bringhurst FR: Receptors for the carboxyl-terminal region of pth(1-84) are highly expressed in osteocytic cells. *Endocrinology* 2001, 142:916-925.
12. Brown EM, Gamba G, Riccardi D, Lombardi M, Butters R, Kifor O, Sun A, Hediger MA, Lytton J, Hebert SC: Cloning and characterization of an extracellular Ca(2+)-sensing receptor from bovine parathyroid. *Nature* 1993, 366:575-580.
13. Brown EM, MacLeod RJ: Extracellular calcium sensing and extracellular calcium signaling. *Physiol Rev* 2001, 81:239-297.
14. Nemeth EF, Scarpa A: Rapid mobilization of cellular Ca²⁺ in bovine parathyroid cells evoked by extracellular divalent cations. Evidence for a cell surface calcium receptor. *J Biol Chem* 1987, 262:5188-5196.
15. Peacock M, Bilezikian JP, Klassen PS, Guo MD, Turner SA, Shoback D: Cinacalcet hydrochloride maintains long-term normocalcemia in patients with primary hyperparathyroidism. *J Clin Endocrinol Metab* 2005, 90:135-141. Multicenter, randomized, double-blind, placebo-controlled study into the use of cinacalcet (a calcimimetic) to reduce serum calcium in primary hyperparathyroidism.
16. Charytan C, Coburn JW, Chonchol M, Herman J, Lien YH, Liu W, Klassen PS, McCary LC, Pichette V: Cinacalcet hydrochloride is an effective treatment for secondary hyperparathyroidism in patients with CKD not receiving dialysis. *Am J Kidney Dis* 2005, 46:58-67.
17. Gowen M, Stroup GB, Dodds RA, James IE, Votta BJ, Smith BR, Bhatnagar PK, Lago AM, Callahan JF, DelMar EG et al.: Antagonizing the parathyroid calcium receptor stimulates parathyroid hormone secretion and bone formation in osteopenic rats. *J Clin Invest* 2000, 105:1595-1604.
18. Pollak MR, Brown EM, Chou YH, Hebert SC, Marx SJ, Steinmann B, Levi T, Seidman CE, Seidman JG: Mutations in the human Ca(2+)-sensing receptor gene cause familial hypocalciuric hypercalcemia and neonatal severe hyperparathyroidism. *Cell* 1993, 75:1297-1303.
19. Pollak MR, Chou YH, Marx SJ, Steinmann B, Cole DE, Brandi ML, Papapoulos SE, Menko FH, Hendy GN, Brown EM et al.: Familial hypocalciuric hypercalcemia and neonatal severe hyperparathyroidism. Effects of mutant gene dosage on phenotype. *J Clin Invest* 1994, 93:1108-1112.
20. Hodsmann AB, Steer BM, Fraher LJ, Drost DJ: Bone densitometric and histomorphometric responses to sequential human parathyroid hormone (1-38) and salmon calcitonin in osteoporotic patients. *Bone Miner* 1991, 14:67-83.
21. Hodsmann AB, Hanley DA, Ettinger MP, Bolognese MA, Fox J, Metcalfe AJ, Lindsay R: Efficacy and safety of human parathyroid hormone-(1-84) in increasing bone mineral density in postmenopausal osteoporosis. *J Clin Endocrinol Metab* 2003, 88:5212-5220.
22. Stewart AF: PTHrP(1-36) as a skeletal anabolic agent for the treatment of osteoporosis. *Bone* 1996, 19:303-306.

23. Bonadio J, Smiley E, Patil P, Goldstein S: Localized, direct plasmid gene delivery in vivo: prolonged therapy results in reproducible tissue regeneration. *Nat Med* 1999, 5:753-759.

Curriculum Vitae

Monika Zelman-Femiak

Date and Place of Birth:
14 April 1980 Warsaw / Poland

Address:
**Straubmühlweg SWH 2
Haus A10 / 703
97078 Würzburg
Germany**

Corresponding Address:
**AG Harms Molecular Microscopy
Rudolf Virchow Center
DFG-Research Center for Experimental Biomedicine
Josef-Schneider Str. 2 / D15
97080 Würzburg
Germany**

Mobile & Office Phones:
**+49 176 78 28 33 46
+49 931 31 80 360**

E-mail:
**zelmona@virchow.uni-wuerzburg.de
zelmona@gmail.com**

Education

10.2007-present: PhD studies, Molecular Microscopy Group, Rudolf Virchow Center, DFG-Research Center for Experimental Biomedicine, Würzburg, Germany
2006-2007: Property Valuation Postgraduate Studies, Faculty of Law and Administration, Warsaw University, Warsaw, Poland
2004: Master of Science Degree in Chemistry
Laboratory of Peptides, Chemistry Department, Warsaw University, Warsaw, Poland
Thesis title: Synthesis of homoarginine-containing opioid peptide
2000-2003: Faculty of Economic Sciences, Warsaw University, Warsaw, Poland
1999-2004: Chemistry Department, Warsaw University, Warsaw, Poland
1995-1999: Reytan High School, Warsaw, Poland

Research Experience

10.2007-present: PhD student, Molecular Microscopy Group, Rudolf Virchow Center, DFG-Research Center for Experimental Biomedicine, Würzburg, Germany
2004-2007: Young Researcher, Department of Lipid Biochemistry, Institute of Biochemistry and Biophysics, Polish Academy of Sciences, Warsaw, Poland
06-08.2003: Trainee, Polfa Warsaw SA Pharmaceutical Company, Warsaw, Poland
2002-2004: Volunteer Researcher, Department of Lipid Biochemistry, Institute of Biochemistry and Biophysics, Polish Academy of Sciences, Warsaw, Poland
2001-2002: Volunteer Researcher, Department of Biophysics, Institute of Biochemistry and Biophysics, Polish Academy of Sciences, Warsaw, Poland

Publications

Lateral mobility of BMP type I receptor selectively modulates non-SMAD signalling

Zelman-Femiak M*, Guzman A*, Knaus P, Harms GS

(* authors contributed equally to the work)

Submission to Nat Cell Biol.

Quantum dots for single-molecule biological imaging on native cell membranes

Zelman-Femiak M, Noskov A, Lambright G, Bhushan S, Lohse MJ, Harms GS

Submission to Nat Meth.

Covalent quantum dot receptor linkage via the acyl carrier protein for single-molecule tracking, internalization, and trafficking studies.

Zelman-Femiak M, Wang K, Gromova KV, Knaus P, Harms GS

Biotechniques. 2010 Aug;49(2):574-9.

Detection of single quantum dots in model organisms with sheet illumination microscopy.

Friedrich M, Nozadze R, Gan Q, Zelman-Femiak M, Ermolayev V, Wagner TU, Harms GS.

Biochem Biophys Res Commun. 2009 Dec 18;390(3):722-7.

Contribution of the mevalonate and methylerythritol phosphate pathways to the biosynthesis of dolichols in plants.

Skorupinska-Tudek K, Poznanski J, Wojcik J, Bienkowski T, Szostkiewicz I, Zelman-Femiak M, Bajda A, Chojnacki T, Olszowska O, Grünler J, Meyer O, Rohmer M, Danikiewicz W, Swiezewska E

J Biol Chem. 2008 Jul 25;283(30):21024-35.

In vitro plant tissue cultures accumulate polyisoprenoid alcohols.

Skorupinska-Tudek K, Pytelewska A, Zelman-Femiak M, Mikoszewski J, Olszowska O, Gajdzis-Kuls D, Urbanska N, Syklovska-Baranek K, Hertel J, Chojnacki T, Swiezewska E

Acta Biochim Pol. 2007;54(4):847-52.

Synthesis and biological activity of homoarginine-containing opioid peptides

Izdebski J, Kunc D, Schiller PW, Chung NN, Gers T, Zelman M, Grabek M

J Pept Sci. 2007 Jan;13(1):27-30.

Farnesyl phosphates are endogenous ligands of lysophosphatidic acid receptors: inhibition of LPA GPCR and activation of PPARs.

Liliom K, Tsukahara T, Tsukahara R, Zelman-Femiak M, Swiezewska E, Tigyi G

Biochim Biophys Acta. 2006 Dec;1761(12):1506-14.

Dolichols of the fern *Matteucia struthiopteris*

Wojtas M, Bienkowski T, Zelman-Femiak M, Tateyama S, Sagami H, Chojnacki T, Danikiewicz W, Swiezewska E

Acta Biochim Pol. 2005;52(1):255-9

Erratum

Single Particle Tracking Membrane Receptor Dynamics

submitted by

Monika Zelman-Femiak

Chapter 2 32

BMP type I and II receptors mobility linked to non-SMAD/SMAD signaling

2.2. Results & Discussion 35

List of figures that were provided by Asja Guzman / Prof. Petra Knaus
Institut für Chemie und Biochemie - Biochemie
Freie Universität Berlin
Thielallee 63
14195 Berlin

Figure 2g-h. Lateral mobility of BMPRII is reduced upon ligand stimulation. (page 38)

(g,h) Enhanced DRM-association of endogenous BMPRII upon ligand stimulation as assessed by co-fractionation with the DRM-marker Caveolin1. C2C12 cells were starved and stimulated with BMP-2 for 5 min. After cell surface biotinylation cells were used for sucrose gradient fractionation and subsequent streptavidin precipitation of biotinylated proteins. Precipitates were subjected to Western blot analysis. Quantification of Western blot analysis demonstrates the increased proportion of BMPRII in DRM-fractions after BMP-2 addition.

Figure 4a-c. Structural components mediating the confined mobility of BMPRIb. (page 42)

(a) Mutagenesis approach for identification of structural elements responsible for the immobility of BMPRIb. Point mutations, a poly-alanine scan of the transmembrane domain and intracellular truncations of BMPRIb were generated by targeted mutagenesis. The wild type sequence of transmembrane domain is depicted in black, the mutated amino acids in red.

(b,c) Reduced DRM-association of BMPRIb transmembrane domain (TM) mutants as assessed by co-fractionation of receptor with Caveolin1. C2C12-TM2, -TM5 and -PKT cells were used for sucrose gradient fractionation and fractions were subjected to Western blot analysis (b). The histogram (c) depicts the percentage of receptor present in DRM-fractions obtained by quantification of the Western blot analysis.

Figure 5. Effects of enhanced BMPRIb mobility on signaling. (page 44)

(a,b) Western blot analysis of Smad1/5/8, p38 and Akt activation in C2C12-BMPRIb *wt*, -TM2, -TM5 and -PKT cells. Cells were stimulated with BMP-2, GDF-5 or pure PBS for 60 min. Cell lysates were subjected to Western blot analysis of respective phosphorylated proteins. GAPDH was used as loading control. Quantification of Western blot (b) depicts relative intensity of phospho-specific signals normalized to respective GAPDH.

(c) Expression analysis of osteoblastic differentiation markers in C2C12-BMPRIb *wt* or mutant cells. C2C12-BMPRIb *wt*, -TM2, -TM5 and -PKT cells were starved, stimulated with GDF-5 for 12 h or 48 h and used for RNA isolation. Quantitative RT-PCR was performed to analyze gene expression of *Runx2*, *ALP*, *Osterix* and *OCN*. Gene expression was normalized to *HPRT* expression and plotted as mean normalized values (MNE).

(d) Analysis of Smad-mediated transcriptional activation by BMP-responsive reporter gene assay. Cells were transfected with BMP-responsive and constitutive active luciferase constructs, starved and stimulated with GDF-5 for 6 h. Luciferase activity was measured in cell lysates. Quantification shows GDF-5-induced luciferase activity normalized to constitutive luciferase activity.

(e) Alkaline phosphatase (ALP) activity assay. C2C12 cells-BMPRIb *wt*, -TM2, -TM5 and -PKT cells were starved and stimulated with various concentrations of GDF-5 for 72 h. ALP production indicative for osteoblastic differentiation was assessed by a colorimetric assay of enzymatic activity of ALP.

Figure 6a. Increased lateral mobility of receptor does not impair receptor endocytosis. (page 46)

(a) FACS-based analysis of BMPRIb internalization. HA-tagged BMPRIb *wt* or mutant receptors transiently expressed in HEK293T were fluorescently labeled and the decrease of surface fluorescence assessed by FACS-measurements. The line plot depicts the time-dependent decrease of mean fluorescence indicative of receptor internalization.